Synthesis of One-Dimensional TiO_2 Nanotube Arrays by Potentiostatic Anodisation

By

Anele Tshaka

A thesis submitted at the University of the Western Cape (UWC) in fulfilment of the requirements for a degree of Magister in Science

Supervisor : Dr F. R. Cummings, UWC

Co-Supervisors : Dr F. G. Muller, UWC

Dr D. E. Motaung, CSIR

December 2017

DEDICATION

This thesis is nicely dedicated to my mother,

Zameka Orippa Tshaka

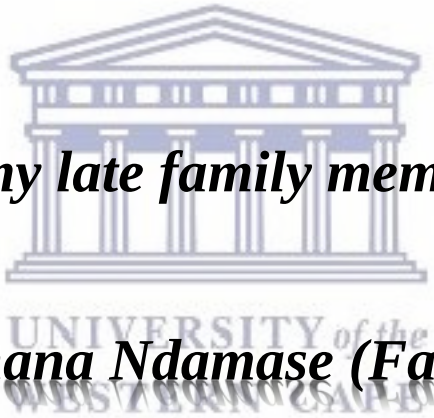

And my late family members,

Sidunana Ndamase (Father)

Nomava Vivian Tshaka (Sister)

Monde Tshaka (Brother)

ACKNOWLEDGEMENTS

I would like to send a special thank you to the following people and organisations for their continuous support and encouragement during the journey. If it wasn't for their influence, the completion of this thesis wouldn't be possible

Dr Francious Riccardo Cummings of the Electron Microscope Unit (EMU) at the Department of Astronomy and Physics (UWC), for the excellent supervision of this thesis, encouragement and many other stimulating discussions.

Dr Theophillus Frederic George Muller of the Department of Astronomy and Physics (UWC) and Dr David Motaung of the Council for Scientific and Industrial Research (CSIR) who acted as the co-supervisors of this thesis, for their wise-words of advice and support.

Dr Gerald Malgas of the Department of Astronomy and Physics (UWC), for his constant encourage and interest in my progress.

Prof Christopher Arendse (H.O.D) of the Department of Astronomy and Physics (UWC) for his support and encouragement at times when I needed them the most.

Mrs. Angela Adams the secretary of the Department of Astronomy and Physics (UWC), for the continuous support and encouragement. Most importantly for the comforting words during the time when I lost my father.

The staff of the Department of Astronomy and Physics and the whole MANUS/MATSCI group, for their direct and indirect support, to mention a few; D. J. Ongori, Prof N. Ocre, Dr L. Square, Mr. M. Paradza, Mrs. N. Kenseley, S. Tanci, S. Ngqoloda, N. V. Petersen, E. McDonald, S. Magubane, S. Khanyile, S. Matshawule and M. B. Laden.

The National Research Foundation (NRF), iThemba Labs and University of the Western Cape for the financial support during this study. Council for Scientific and Industrial Research (CSIR) and Electron Microscope Core of the University of Missouri for allowing me to use their instruments.

To my immediate, extended family and friends for their encouragement and support:

Firstly, my mother Zameka Orippa Tshaka for the love, support and always inspiring me to greater achievements – I love you

To the rest of my family, Siviwe, Siyabonga, Snoxolo, Vatiswa, Yonela, Thelezi, Philani, Lubabalo and the rest of the Ndamase family, thank you guys for being there for me at needy times.

To my daughter and close friends, Yakha Awonke (daughter – my pillar of strength), Abulele Mkiva, Andile Peter, Lukhona Gobingca, Xolani Tsutswana, Zonwabele Sapula and Luzuko Makhaphela - thank you guys for your support and for being always good to me.

The Almighty God, my Creator

Thank you

DECLARATION

I declare that

"Synthesis of One-Dimensional TiO_2 Nanotube Arrays by Potentiostatic Anodisation"

Is my own work, that is has not been submitted for a degree or examination in any other institution, and that all the sources I have used or quoted have been indicated and acknowledged by means of complete references.

Anele Tshaka **December 2017**

Signature…….

KEY WORDS

Synthesis of One-Dimensional TiO_2 Nanotube Arrays by Potentiostatic Anodisation

Anele Tshaka

TiO_2 Nanotubes

Anodisation

Nanomaterial

Nanoscale

Compact-Oxide Layer

Field-aided Oxidation

Field-aided Dissolution

Photocatalysis

Electron Microscope

Scanning Electron Microscope

Morphology

Transmission Electron Microscope

X-Ray Diffractometer

Electron Energy Loss Spectroscopy

Scanning Transmission Electron Microscopy

Crystallinity

ABSTRACT

Synthesis of One-Dimensional TiO_2 Nanotube Arrays by Potentiostatic Anodisation

Anele Tshaka

MSc Thesis, Department of Astronomy and Physics, University of the Western Cape

TiO_2 nanomaterials, in particular nanotubes, are some of the most studied materials, as they are considerably important in technological and biological applications due to their unique electronic properties and biocompatibility. For example, vertically aligned TiO_2 nanotubes play a crucial role in photovoltaics as they enhance the charge separation as a result of their excellent photo-catalytic properties in the presence of organic dye molecules, and provide a superior one-dimensional transport route compared to nanoparticle films. There are numerous techniques used to synthesise TiO_2 nanotubes, such as chemical vapor deposition (CVD), template based techniques, anodisation, to name but a few. However, due to its non-toxicity environmental friendliness and cost-effectiveness, anodisation is the most common technique to synthesise TiO_2 nanotubes. In addition anodisation allows for control over the morphology when tailoring the anodisation parameters such as voltage, concentration, temperature and duration. It is well-documented that the as-synthesised TiO_2 nanotubes via anodisation technique are amorphous and require post-treatment at elevated temperature (above 280°C) to induce crystallinity into anatase phase. Further increase in annealing temperature results in crystallisation in either rutile or mixed phase structure.

However, a clear description of the crystalline evolution throughout the nanotube remains lacking. In addition, a clear understanding of how this peculiar crystallinity affects the localised opto-electronic properties which ultimately affect their performance in electronic devices such as in photovoltaics, is also not well studied in literature. As such, this study aims at investigating the effect of various electrolyte compositions on the resulting morphology, together with the effect of annealing temperature on the structure of TiO_2 nanotubes by means

of in-depth electron microscopy analyses. The bulk of this study is aimed at investigating the crystallographic transformation along the nanotube length by means scanning transmission electron microscopy coupled with electron energy loss spectroscopy (STEM-EELS) and Jump-Ratio imaging, while valence EELS (VEELS) is employed to quantify the localised optical properties of the nanotubes. X-ray diffraction studies are employed as a complementary technique to transmission electron microscopy (TEM) to probe for changes in the bulk crystallinity post thermal treatment of the as-synthesised TiO_2 nanotubes.

Three different electrolyte regimes of different pH and viscosity were used to synthesise TiO_2 nanotubes. It was found that, anodisation of the Ti foil in neutral, organic electrolytes (i.e. regime 3, consisting of 0.14 M (1 vol%) NH_4F + 97 vol% PEG + 2 vol% H_2O) at longer anodisation durations yields nanotubes with high aspect ratios compared to those obtained when using an acidic (regime 1, 0.14 M (0.5 vol%) NaF + 0.5 M (2.5 vol%) H_3PO_4 + 97 vol% H_2O) and neutral (regime 2, 1 M (3 vol% NaF + 2 vol% H_2O + 95 vol% glycerol). Furthermore, it was found that upon annealing nanotubes at a temperature of 450 °C in air for 3 hours, the nanotube walls crystallises in predominantly anatase phase while the underlying barrier layer is rutile rich. When the annealing temperature was increased to 600 °C, coexistence of both anatase and rutile phase along the nanotube length was observed with nanotube top and bottom showing crystallisation in predominantly anatase and rutile respectively. From VEELS, it was observed that the band-gap is inconsistent along the nanotube length, and that it deviates from that of anatase (3.2 eV) and rutile (3.0 eV). The obtained band-gap of 3.12 eV at the nanotube top and 3.28 eV at nanotube bottom is attributed to the coexistence of anatase and rutile phases even at an annealing temperature of 450 °C.

LIST OF FIGURES

Synthesis of One-Dimensional TiO_2 Nanotube Arrays by Potentiostatic Anodisation

Anele Tshaka

TABLE OF CONTENTS

CHAPTER ONE

Introduction

1.1 Background

Over the years, the field of nanotechnology has received a great deal of attention from researchers in almost all scientific disciplines including Biology, Chemistry, Physics and Engineering, owing to the unique properties acquired by materials at the nanoscale (particle size smaller than 100 nm) [1.1]. Nanotechnology was established a few years after the lecture given by the American theoretical physicist, Richard Feynman during the 1959 American physics society gathering [1.2]. In this lecture, he thought of ways on manipulating individual atoms to the desired atomic arrangements which ultimately resulted in his postulation that

"*It is possible in principle to manufacture nanoscale machines that would enable us to arrange atoms the way we want and do chemical synthesis the way we want*".

This lecture was at the time of no interest to the scientific community since there was no knowledge about the nanoscale properties and the synthesis techniques of nanomaterials. However, through scientific research in the late 20th century, metallic nanopowders for magnetic recording tapes were developed. Since then, further studies on synthesis techniques of nanomaterials and their remarkable properties commenced.

Findings at the time revealed that nanomaterials possess great potential for satisfying the requirement for technological evolution; which is to manufacture electronic and photo-devices with relatively small dimensions with enhanced performance [1.3]. These findings stimulated world-wide research aiming to develop and understand the synthesis techniques of nanomaterials. This led to a successful synthesis of nanoporous aluminium oxide (Al_2O_3) via the low-cost and environmental friendly potentiostatic anodic oxidation of aluminium foil in acidic electrolyte [1.4]. Within the field of material science, the successful synthesis of nanoporous Al_2O_3 intensified research efforts on attempting to synthesise porous oxides

structures on other materials via the electrochemical technique. To date, porous structures are grown on metals that form stable oxide layers on their surfaces when exposed to the atmosphere. As such these oxides are mainly grown on valve-metals such as zinc (Zn), tin (Sn), tungsten (W), titanium (Ti), niobium (Nb), hafnium (Hf) and zirconium (Zr) [1.5- 1.8]. Amongst these metal-oxides, titanium dioxide (TiO_2) is the most studied metal-oxide due to its broad set of outstanding functional properties [1.9].

TiO_2 is the ninth most abundant compound in the earth's crust and it occurs in nature as a white non-combustible and odourless powder, crystal and/or thin film. The formation of TiO_2 is ascribed to the naturally occurring oxidation of titanium ionic species (Ti^{4+} and Ti^{3+}) by reactive oxygen species (ROS) found in the atmosphere. It is classified as a semiconductor material with a wide-energy bandgap ($E_g \approx 3$ eV) and belongs to the family of transitional metals [1.10]. Bulk TiO_2 is known to be non-toxic, environmental friendly and corrosion-resistant material that is frequently used in paints, white pigments and moisturisers [1.11]. In material science, TiO_2 nanostructures (nanorods, nanowires, nanofibers, nanotubes, etc.) especially nanotubes, have been extensively studied due to their excellent electronic properties and exceptional biocompatibility [1.12-1.14]. Recently, TiO_2 nanotubes TiO_2 NTs have been incorporated successfully in technological devices such as in photovoltaics where they provide direct charge transport [1.15].

1.2 Generations of Anodised TiO_2 Nanotubes

Ever since Keller [1.16] reported the basic model of porous aluminium oxide (Al_2O_3) as a hexagonally closed-packed structure that consist of porous and barrier layers, research efforts focused on studying the morphology and the growth mechanism of these structures by means of transmission and scanning electron microscopy [1.17-1.19]. Through the work of Masuda and Fakuda [1.20] it was reported that upon further optimisation of anodisation conditions, an oxide containing highly ordered porous array could be grown. These highly ordered, perfectly aligned Al_2O_3 porous structures were mostly used in photonic crystals and indirectly as template in template based techniques (discussed in section 1.5) to grow porous structures on secondary materials that are deposited inside the porous template material. Amongst the porous

structures grown in such fashion are TiO_2 porous arrays with exceptional optical and surface properties which make them suitable for biological and technological applications [1.21-1.22]. For a long time, it was believed to be impossible to achieve growth of self-organised porous structures of TiO_2 via the anodisation technique. This was attributed to the fact that TiO_2 is chemically very stable, thus it is almost impossible to chemically dissolve. In 1999, Zwilling et al [1.23] reported successful synthesis of self-organised nanoporous structures with thickness of few hundred nanometres by anodising titanium (Ti) alloys in a chromic-acid electrolyte comprising of dilute hydrofluoric (HF) acid. Further studies by means of scanning electron microscope (SEM) revealed that these porous structures have tubular shape with open tops and closed bottom, thus, they are referred to as nanotubes instead of nanopores [1.24-1.26]. Since then, research efforts aiming at developing ways to manipulate the resulting morphologies of nanotubes which would make them of practical use commenced.

In 2001, Gong et al [1.27] reported the first-generation synthesis of TiO_2 NTs with length of up to 500 nm during anodisation of Ti foil in HF aqueous electrolyte. The resulting morphologies of the Gong synthesis are shown in figure 1.1 (a). However, due to the low aspect ratio of the first-generation, they were not of practical use, thus further investigations were required to improve the aspect ratio. Cai et al [1.28] reported second generation synthesis of TiO_2 NTs with enhanced length of up to several micrometers as shown in figure 1.1 (b). This successful synthesis of TiO_2 NTs with enhanced aspect ratio was achieved by tailoring the electrolyte composition, with sodium fluoride (NaF)/potassium fluoride (KF) salt used instead of HF.

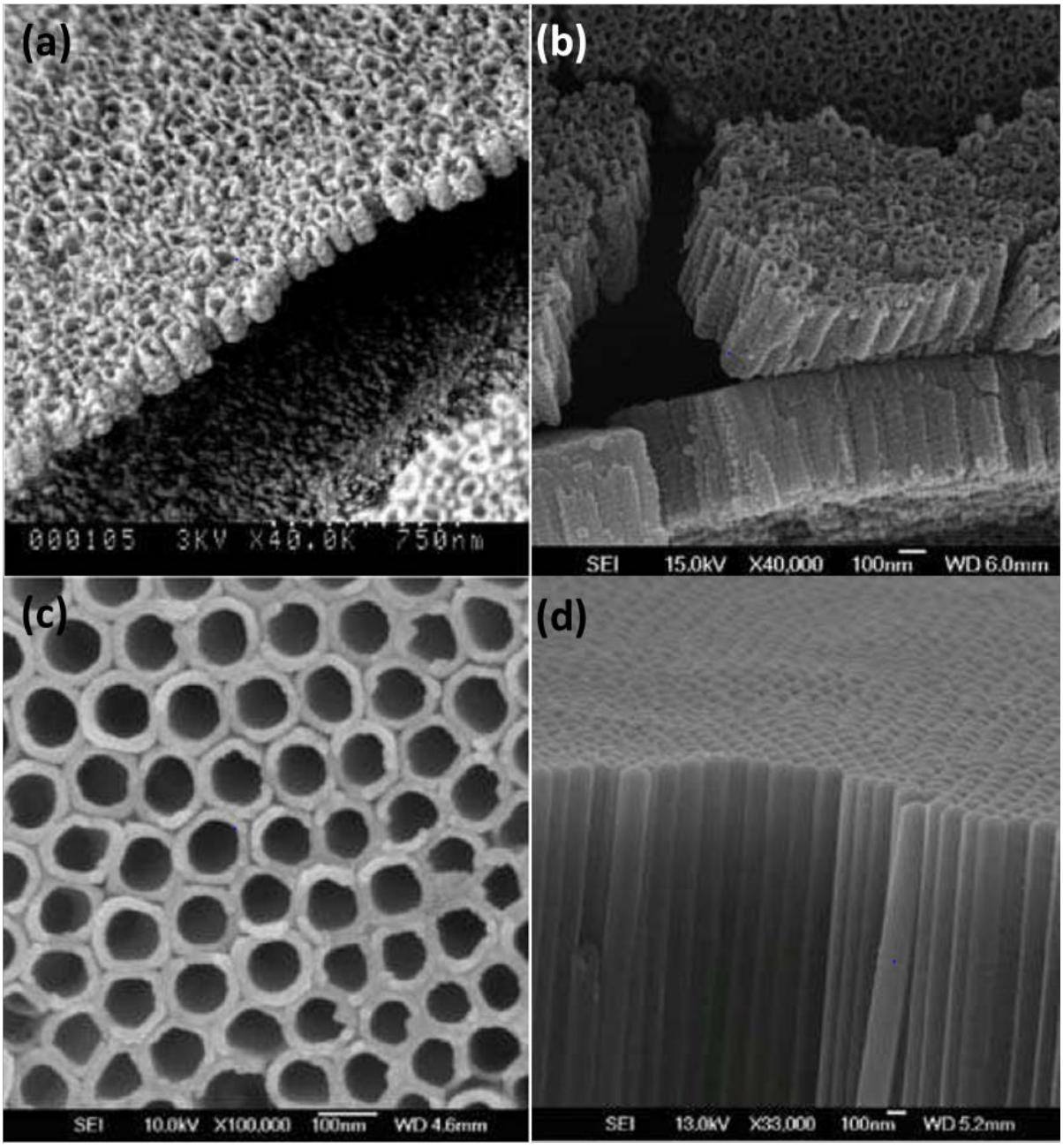

Figure 1.1: Illustration of the morphological and geometrical evolution of TiO2 NTs synthesised via anodisation, (a)-(b) cross-sectional view of Gong and Cai's first and second generation of TiO2 NTs, respectively; (c)–(d) top and cross-sectional view [1.27, 1.28]

The third-generation synthesis was reported by Paulose et al [1.29] where they achieved highly ordered TiO_2 NTs arrays with length of 134 µm via anodisation of Ti in organic electrolyte comprising of ethylene glycol (EG), dimethyl sulfoxide (DMSO) in combination with HF, NaF,

ammonium fluoride (NH_4F) and KF. The resulting morphology of the third-generation TiO_2 NTS is shown in figure 1.1 (c)-(d). Moreover, it turned out that using organic electrolyte (non-aqueous) regimes result in growth of highly ordered TiO_2 NTs arrays with almost perfect hexagonal arrangement with smooth tubes without sidewall inhomogeneity compared to aqueous electrolytes [1.30]. Other reports on the third-generation synthesis focused on further optimisation of the anodisation parameters such as applied voltage, duration, temperature, pH level, concentrations and temperature to achieve much higher aspect ratios [1.31-1.32].

Grimes et al [1.32] proposed the fourth-generation to be synthesis of TiO_2 NTs by anodisation of Ti foil in fluoride-free electrolyte bath. It is known that nanotubes synthesised in first, second and third generations have amorphous crystallographic structure. However, upon post-treatment at elevated temperatures, the TiO_2 NTs walls start to crystallise in anatase phase while the underlying barrier layer crystallises in rutile phase. In general, it is well understood that the electrolyte composition and its pH determine both the nanotube formation rate and the chemical dissolution rate of the oxide. Also, it is a known fact that the applied anodisation potential essentially controls the length-scale of the tube diameter or pore size [1.33]. Notwithstanding this progress achieved over the years in the field, a lot of conjecture remains when discussing the growth model of the different TiO_2 nanotubular structures during the anodisation process (discussed in chapter two, section 2.4). These include a lack of holistic description about the processes taking place in the Ti/electrolyte interface [1.34] and lack of direct experimental evidence to confirm the processes and the reason for their dominance at a given stage [1.35-1.36].

1.3 Properties of TiO_2 Nanotubes

In many publications [1.25-1.28, 1.33] it has been reported that the as-deposited TiO_2 NTs have amorphous crystallographic structure, with post-thermal treatment resulting in the nanotube walls converting into crystalline anatase and the base into the rutile phase. The above mentioned crystalline phases are the most studied phases of TiO_2 and their applications vary due to their distinct structural, electronic and optical properties [1.9]. In this section, properties TiO_2 and comparison based on their functional applications will be discussed. In this thesis, the rutile and anatase phases will be studied.

1.3.1 Crystal Structures of TiO_2

Generally, TiO_2 is known to crystallise in three distinct polymorphs, namely rutile, anatase and brookite. Besides these three polymorphs, there are other synthetic layer phase called TiO_2 (B) [1.37], and some other high-pressure polymorphs [1.38]. However, because the high-pressure polymorphs are of minor significance for research and device application, and because there are no publications reporting traces of brookite phase in TiO_2 NTs structures grown by anodisation, only crystal structures of anatase and rutile will be considered. Rutile and anatase are both tetragonal polymorphs of TiO_2 with six and twelve atoms in their unit cells respectively as shown in figure 1.2 [1.39, 1.40].

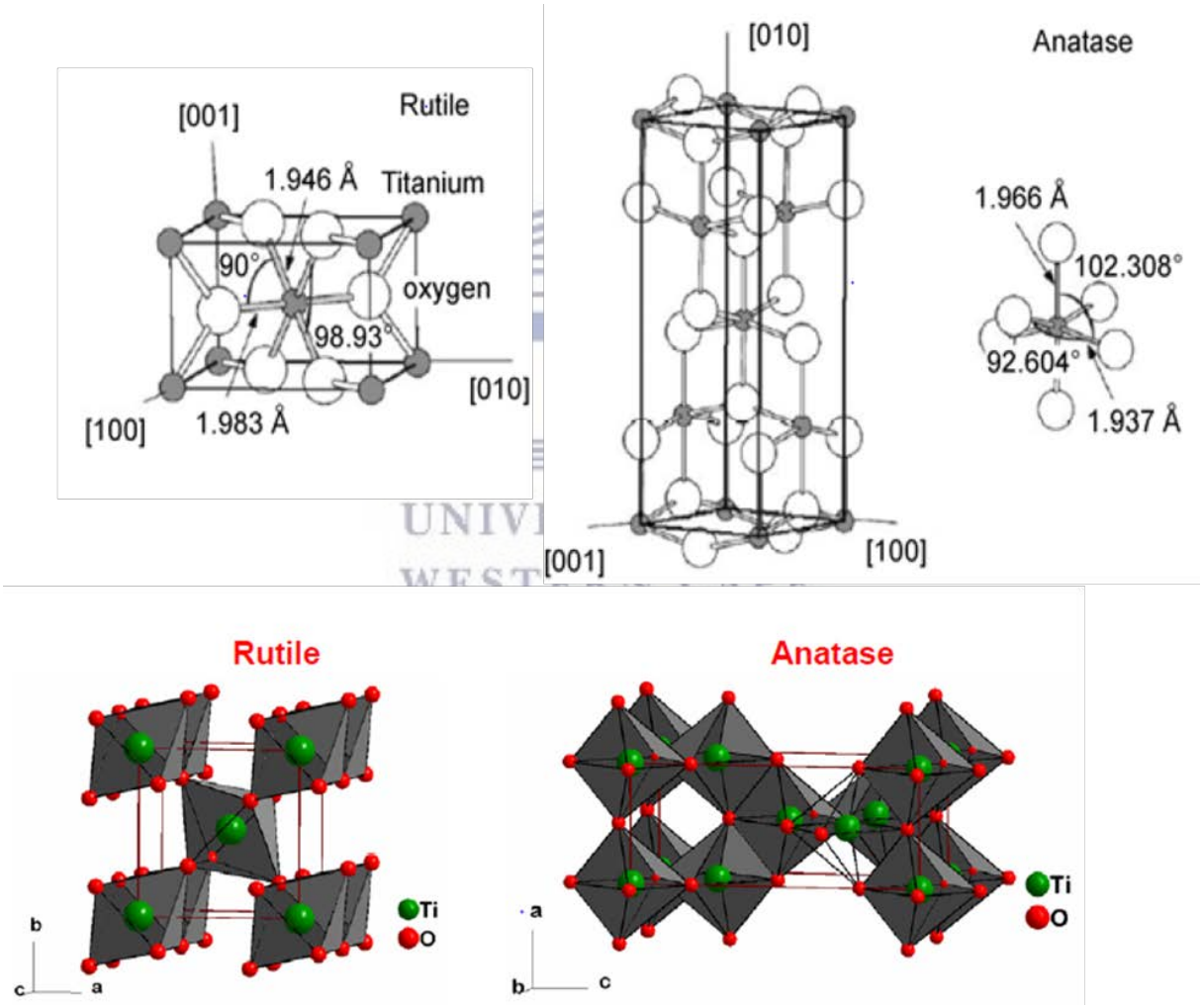

Figure 1.1: Tetragonal unit cells of bulk rutile and anatase structures with stacking of octahedral to form three-dimensional lattice [1.39, 1.40]

The crystal structure of TiO_2 is explained in terms of TiO_6 octahedron with each octahedron made up of six oxygen atoms which surround the titanium atom located at the centre of the octahedral as depicted in figure 1.2 [1.40]. The essential difference between the crystal structure of anatase and rutile lies on the octahedral distortion and octahedral assembly [1.39]. Distortion is caused by the variation in Ti-O bond lengths, where two bonds slightly differ in length compare to the other four and by the O-Ti-O bond angles which deviate from 90° as illustrated in figure 1.2 and summarised in Table 1.1 [1.39,1.40].

Table 1.1: Crystal structure data for TiO_2 anatase and rutile [1.40]

Properties	Rutile	Anatase
Crystal structure	Tetragonal	Tetragonal
Lattice constant (Å)	$a = 4.5936$ $c = 2.9587$	$a = 3.784$ $c = 9.515$
Space group	$P4_2/mnm$	$I4_1/amd$
Molecule (cell)	2	2
Volume/ molecule ($Å^3$)	31.2160	34.061
Density (g cm^{-3})	4.13	3.79
Ti–O bond length (Å)	1.949 (4) 1.980 (2)	1.937(4) 1.965(2)
O–Ti–O bond angle	81.2° 90.0°	77.7° 92.6°

In the rutile phase, the octahedra are joined by sharing two edges to form octahedral assembly which are then interlinked by sharing of one corner with the neighbouring octahedral to form a three-dimensional lattice, whereas in anatase the three-dimensional lattice is formed by sharing of four edges to form the (001) plane which are then connected by corner-sharing with octahedral on the plane below as illustrated in figure 1.2 [1.39-1.41].

Amongst the two TiO_2 polymorphs, rutile is the most thermodynamically stable phase which does not undergo any transformation at very high temperatures, while anatase is the metastable phase of TiO_2 which upon thermal treatment is transformed to the more stable rutile phase [1.11, 1.39]. However, the stability of anatase is particle size dependant as it is believed that at

particle size of less than 20 nm, anatase is considered to be the most stable. Moreover, the presence of foreign ionic species in the lattice of TiO_2 also affects the stability of each phase [1.9, 1.11].

The crystal structure of TiO_2 is a crucial parameter for effectiveness in technological and/or biological application since there is a variation in the material's properties due to crystallisation [1.4]. For example, anatase is preferred over rutile in dye-sensitised solar cells (DSSCs) and in photocatalysis experiments. This is because of anatase's suitable band-edge for charge separation, high charge mobility, low dielectric constant and low density [1.32, 1.43]. However, rutile structure is of importance in gas sensors and it is used as dielectric layers [1.32].

1.3.2 Electrical and Optical Properties of TiO_2

a) Electrical Properties - Semiconductors

A semiconductor is a material that behaves as an insulator at low temperatures and as a good conductor when sufficient energy is supplied. The electrical properties of these materials are explained in terms of their energy bands; namely the valence band (V_B) and the conduction band (C_B) that are separated by energy band-gap (E_G) of more than 2 eV as shown in figure 1.3(a) [1.44, 1.45]. At low temperatures, V_B is the highest filled band while the C_B is the lowest filled band with fermi-energy (E_F) situated in the centre of the E_G. When the material is illuminated with photon energy (*hf*) that equals or greater than the E_G, an electron from the V_B will be excited to the C_B leaving behind a positively charged particle that is referred to as "hole" as depicted in figure 1.3(b). The electron in the C_B then gets transported to the external circuit thereby producing electric current. Meanwhile, a hole in the V_B is replaced by an electron resulting in movement of holes in the V_B which also contribute to the conductivity of the material. Such types of pure semiconductor material depicted in figure 1.3 (b) with direct E_G called intrinsic semiconductors and have equal number of charge carriers (electrons and holes). This means that the number of electrons in the C_B equals to the number of holes in the V_B. The conductivity of an intrinsic semiconductor material can only be increased by irradiating the material with highly energetic photons. However, this may result in material damage, thus an alternative treatment in employed to increase the material's conductivity [1.44, 1.52].

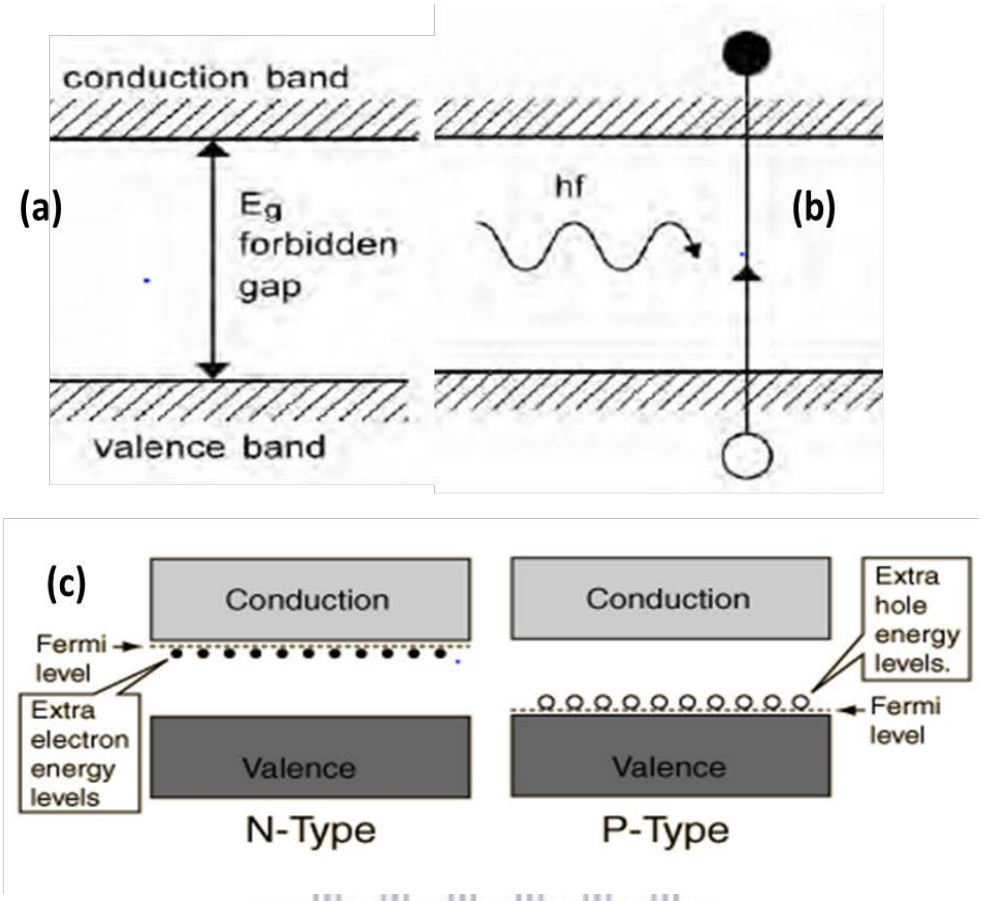

Figure 1.1: Schematic band structures for both intrinsic and extrinsic semiconductors with (a) pure semiconductor, (b) photoexcitation of e-h pairs, and (c) doped semiconductor with induced donor and acceptor levels in n-type and p-type materials respectively [1.45]

Another type of semiconductor has indirect E_G and exists in two types; p-type and n-type with enhanced conductivity at optimal condition. The indirect E_G forms as result of introduction of foreign atom (dopant) with one more or less valence electron into the lattice of the semiconductor material. This process is called "doping" and is used to manipulate the conductivity of the material by introduction of energy states in the E_G which can either be a "donor level" or "acceptor level" depending on the dopant used. As shown in figure 1.3(c), the acceptor level near the V_B exist as a result of introduction of dopant with one less valence electron, thus causing the material to have an excess of holes. Such materials are known as p-type semiconductors with majority charge carriers being holes and minority being electrons. If the material is doped with dopant of one more electron, a donor level situated just below the C_B is introduced into the forbidden zone. Doping result in shift of E_F to be situated between the induced donor and acceptor states. Furthermore, doping makes the material to be conductive

even at relatively low temperatures, thus when operated at high temperatures, it behaves the same as the intrinsic semiconductor [1.44].

b) Semiconductor Properties of TiO_2

TiO_2 is a large band semiconductor with relative energy levels that form its band structure being that of Ti-3d states and oxygen (O)-2p states [1.42]. The V_B of TiO_2 is composed of O-2p states hybridised with Ti-3d states, while the C_B is mainly Ti-3d states [1.46]. Depending on its crystallization, TiO_2 has indirect E_G of 3.2 eV when in anatase form and 3.0 eV in rutile [1.47, 1.48]. Of importance in TiO_2 structure are the oxygen vacancy states and Ti^{3+} states which have large impact on the electrical and optical properties of TiO_2. In vacancy states occupied by O^{2-} anions (charged vacancy state) in TiO_2 regular lattice, one or two electrons localises in the vacancy states, forming a donor level in the band-structure of TiO_2 located at 0.75 - 1.18 eV below the C_B, as shown in figure 1.4 [1.49].

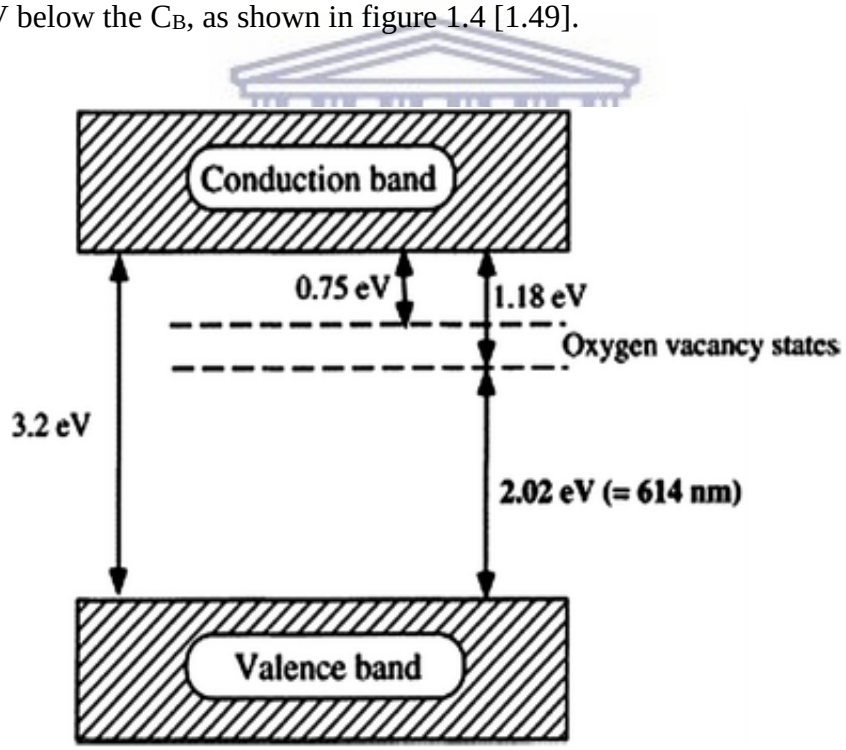

Figure 1.2: A proposed band-structure model for anatase with oxygen vacancy states [1.50]

Although figure 1.4 illustrates the proposed band structure for anatase phase, the same is observed in rutile. It has been demonstrated for both rutile and anatase that an increase in oxygen vacancies results in an increase in these donor states which in the case of highly

deficient anatase they can overlap the conduction band [1.51]. On the other hand, the Ti^{3+} states located at 0.2-0.8 eV below the C_B (not shown in figure 1.4) acts as electron trapping sites which can easily transfer the trapped electron into the nearby C_B. Hence, they dominate the conductivity of the TiO_2 crystals [1.42].

c) Semiconductor – Electrolyte Interface

In technological applications such as photovoltaics and photocatalysis, TiO_2 NTs are used in environments where they will be in contact with a solution (electrolyte). Upon contact with electrolyte, semiconductor materials are subject to a change in band geometry, which either results in upward or downward bending of band edges in p-type and n-type semiconductor respectively. The description of this phenomenon is based on three assumptions: (1) the semiconductor material is ideally crystalline with energetically discrete, homogeneous and completely ionised donor states near C_B, (2) no surface defects and (3) Helmholtz layer is neglected. [1.52].

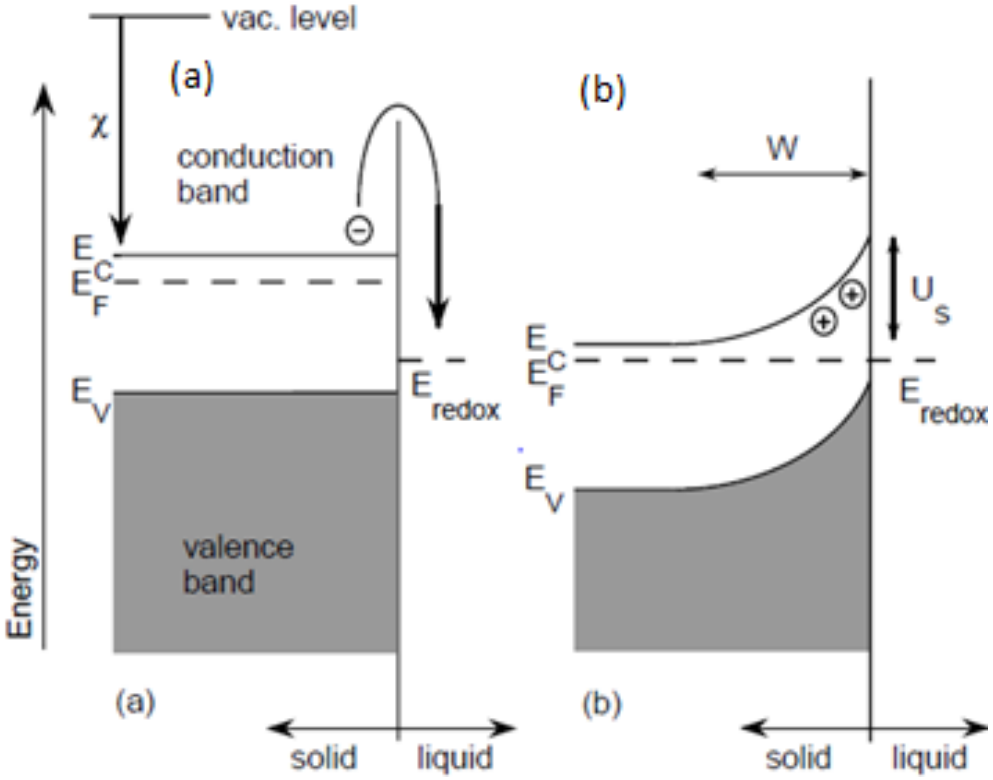

Figure 1.3: Energetic situations at n-type semiconductor/ electrolyte interface (a) before contact and (b) after contact [1.21]

When the n-type semiconductor material, for example TiO_2, is in contact with an electrolyte whose conductivity is higher than that of the semiconductor, the E_F of the semiconductor material readjusts until it equals that of the electrolyte, hence thermal equilibrium is achieved when fermi-energies coincide. During the equilibration process, electrons are being transferred at the semiconductor-electrolyte interface resulting in the formation of the space charge layer "*W*", which generates an electric field as observed in figure 1.5 (b). The generated electric field in the space charge region is ascribed to the observed band-bending, thus the formation of the Schottky barrier layer [1.53]. The Schottky barrier layer offers the material with diode behaviour; hence it enhances photocatalytic activity [1.11].

d) Optical Properties of TiO_2

For photovoltaic and photocatalysis applications, one of the major requirements is the material's ability to absorb sufficient light to generate large number of electron-hole (e-h) pairs. Because TiO_2 has a very wide E_G, the material can only absorb sufficient energy to generate e-h pairs in the ultraviolet (UV) region. However, the presence of oxygen vacancies in the regular TiO_2 lattice has extended the absorption into the visible region by means of induced local states near C_B. As previously mentioned, the increase in the number of oxygen vacancies result in an increased number of local states inside E_G just below the C_B. This however, forms the basis for manipulating optical properties of TiO_2 by introducing oxygen vacancies [1.42].

Doping TiO_2 with foreign atoms such as vanadium (V), chromium (Cr) and nitrogen (N) [1.54] has been the commonly practised band-gap engineering to enhance photoresponse in the ultraviolet-visible (UV-Vis) range. Doping with N via ion-implantation has been, to date, reported as the most efficient treatment which narrows the E_G by formation of $Ti_xO_yN_z$ states just above the V_B [1.9]. However, as a consequence of ion bombardment, TiO_2 NTs become amorphous and require annealing to re-establish crystallinity. Results shown in figure 1.6 illustrate the broadening (peak-shift) of photoresponse (induced photo-current) towards the visible region as result of doping TiO_2 NTs with N at different concentrations. The effectiveness of N-doping in enhancing photoresponse is observed at doses of 10^{16} ions cm^{-2} while fewer concentrations showed no real effect in photoresponse [1.9].

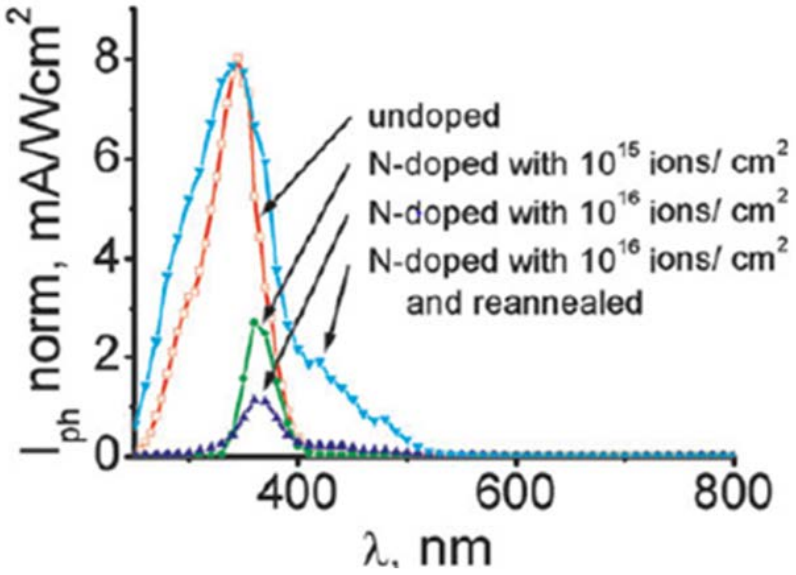

Figure 1.4: Photo-current spectra of Undoped and N-doped TiO2 via ion-implantation at different concentrations [1.9]

1.4 Functional Applications of TiO_2 Nanotubes

1.4.1 Photocatalysis

Photocatalysis is an accelerated photoreaction in the presence of a semiconductor material which acts as a catalyst in the reaction [1.55]. TiO_2, amongst all other semiconductor materials used for catalysis, is the most active photocatalytic material owing to its suitable band-edge position relative to the typical environment (such as water). Its C_B is situated at higher energies than the oxidised states of the environment while the V_B is situated at lower energies than the reduced states of the environment. This band arrangement permits the transportation of photo generated e-h pairs into the electrolyte where they participate in photocatalytic reactions. Moreover, because TiO_2 is non-toxic, cost effective, highly corrosion resistant with superior photo-reactivity and has long-term chemical stability, it is the preferred photocatalytic material over others such as gallium arsenide (GaAs), lead-sulphide (PbS), zinc-oxide (ZnO) and cadmium-sulphide (CdS) [1.56 - 1.58].

Two main research interests in photocatalysis include the applications in water decomposition [1.59] and degradation of environmental pollutants [1.60]. The use of vertically aligned TiO_2 NTs as ideal catalyst for both applications instead of conventionally used TiO_2 nanoparticles

has enhanced photocatalytic activity drastically. This is attributed to the hollow nature of TiO_2 NTs which offers direct charge transport route compared to that offered by nanoparticles as shown in figure 1.7 [1.61]. Thus, the use TiO_2 NTs reduces the losses incurred by charge trapping sites across nanoparticle boundaries [1.62].

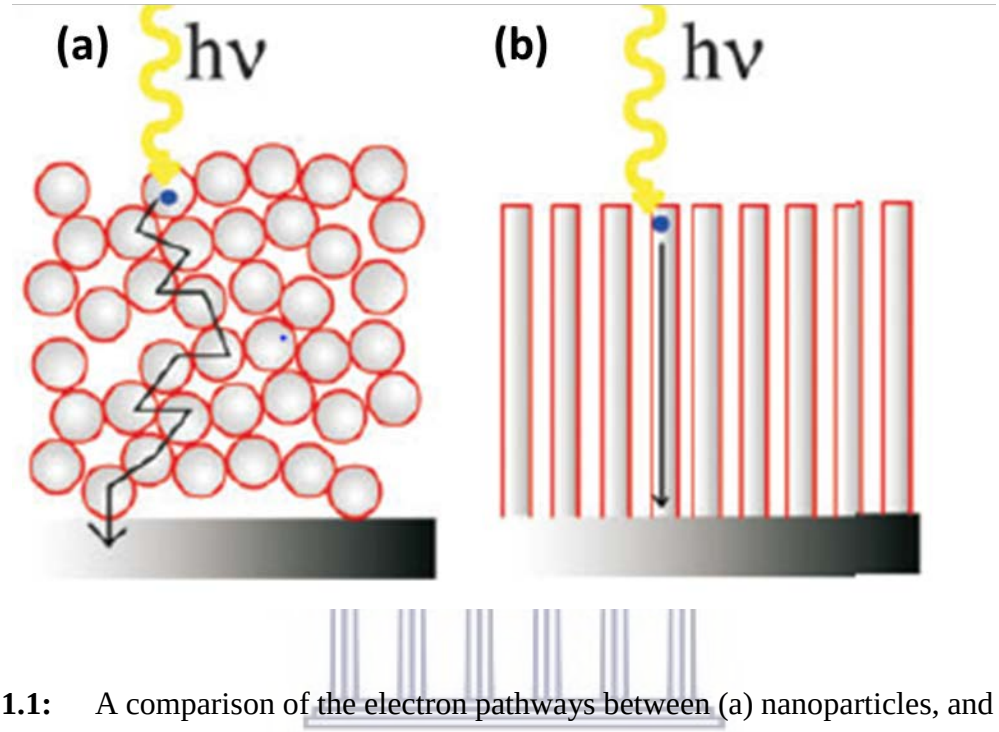

Figure 1.1: A comparison of the electron pathways between (a) nanoparticles, and (b)TiO2 NTs [1.9]

1.5.2 Principle of Water-Decomposition and Hydrogen Generation

Upon irradiating a photocatalyst, for example TiO_2 NTs in an ideal photo-electrochemical cell as shown in figure 1.8 with UV-Vis light, electrons are excited from V_B into the C_B leaving behind holes [1.63]. The photogenerated e-h pairs are then separated by the electric field present in the Schottky barrier that is formed during the contact of TiO_2 NTs with the environment (water). Holes (h_{vb}) from the V_B are injected into the environment while electrons (e_{cb}) in the C_B are driven deep into surface of the catalyst [1.11, 1.63].

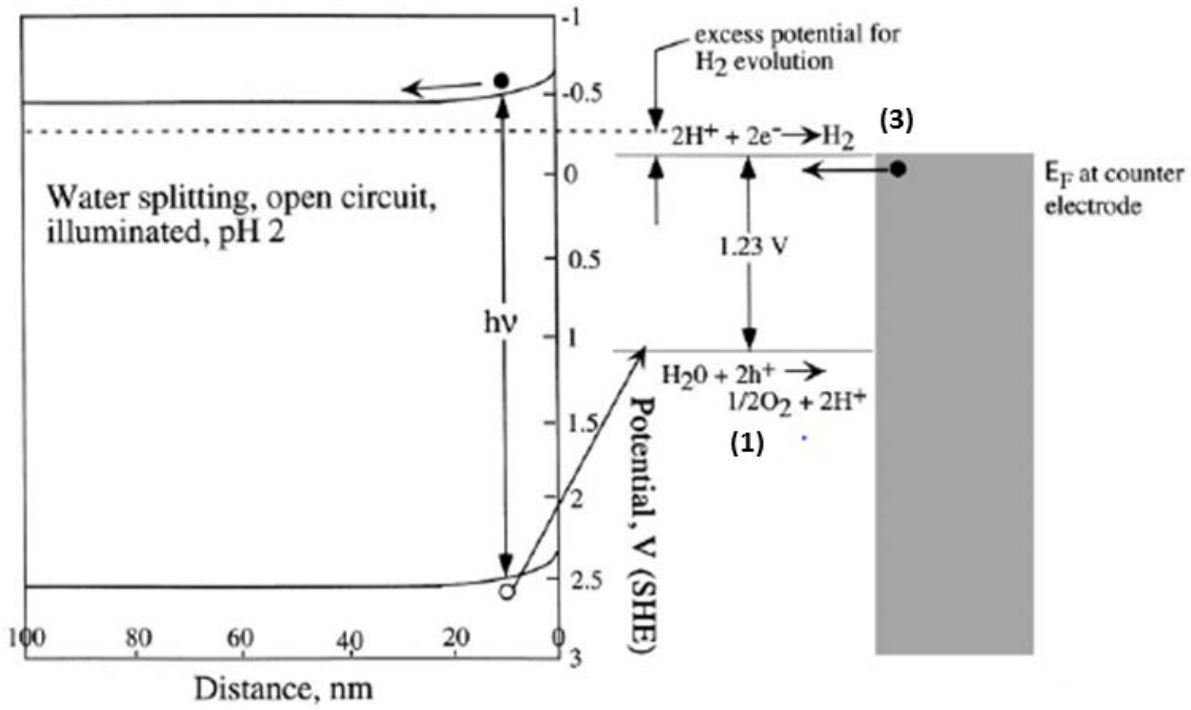

Figure 1.2: A schematic representation of photo-electrochemical water-decomposition using an illuminated oxide semiconductor (such as TiO2 NTs) with electrochemical scale [1.64].

Because of the high oxidising ability of the injected h_{vb}, they oxidise water molecules at the cathode surface thereby splitting water into oxygen (O_2) and hydrogen (H^+). The formation of e-h pairs and the occurring photocatalytic reactions are summarised in equations 1.1- 1.3 [1.65, 1.66]:

$$TiO_2 + UV - Vis\ light\ (energy) \rightarrow e_{cb}^- + h_{vb}^+ \quad (1.1)$$

$$H_2O\ (water) + 2h_{vb}^+ \rightarrow \frac{1}{2}\ O_2 + 2H^+ \quad (1.2)$$

$$2H^+ + 2e_{cb}^- \rightarrow H_{2\ (gas)} \quad (1.3)$$

When the C_B of the catalyst material is at higher or more negative potential on electrochemical scale than hydrogen evolution potential, the photogenerated electrons flow to the cathode material and reduce protons to form hydrogen gas as described by (1.3) [1.66]. With appropriate laboratory setup, the generated hydrogen gas can be extracted and stored, preferably in tanks for use as alternative fuel for fossil fuels.

1.4.3 Degradation of Pollutants

In the absence of the cathode material and the presence of unwanted pollutants in environment such as water, irradiating the photocatalyst-environment system with UV-Vis light results in additional reactions to those mentioned for water-decomposition and hydrogen generation. The photogenerated e-h pairs react with water molecules to form superoxide (O_2^-) and hydroxyl (OH) species at V_B and C_B of the photocatalyst, respectively. The reactions are summarised in equation (1.4) - (1.8) [1.65]:

$$H_2O\ (water) + h_{vb}^+ \rightarrow OH + H^+ \quad (1.4)$$

$$O_2 + e_{cb}^- \rightarrow O_2^- \quad (1.5)$$

$$h_{vb}^+ + pollutant \rightarrow pollutant^+ \rightarrow degradation\ products \quad (1.6)$$

$$O_2^- + pullutant \rightarrow degradation\ products + CO_2 \quad (1.7)$$

$$OH + pullutant \rightarrow degradation\ product + CO_2 \quad (1.8)$$

The formed superoxide and hydroxyl in (1.4) and (1.5) interact with pollutant such as organic material causing mineralisation as shown in figure 1.9 and the occurring reactions are described by equation (1.7) and (1.8). This consequently results in a complete degradation of pollutants to carbon dioxide and degradation products such as mineral acid [1.11, 1.56].

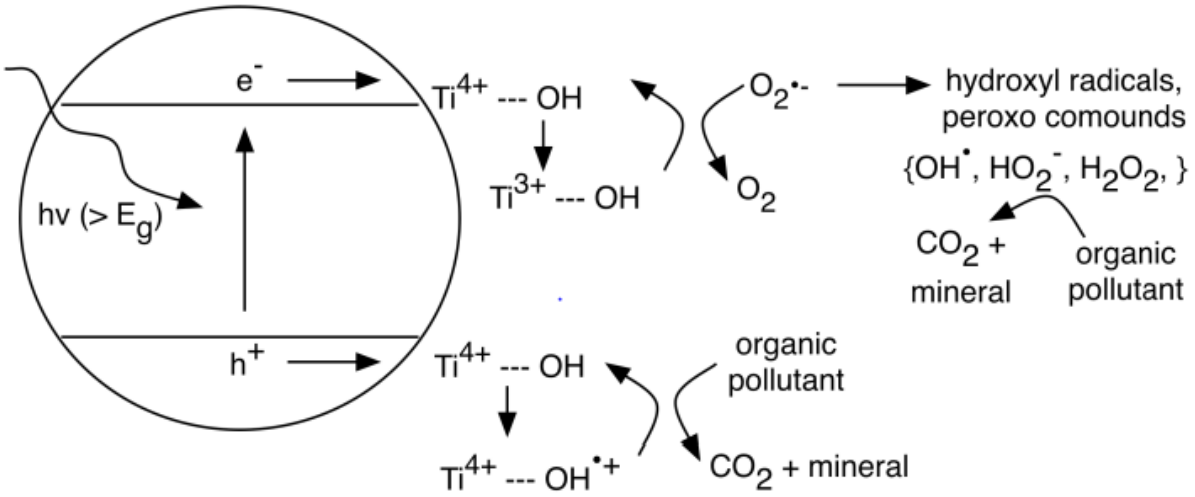

Figure 1.3: Photo-oxidative degradation of pollutants through interaction with surface bound hydroxyl radicals [1.63].

1.4.4 Photovoltaic Dye-Sensitised Solar Cells

The DSSC is a device that converts solar energy into electrical energy. The five components of a typical include; (i) a transparent conducting oxide (TCO) glass substrate, (ii) a semiconductor material, (iii) a sensitiser adsorbed onto the surface of a semiconductor, (iv) an electrolyte containing redox mediator and (v) a counter electrode such as platinum (Pt) that is responsible for the regeneration of the mediator [1.67, 1.68]. Ever since the first report of fabrication of DSSCs by Grätzel and O'Regan in 1991 [1.69], TiO_2 in form of nanoparticles has been the preferred semiconductor material because of its stability even at extreme conditions with suitable C_B position which lies slightly below excited states energy levels of many dyes [1.42].

However, the use of TiO_2 nanoparticles in DSSCs is associated with several disadvantages which include long carrier diffusion path as shown in figure 1.7(a), interfacial recombination of electrons at semiconductor-dye interface [1.11] and the recombination of electrons at grain boundaries due to the presence of trapping sites [1.11, 1.32]. Thus, TiO_2 NTs have recently been the preferred nanostructures for use as photoanodes in DSSCs. This is ascribed to their one-dimensional nature which permits direct electron transport route with low surface defect (recombination sites) [1.9, 1.11, 1.32, 1.42]. Figure 1.10 illustrates the assembly of the incorporated TiO_2 NTs and the basic operating principle of DSSCs [1.67].

During light-to-electron conversion in the DSSC a dye molecule absorbs photon energy and excite electrons from the highest occupied molecular orbit (HOMO) into the lowest unoccupied molecular orbit (LUMO) [1.11, 1.32]. Because TiO_2 has a suitable C_B position with respect to the LUMO level, the excited electrons are injected into its C_B. The injected electrons are then transported through the one-dimensional route; as depicted in figure 1.7(b) to the back contact before they are conducted to the external load. Resulting from photoabsorption, the oxidised dye is reduced back to its original state by the presence of redox species such as iodide or triiodide in the electrolyte. In turn, the iodide is regenerated at the photocathode with Pt acting as catalyst [1.11, 1.42, 1.67-1.68].

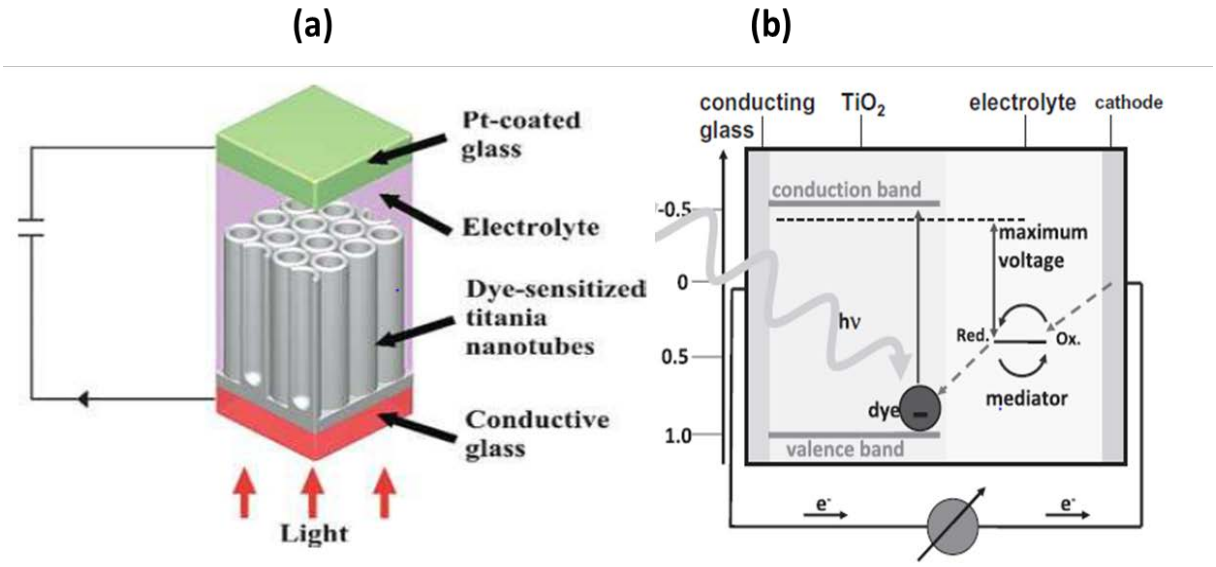

Figure 1.4: Schematic representations of (a) dye-sensitized solar cell assembly and (b) its basic operation principle [1.32, 1.67].

However, there are efficiency limiting factors in TiO_2 NTs based DSSCs such as the insufficient specific surface area for dye-loading compared to nanoparticles. Of recent, many studies [1.70-1.73] focus on improving the surface area of tube systems by either mixing TiO_2 NTs with TiO_2 nanoparticles and/or by synthesising TiO_2 NTs with geometries of increased surface area for dye-loading.

1.5 TiO_2 Nanotubes Arrays: Synthesis Techniques

To date, a commonly used technique to synthesise TiO_2 nanotubes is the anodisation technique (discussed in chapter two, section 2.2). Prior to the use of this technique, there were other synthesis techniques namely template-based that includes assisted template method [1.73-1.74], hydro/solvothermal [1.75] and sol-gel techniques [1.76], as well as atomic layer deposition (ALD) [1.77]. The use of these techniques to synthesise nanotube arrays follow after Hoyer [1.73] reported the synthesis of TiO_2 NTs via the assisted template method. This method uses highly ordered nanoporous anodic aluminium oxide (AAO) with uniform dimensions (pore-diameter and length) and it is divided into two types namely the positive and negative template synthesis.

1.5.1 Positive versus Negative Template Approach

Hoyer in his experiment employed the positive template approach where the amorphous TiO_2 was electrochemically deposited on the outer surface of the AAO template [1.73, 1.78]. After the synthesis duration elapsed, the AAO was then etched using acetone. The resulting TiO_2 NTs revealed crystallization after post treatment and had length of 8 μm, inner and outer diameter ranges of 70-100 *nm* and 140-180 nm respectively [1.79]. Lee et al. [1.79] demonstrated the growth of TiO_2 NTs without using chemical medium for the dissolution of ZnO nanorods that served as template material during synthesis. Because ZnO easily dissolve in water [1.56], the removal of the ZnO nanorods to obtain nanotubes was achieved as a result of its reaction with hydrogen ions (H^+) during the liquid vapour deposition of TiO_2.

Another interesting assisted template technique that employs the positive template method is the sol-gel technique. This technique uses a chemical solution (sol) comprising of Ti precursor in liquid phase that is to be converted into a solid-gel phase by means of hydrolysis and polymerisation [1.80]. When in the gel phase, the removal of the remaining liquids is achieved by a process called “drying” that is then followed by dissolution of the template material. The latter results in the formation of uniform TiO_2 NTs with morphologies that can be tailored by using a template with desired geometry. Qiu et al [1.81] employed sol-gel technique using ZnO nanorods as the active template to synthesise TiO_2 nanotubes. The resulting nanotube arrays had inner diameter range of 100- 120 nm and length of 1.5 μm as shown in figure 1.11 (a) and (b) respectively.

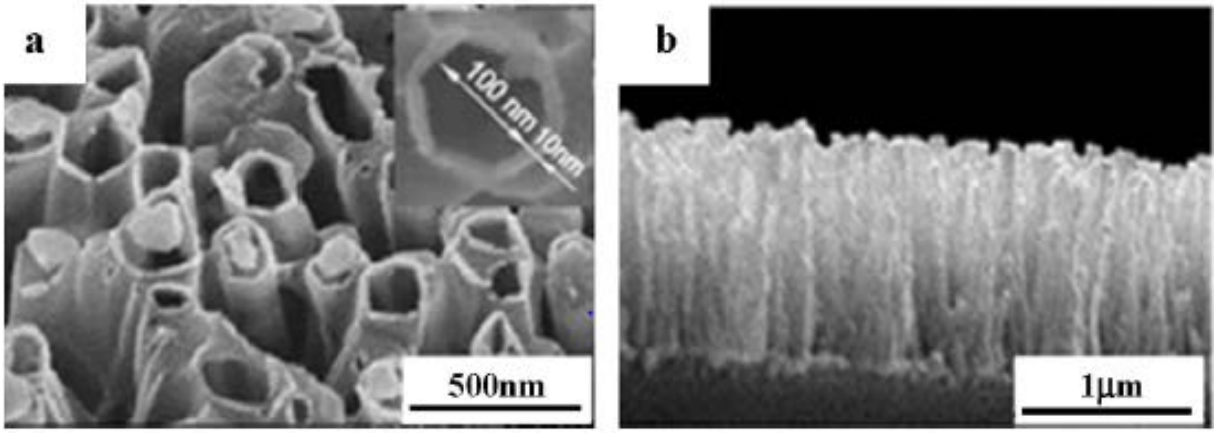

Figure 1.1: FESEM images of Qui et al [1.80] TiO2 nanotubes after chemical etching of ZnO nanorods (a) Top-view and (b) Cross-sectional view [1.81]

1.5.2 Negative Template Approach

The negative template approach is very similar to the positive template approach, but with a slight difference being the deposition of oxide material on the template surface. In the negative template approach, the oxide material is deposited on the inner surface of template pores and the TiO_2 NTs obtained in this approach acquire excellent uniformity in diameter and length compared to those obtained from positive template approach. In addition to the uniformity of grown nanotubes, the obtained morphology reflects true dimensions (length and diameter of the used template material [1.79]. Zheng et al [1.82] employed the sol-gel method using the AAO as negative template to successfully synthesise TiO_2 NTs with enhanced diameter of 200 nm and the length of 8 µm.

It is noted that the negative template approach produces uniform nanotube array with the morphology of both approach being highly dependent on the morphology of the template material used. However, there are disadvantages of using assisted-template approach when synthesizing TiO_2 nanotubes. These disadvantages include the induced contamination during dissolution of the template, long duration and cumbersome process for prefabrication and removal of template. Hence other techniques are also investigated [1.79].

1.6 Motivation for this Study, Aims and Thesis Outline

As previously mentioned, although the TiO_2 nanotube formation during the anodisation process is well documented, a clear description of the crystalline evolution throughout the nanotube remains lacking, even though it has been shown by various studies [e.g. 1.30 – 1.35] to exist as a hybrid anatase/rutile structure post annealing. In addition, a clear understanding of how this peculiar crystallinity affects the localised opto-electronic properties, which, as discussed through sections 1.2 to 1.5 above, are crucial to quantify before application in the broad spectrum of devices, remains unexplored.

Scanning transmission electron microscopy coupled electron energy loss spectroscopy (STEM-EELS) provides a powerful means of not only detecting and quantifying the valence states, coordination and site geometry in transition metal-oxides, but also the localised electronic structure-related optical behaviour, or the so-called opto-electronic properties, such as the

bandgap. In a typical EELS spectrum, the local environment of the metallic and oxygen atoms is characterised by a fine structure of the onset of the respective ionisation edges. This is known as electron energy-loss near edge fine structure (ELNEFS). During ELNEFS analyses the $L_{3,2}$ peak (called edge in EELS terminology) of the 3d transition metals contain information about the valence state, coordination and site symmetry of the central atom (as discussed in section 1.3.1). The L_3 edge originates as a result of electron transitions from the inner $2p_{3/2}$ orbitals to empty 3d orbitals in the metal, whereas the L_2 edge originates from $2p_{1/2} \rightarrow$ 3d electron transitions [1.41].

In the case of TiO_2 the near-edge structures found in the $L_{3,2}$ edges mainly reflect the covalent bonding states resulting from direct and/or indirect interactions between O and Ti atoms. The ELNEFS of both rutile and anatase TiO_2 is well documented [1.41]. Various studies on the ELNEFS of TiO_2 have tried to quantify the valence state of various forms of titania, the local site coordination, as well as the concentration of crystalline versus amorphous phases present in powdered forms of TiO_2 nanoparticles [e.g. 1.85]. Anodised TiO_2 nanotube arrays offer a very interesting network of intercalated nano-crystals of TiO_2, compacted in a tube form, separated by weakly interacting Van der Waals forces [1.30]. As is the case for most nanocrystals, this intertwined network of nano-sized anatase and rutile crystals offer interesting localised properties, often causing debate around their effect on the measured bulk properties. As such, in this study, STEM-EEL spectroscopy coupled with spectral imaging formed the core investigative tool to probe the nano-scale properties of the various synthesised TiO_2 nanotube arrays. To date, this is the first such study on this interesting nanomaterial, following up from the work previously published by our group [1.35].

In particular, this study aimed at developing an understanding of crystallographic phase transformation along the nanotube length after post-thermal treatment of the grown TiO_2 NTs, at elevated temperatures. To investigate the factors that affect the resulting morphology of TiO_2 NTs during anodisation, three different electrolyte regimes were used, allowing the study to briefly touch on the effect of the experimental conditions on the growth of the nanotubes. Complementary to the STEM-EELS, electron microscope was used to study the morphology, elemental composition, crystal structures of the material, whereas x-ray diffraction was used for bulk characterisation of the nanotube crystal structure.

The thesis is outlined as follows:

Chapter One provided some background on the establishment of the field of nanotechnology followed by a brief discussion of the discovery and the evolution of anodised TiO_2 NTs. The chapter also emphasised the most important properties and two main functional applications of TiO_2 NTs.

Chapter Two will detail the generally accepted growth model of TiO_2 NTs during anodisation and summarise the experimental techniques used for the preparation of electrolytes, TiO_2 nanotube synthesis and the in-house experimental setup used.

Chapter Three will focus on the characterisation techniques used to perform the desired investigations with emphasis on electron microscopy and in particular electron energy loss spectroscopy.

Chapter Four will cover the most important results obtained during the course of this study, with in-depth discussion of the morphology, crystallinity, elemental composition, and electronic properties presented.

Lastly, **Chapter Five** will summarise the major findings and future work.

References

[1.1] G. L. Hornyak, H. F. Tibbals, J. Dutta and J. J. Moore, 2009, "Introduction to nanoscience and technology", Taylor & Francis Group, London, United Kingdom

[1.2] R. P. Feynman, 1959, "Plenty of room at the bottom", Transcripts of the American Physics Society Meeting, Available at: http://www.pa.msu.edu/~yang/RFeynman_plentySpace.pdf [Accessed: 24 January 2017]

[1.3] P. S. Anton, R. Silberglitt and J. Sneider, 2001, "The global technology revolution", Rand Publishers, Arlington, United States of America

[1.4] J. M. Macak, 2008," Growth of self-organised titanium dioxide nanotube layers" Unpublished PhD Thesis, University of Erlangen-Nuremberg, Nuremburg, Germany

[1.5] A. Umar, 2010, "Metal-oxide nanostructures and their Applications", (Unpublished PhD Thesis), Najran University, Najran, Saudi Arabia

[1.6] H. Tshuchiya and P. Schmuki, Electrochem. Commun. 07 (2005) 49

[1.7] I. V. Sieber, B. Kannan and P. Schmuki, Electrochem. Solid-State Lett. 08 (2005) J10

[1.8] I. V. Sieber and P. Schmuki, J. Electrochem. Soc. 152 (2005) C639

[1.9] A. Ghichov and P. Schmuki., Chem. Commun. 10 (2009) 2791

[1.10] A. Fujishima, T. N. Rao and D. A. Tryk, J. Photochem. Photobiol. C (2000) 1

[1.11] P. Roy, S. Berger and P. Schmuki, Angew. Chem. Int. Ed. 50 (2011) 2904

[1.12] C. M. Lieber, Solid State Commun. 107 (1998) 607

[1.13] N. R. Rao, A. Muller and A.K. Cheetham, 2006, "The Chemistry of Nanomaterials: Synthesis, Properties and Applications", Wiley -VCH, Weinheim, Germany

[1.14] C. Weisbuch and B. Vinter, 1991, "Quantum Semiconductor Structures Fundamentals and Applications", Elsevier, Amsterdam, The Netherlands

[1.15] J. M Macak, Hildebrand, U. M Jahns and P. Schmuki, Electroanal. Chem. 10 (2008) 1016

[1.16] F. Keller, M. S. Hunter and D. L. Robinson, J. Electrochem. Soc. 100 (1953) 411

[1.17] J. P. O' Sullivan and G. C. Wood, Proc. of the Royal Society of London, Series A – Mathematical and Physical Sciences, 317 (1970) 511.

[1.18] E. Thompson and G.C. Wood, Nature 290 (1981) 230

[1.19] G. Thompson and G. C. Wood, 1983, "Treatise on materials science and technology", Academic Press, New York, USA

[1.20] H. Masuda and K. Fukuda, Science 268 (1995) 1466

[1.21] J.M Macak., 2008, "Growth of Anodic Self-Organized Titanium dioxide nanotube layers" (Unpublished PhD Thesis), Nuremberg, Germany

[1.22] T. Shokuhfar, 2010, "Structural and Surface property Characterisation of Titanium Dioxide nanotubes for Orthopaedic Implants", (Unpublished PhD Thesis), Michigan University of Technology, Ann Arbor, USA

[1.23] V. Zwillig, M. Aucouturier and E. Darque-Ceretti, Electrochim. Acta. 45 (1999) 921

[1.24] R. Beranek, H. Hildebrand and P. Schmuki, Electrochem. Solid-State Lett. 6 (2003) B12

[1.25] J. M. Macak, K. Sirotna and P. Schmuki, Electrochim. Acta. 50 (2005) 3679

[1.26] J. M. Macak, H. Tsuchiya and P. Schmuki, Angew. Chem., Int. Ed.44 (2005) 2100

[1.27] D. Gong, C. A. Grimes, O. K. Varghese, W. Hu, R. S. Singh, Z. Chen and E. C. Dickey, J Mater Res. 16 (2001) 3331

[1.28] Q. Cai, M. Paoulose, O.K. Varghese, C.A. Grimes, J Mater Res. 20 (2005) 230

[1.29] M. Paulose, K. Shankar, S. Yoriya, H. E. Prakasam, O. K. Varghese, G. K. Mor, T. A. Latempa, A. Fitzgerald and C. A. Grimes., J Phys. Chem. B, 110 (2006)16179

[1.30] J. M. Macak, H. Tsuchiya, L. Taveira, S. Aldabergerova and P. Schmuki, Angew. Chem. 117 (2005) 7629

[1.31] K. Shankar, G. k. Mor, H. E. Prakasam, S. Yoriya, M. Paulose, O. K. Varghese and C. A. Grimes. Nanotechnology 18 (2007) 065707

[1.32] C. A. Grimes and G. K. Mor, (2009)," TiO_2 Nanotube Arrays- Synthesis, Properties and Applications", Springer Science + Business Media. New York

[1.33] O. K. Varghese, D. Gong, M. Paulose, K. G. Ong, E. C. Dickey and C. A. Grimes. Journal of Materials Research 18 (2003)156

[1.34] S Bauer, S Kleber, and P. Schmuki. Electrochem. Commun., 8 (2006) 1321

[1.35] F. R. Cummings, T. F. G Muller, G. F Malgas and C. J Arendse, Journal of Physics and Chemistry of Solids 85 (2015) 278

[1.36] Y. Zhang, D. Yu, M. Gao, D. Li, Y. Song, R. Jin, W. Ma and X. Zhu, Electrochimica. Acta 160 (2015) 33

[1.37] R. Marchand, L. Broham and M. Tournoux, Mater. Res. Bull. 15 (1980) 1129

[1.38] J. Muscat, V. Swany and N. M. Harrison, Phys. Rev. B, 65 (2002) 224112

[1.39] A. Gjevori, 2010, "Phase Formation of Photoactive TiO2 Thin Films by Metal Plasma Immersion Ion Implantation and Deposition", Unpublished MSc. Thesis, University of Tirana, Albania

[1.40] D. T. Cromer and K. Herrington. J Am Chem Soc. 77 (1955) 4708

[1.41] R. Brydson, H. Sauer, W. Engel, J. M. Thomas et al., Condens. Matt. 1 (1989) 797

[1.42] S. M. Gupta and M. Tripathi, Chinese Sci. Bull. 56 (2011) 1639

[1.43] O. Carp, C.L Huisman and A. Reller, Prog. In Solid State Chem. 32 (2004) 33

[1.44] C. Kittel, 2005, "Introduction to Solid State Physics", John Wiley & Sons, Inc., United States of America

[1.45] S. R Wenham, M. R Green, M. E Watt and R. Corkish, 2007, "Applied photovoltaics". Earthscan, United Kingdom

[1.46] T. Paxton and L. Thien-Nga. Phys. Rev. B 57 (1998) 1579

[1.47] E. Vulliet, C. Emmelin, J. M Chovelon, et al., Appl. Catal. B 38 (2002) 127

[1.48] A. Fujishima, K. Kobayakawa and K. Honda. J. Eloctrochem. Soc. 122 (1975) 1487

[1.49] X. Pan, M. Q. Yang, X. Fu, N. Zhang and Y. J. Xu, Nanoscale, 5 (2013) 3601

[1.50] L. Nakamura, N. Negishi, S. Kutsuna, T. Ihara, S. Sugihara, K. Takeouchi and J. Mol. Catal A: Chem. 161 (2000) 205

[1.51] G. U. Oertzen and A. R. Gerson. J. Phys. Chem. Solids, 68 (1969) 979

[1.52] R. Memming, 2001, "Semiconductor Electrochemistry", Wiley-VCH, New York

[1.53] L. M. Peter, 2016, "Semiconductor electrochemistry", Springer, United Kingdom

[1.54] X. Pan, M. Q. Yang, X. Fu, N. Zhang and Y. J Xu. Nanoscale 5 (2013) 3601

[1.55] 'Photocatalyis'2017, In Wikipedia: The Free Encyclopaedia, Wikimedia Foundation Inc. [Accessed: 26 October 2017], Available: http://en.wikipedia.org/wiki/Photocatalysis

[1.56] A. Mills and J. Hunte, Photochem., Photobiol., A Chem. 108 (1997) 1

[1.57] M. Plodinec, A Gajovic, G. Jaska, K. Zagar and M. Ceh, J. Alloys Compd. 591 (2014) 147

[1.58] Y. Tang, Z. Jiang, Q. Tay, J. Deng, Y. Lai, D. Gong, Z. Dong and Z. Chen, RSC Adv. 2 (2012) 9406

[1.59] S. U. M. Khan, M. Al-Shahry and W. B. Ingler Jr., Science 297 (2002) 2243

[1.60] Z. Liu, X. Zhang, S. Nishimoto, M. Jin, D. A. Tryk, T. Murakami and A. Fujishima, Phys. Chem. C. 112 (2008) 253

[1.61] P. Roy, D. Kim, K. Lee, E. Spiecker and P. Schmuki, Nanoscale 2 (2010) 45

[1.62] J. Yan and F. Zhou. J. Mater. Chem. 21 (2011) 9406

[1.63] Y. R Smith, R. S Ray, K. Carlson, B. Sarma and M. Misra, Materials 6 (2013) 2892

[1.64] A. Fujishima, D. A. Tryk and K. Honda (ed), Photoelectrochemical Conversion 2 (1999) 196

[1.65] J. Chen, H. Wang, X. Wei and L. Zhu, Mater. Res. Bull. 47 (2012) 3747

[1.66] A. Fujishima, T. N Rao and D. A Tryk, Journal of Photoelectrochemistry and Photobiology C: Photochemistry Reviews 1 (2000) 1

[1.67] M. K Nazeeruddin, E. Baranoff, M and Gratzel, Solar Energy. 85 (2011) 1172

[1.68] W. Y. Rho, H. Jeon, H. S. Kim, W. J. Chung, J. S Suh and B. H. Jun, Journal of Nanomaterials (2015) 247689

[1.69] B. O'Regan and M. Gratzel, Nature 353 (1991) 737

[1.70] P. Roy, D. Kim, I. Paramasivam and P. Schmuki., Electrochem. Commun. 11 (2009) 1001

[1.71] M. Gratzel, Inorg. Chem. 44 (2005) 6841

[1.72] D. Kim, A. Ghicov and P. Schmuki, J. Am. Chem. Soc. 130 (2008) 16454

[1.73] P. Hoyer, Langmuir. 12 (1996) 1411

[1.74] J. H. Lee, I. Leu, M. C. Hsu and Y. W. Chung, J. Phys. Chem. B. 27 (2005) 13056

[1.75] C. C Tsai, H. Teng, Chem. Mat. 16 (2004) 4352

[1.76] M. Byranvand, A. N. Kharat, L. Fotholahi and Z. M Beiranvand, JNS 3 (2013) 1

[1.77] H. Shin, D. K. Jeong, J. Lee, M. M. Sung and J. Kim, Adv. Mater. 16 (2004) 1197

[1.78] C. Bae, H. Yoo, S. Kim, K. Lee, J. Kim and M. M. Sung, Chem. Mat. 20 (2008) 756

[1.79] W. Tan, B. P. Murphy, A. Ahmad, S. A. Akbar, Ceramics International 38 (2012) 4421

[1.80] 'Sol-Gel', 2017. In Wikipedia: The Free Encyclopaedia, Wikimedia Foundation Inc. [Accessed: 14 March 2017], Available at: http://en.wikipedia.org/wiki/sol-gel

[1.81] J. J. Qiu, W. D. Yu, X. D. Gao and X. M. Li, Nanotechnology 17 (2006) 4695

[1.82] M. Zhang, Y. Bando and K. Wada, J. Mater. Sci. Lett. 20 (2001) 167

[1.83] J. H. Kim, X. D. Zhang, J. D. kim, H. M. Park, S. B. Lee and J. W. Jung, Solid state Chem. 196 (2012) 435

[1.84] C. Bae, Y. Yoon, H. Yoo, D. Han, J. Cho, B. H Lee, M. M Sung, Chem Mater. 21 (2009) 2574-2576

[1.85] E. Stoyanov, F. Langenhorst and G. Steinle-Neumann., American Mineralogist, 92 (2007) 577

CHAPTER TWO

Electrochemical Anodisation and Growth of TiO_2 Nanotubes

2.1 Introduction

Vertically aligned TiO_2 NTs are one of the most widely studied one-dimensional nanostructures. The research studies are intensified by the material's remarkable optical and electrical properties that make them of interest in technological and biological applications [2.1-2.4]. Some of the synthesis techniques that are used to synthesise TiO_2 NTs were discussed in chapter one. The successful synthesis of TiO_2 NTs via the electrochemical anodisation of Ti in fluorinated electrolytes by Gong et al [2.4] has resulted in the anodisation technique being the most popular technique employed for the synthesis of TiO_2 NTs. This prolific use is attributed to the fact that the technique permits control over morphology, it is environmentally friendly, cost-effective and straight-forward approach to obtain ordered nanotube arrays [2.1-2.2, 2.5-2.6]. This chapter will discuss the background of the anodisation technique, how it is used to synthesise TiO_2 NTs and the growth mechanism in fluorinated electrolytes. The chapter will conclude with a discussion on the experimental procedures undertaken for this study to synthesise TiO_2 NTs.

2.2 Electrochemical Anodisation: Background

Anodisation is an electrolytic passivation technique commonly used to form and/or thicken the oxide layer that forms on valve metals upon their exposure in the atmosphere [2.2]. The discovery of electrochemical anodisation technique dates to the early nineteenth century through scientific research by Nicholson and Gayle. The two-discovered electrolytic decomposition of water by the electric current supplied by a galvanic battery while they were experimenting on their galvanic cell [2.7]. In 1923, the electrochemical anodisation technique was employed on industrial scale by Bengoughs and Stuart [2.8] to protect the surface of Al and its alloys from corrosion by means of thickening the oxide layer, which is also known as

the barrier layer. Since then, the technique has been widely used to synthesise porous Al_2O_3 in sulphuric electrolytes, compact oxide layers in neutral fluoride free electrolytes [2.9-2.10] and through the work of [2.4] the technique is also used to synthesise TiO_2 NTs.

A typical anodisation setup is shown in figure 2.1 below and consists of an electrode (typically a metal such as Ti, Al, V, etc.) connected to the positive terminal of a direct current (DC) power-supply and a counter electrode (Pt, Ni, etc.) connected to the negative terminal. The two electrodes are immersed in the electrolyte solution as shown in the figure. When a positive voltage is applied, the positive and negative ionic species that are dissociated in the electrolyte are accelerated by the generated electrical field towards the surface of the cathode and anode materials, respectively. In the presence of oxygen (O^-) ions in the solution, the movement of negative ions results in an anodic reaction where the O^- ions react with the metal species, forming an oxide layer. Depending on the applied voltage, electrolyte composition and temperature, the grown oxide layer may either be completely dissolved in the solution, continuously increasing in thickness until saturation point and/or can be converted into a porous structure, which can, subsequently, also be transformed into tubular structures [2.2, 2.5-2.6]

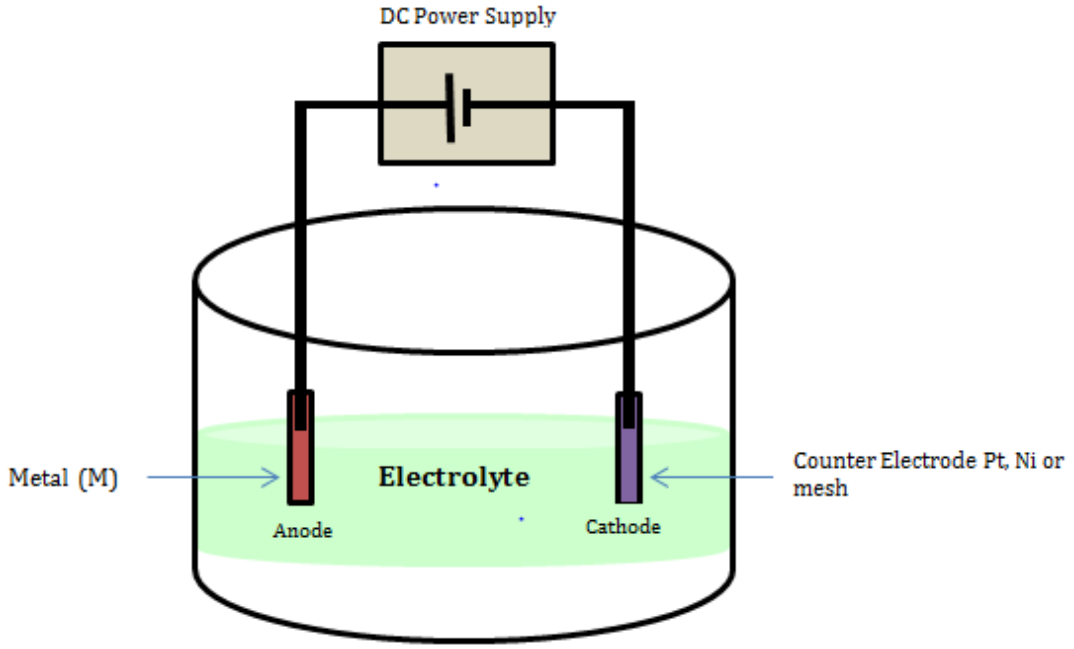

Figure 2.1: Schematic diagram illustrating a typical anodisation setup (redrawn) [2.6]

2.3 Formation of Compact Oxide Layer on Metals

When a sufficient anodic potential is applied on the anodisation setup containing fluoride free electrolyte as in figure 2.1, the formation of the compact oxide layer occurs. The growth of this compact oxide layer involves three reactions, namely the oxidation reaction (2.1), the reduction reactions (2.2) and the overall metal-oxide formation reaction [2.11]

$$M \rightarrow M^{n+} + ne^{-} \quad (2.1)$$

$$2H_2O \rightarrow 4H^{+} + 2O^{-} \quad (2.2)$$

$$M + 2H_2O \rightarrow MO_2 + 4H^{+} + 4e^{-} \quad (2.3)$$

In the oxidation reaction, the metal is oxidized to forming ionic species (M^{n+}), while in the reduction reaction the water molecules are dissociated into their ionic (H^+ and O^-) components. Due to the presence of the field, the oxidized metal species migrates outwards the metal-oxide interface and react with the inward transported O^- ion species at inner or outer oxide interface depending on the field strength. This phenomenon is schematically represented in figure 2.2 (a) and lead to growth of compact oxide layer as per reaction (2.3). [2.13]. Since the system is under a constant applied voltage, the thickness of the compact oxide layer is steadily increased together with its resistivity as depicted in current-time transient curve in figure 2.3 (d). This in turn, result in reduction of field strength inside the oxide, thus reducing the field capability to drive ionic species. As for this result, the outward migration of oxidised metallic ion species and inward transport of O^- species is impeded and the growth rate of oxide layer is decreased until no oxide forming reaction (2.3) occurs. At this stage (III), the current-time curve in fluoride free electrolytes reaches and maintain minimum current values which is indicative of no further formation of the oxide. [2.6, 2.11-2.13].

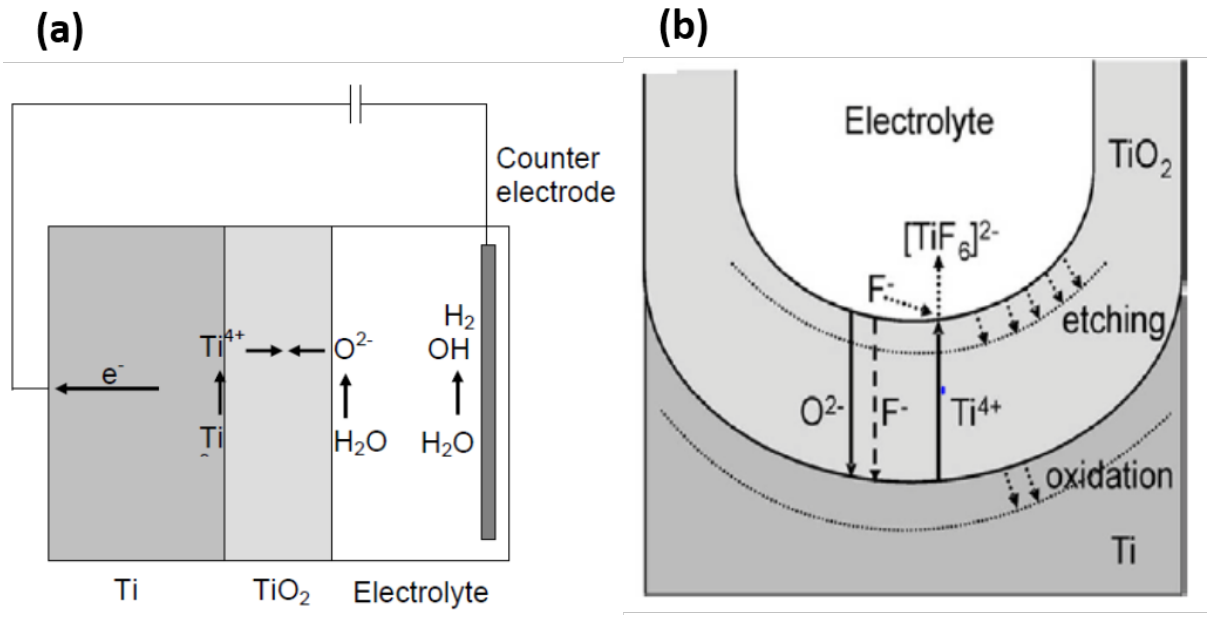

Figure 2.2: Ti anodisation (a) in fluoride free electrolyte to form TiO2 [2.13] and (b) in fluorinated electrolyte forming TiO2 NTs [2.12]

2.4 Growth of TiO_2 Nanotubes in Fluorinated Electrolytes

In the presence of halides such as fluoride (F^-) in the electrolyte solution, the passive state of the compact oxide layer, shown in figure 2.3 (a), is subject to local instabilities [2.14-2.15]. This is attributed to the ability of F^- to form water-soluble complexes as per reaction (2.4) that aid as prevention of the oxide formation at the metal-oxide interface. Furthermore, the small radius of F^- ions enable them to be easily transported through the formed oxide lattice to the metal-oxide interface by the applied field, thereby competing with the O^- ions as shown in figure 2.2 (b) [2.11-2.12]. Consequently, this results in chemical dissolution of the formed oxide layer to form the water-soluble complexes as per reaction (2.5) and prevent the formation of precipitates upon arrival of Ti^{4+} ions at the oxide-electrolyte interface.

$$Ti^{4+} + 6F^- \rightarrow [TiF_6]^{2-} \quad (2.4)$$

$$TiO_2 + 6HF \rightarrow [TiF_2]^{2-} + 2H_2O + 2H^+ \quad (2.5)$$

Moreover, the chemical dissolution of the formed oxide layer, as a result of (2.5), is accompanied by the formation of random pores that are shown in figure 2.3(b). During the pore formation phase, an active area on the oxide layer is increased and thus the resistivity of the

oxide layer is reduced. This leads to an increase in current and thus results in the deviation of current-time curve (stage ii) in fluorinated solutions compared to that observed in fluoride free electrolytes as shown in figure 2.3 (d). As anodisation times elapses, many pores have initiated and start to compete for available current, thereby forming a tree-like shape until a steady state (state iii) between the chemical dissolution and oxide formation is established. At this stage, the rate of pore formation at metal-oxide interface is identical to the oxide dissolution rate at oxide-electrolyte interface and the pores have developed into nanotube structure, shown in figure 2.3 (c), that continuously etch the Ti substrate with no further thickening of the oxide layer [2.11-2.12].

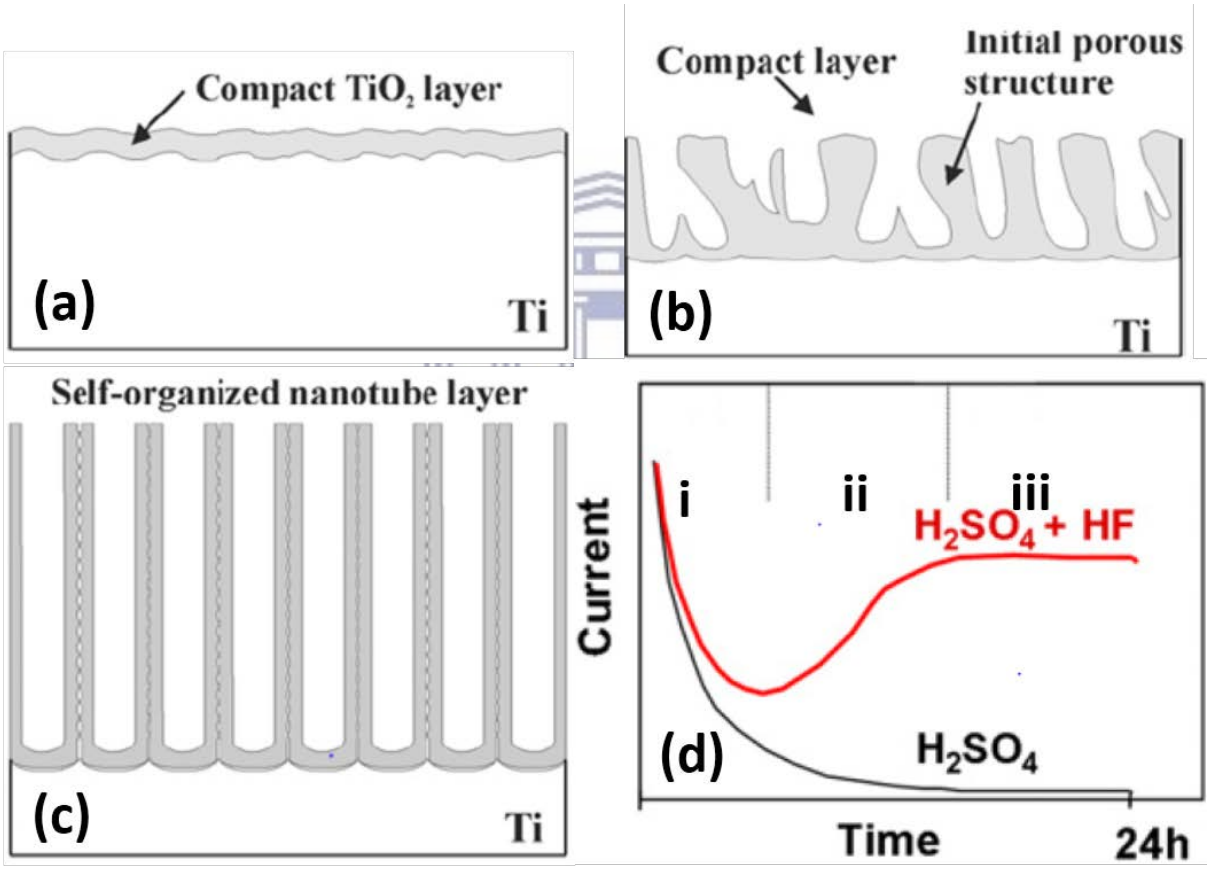

Figure 2.3: (a)-(c) Evolution stages of TiO2 morphologies during anodisation of Ti in fluorinated electrolyte and (d) characteristic current-time curve for Ti anodisation in fluoride free (black line) and fluorinated electrolyte (red-line) [2.12]

During steady state, the length of the nanotube layer increases until the electrochemical etch rate (reaction 2.4) reaches that of the chemical dissolution rate of the top nanotube surface (reaction 2.5). At this point the nanotube length will be independent of the anodisation time, as determined for a given electrolyte concentration and applied potential. As such the chemical dissolution is the key for the self-organised formation of the nanotube arrays, as it not only reduces the thickness of the oxide layer (barrier layer), but also keeps the electrochemical etching (field-assisted oxidation and dissolution) process active; no nanotube structures will be formed if the chemical dissolution is too high or too low. In turn, the electrochemical etch rate depends on the applied anodisation potential and concentration of electrolytes. More accurately though, the anodic potential at which nanotubes are formed is strongly related to the F^- concentration, with higher potentials requiring electrolytes of higher F^- concentration [2.11, 2.12].

2.5 Experimental Procedure

2.5.1 Electrolyte Preparation

In this study, the synthesis of TiO_2 NTs was carried out in three different electrolyte regimes. A total electrolyte solution volume of 200 ml was used for each class of synthesis, with all three electrolyte types fluorinated. The concentration of electrolyte constituents together with the other anodisation parameters are summarised in Table 2.1 below.

Table 2.1: Electrolyte constituents for all three regimes and anodisation parameters

Electrolyte/ Parameters	**Regime 1**	**Regime 2**	**Regime 3**
NaF concentration (M)	0.14	1.0	-

H_3PO_4 concentration (M)	0.5	-	-
H_2O concentration (Volume %)	97	2	2
NH_4F concentration (M)	-	-	0.14
PEG (Volume %)	-	-	98
Glycerol (Volume %)	-	98	-
pH	2.61	7.47	7.67
Voltage (V)	3	60	60
Time duration (h)	3	4	77

In the first electrolyte regime, the solution was prepared by dissolving 0.14 mol/*l* (M) of sodium fluoride (NaF) salt in 97% volume of deionised water (DI H_2O) before the mixture was stirred using hot-plate (BANTE- Instrument, MS 400) magnetic stirrer. The stirring process was operated at room temperature for 5 minutes. During the stirring process, 0.5 M of phosphoric acid (H_3PO_4) was added to the solution to achieve the desired total electrolyte solution volume.

The preparation of the second electrolyte regime was carried out by dissolving 1.0 M of NaF in 2% volume of DI H_2O before adding 98 vol% of glycerol. The solution was rigorously stirred with the hot-plate magnetic stirrer operated at an elevated temperature of 60°C for 20 minutes to reduce the solution viscosity. The solution was then cooled in air to room temperature and the pH meter (HANNA-Instruments, HI 2210) was used to measure the pH of the solution prior to its used for anodisation.

Lastly, the third electrolyte regime was prepared by dissolving 0.14 mol/*l* (M) of Ammonium fluoride-NH_4F in 2 vol% DI H_2O before adding 98% volume of polyethylene glycol (PEG-400). The solution was then stirred using hot-plate magnetic stirrer and the pH meter was used to measure the pH of the solution. All chemicals that were used for this study were chemical grade and were purchased from Merck chemicals (Pty) Ltd. Gauteng, South Africa.

2.5.2 Sample Preparation and Synthesis

Twenty-five micrometre (25 µm) thick Ti foil sheets were cut into 1 x 1.5 cm^2 rectangular substrates that were subsequently rinsed in anhydrous ethanol (99.9 % purity) over night. Prior to their use for synthesis, the substrates were rinsed in H_2O (DI) for 2 minutes before being dried using compressed air and treated under hot filament lamp for 5 minutes. For the synthesis in all three electrolyte regimes, the substrates were clipped using crocodile clips that were connected to the positive terminal of DC power supply and immersed into the electrolyte solution along with flag shaped 1 x 1.5 cm^2 Pt grid that was used at cathode material. The distance between the two electrodes was maintained between 1 and 2 cm.

Soon after the two electrodes were immersed into the electrolyte and properly spaced, the voltage was ramped at ramping rate of 1 V/s to the desired voltage for all three electrolyte regimes synthesis. During anodisation, a Simple Data Logger ® II (Model L322) interfaced with computer system was used to measure current density fluctuations at the anode (Ti). After the anodisation duration elapsed, the samples were rinsed in DI H_2O and dried in the same manner as before the anodisation. The experimental setup used in this study for the synthesis of one-dimensional TiO_2 NTs is depicted in figure 2.4 together with its schematic representation.

The as-synthesised TiO_2 NTs samples were then annealed in air for 3 hours using Brother XD 1600MT 3-zone furnace operated at 450°C and 600°C. During the annealing process, the furnace was ramped at 10°C/min to the desired temperature and dwelled there for 3 hours before being cooled back to room temperature.

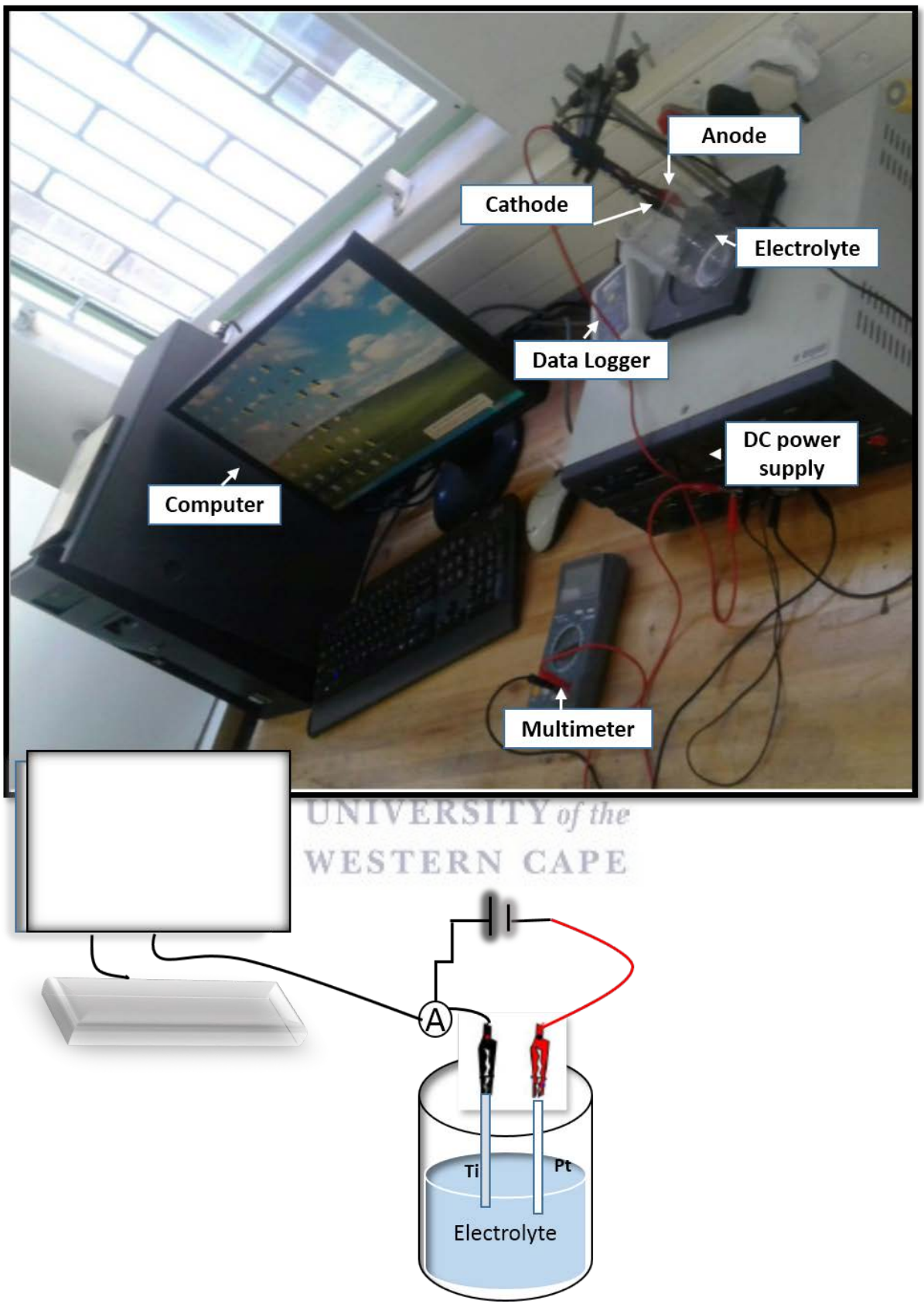

Figure 2.4: Experimental setup used in this study to synthesise TiO2 NTs

References

[2.1] A. Ghichov and P Schmuki., Chem. Commun. 10 (2009) 2791

[2.2] A. C. Grimes and G. K. Mor, 2009," TiO2 Nanotube Arrays- Synthesis, Properties and Applications", Springer Science + Business Media, New York

[2.3] T. Shokuhfar, 2010, "Structural and surface property characterization of titanium dioxide nanotubes for orthopedic implants", Unpublished PhD Thesis, Michigan Technological University, United States of America

[2.4] D. Gong, C. A. Grimes, O. K. Varghese, W. Hu, R. S. Singh, Z. Chen, E. C. Dicke, J Mater Res. 16 (2001) 3331

[2.5] S. Sobieszczyk and R. Klotzke, Advances in Material Science 11 (2011) 1-27

[2.6] J. M. Macak, H. Tsuchiya, L. Taveira, S. Aldabergerova, and P. Schmuki, Angew. Chem. Int. Ed. 44 (2005) 7463.

[2.7] C. Vargel, M. Jacques and M. P. Schmidt, 2004, "Corrosion of Aluminium", Elsevier Publishers, The Netherlands.

[2.8] G. D. Bengoughs and J. M. Stuart, Brit. Patent. (1923) 223

[2.9] V. P. Parkhutik, V. T. Belov and M. A. Chernyckh, Electrochem. Acta. 35 (1990) 961

[2.10] H. Masuda and K. Fukuda, Science 268 (1995) 1466

[2.11] A. Ghichov and P Schmuki, Chem. Commun. 10 (2009) 2791

[2.12] J.M. Macak, H. Tsuchiya, A. Ghicov, K. Yasuda, R. Hahn, S. Bauer and P. Schmuki, Curr. Opinion Solid State Mater. Science 11 (2007) 3

[2.13] JM Macak., 2008, "Growth of Self-Organised Titanium dioxide nanotube Layers" Unpublished PhD thesis, University of Erlangen. Germany

[2.14] J.L. Delplancke, R. Winard, Electrochim. Acta 33 (1988) 1539

[2.15] J. Yahalom and J. Zahavi, Electrochim. Acta 15 (1970) 1429.

CHAPTER THREE

Characterisation Techniques

3.1 Introduction

After synthesis and post-annealing of the TiO_2 nanotubes, electron microscopy and x-ray diffraction were used to characterise both the as-deposited and annealed samples. The scanning electron microscope (SEM) was used to study structural features such as length, pore-diameter, and surface topography of the samples while energy-dispersive x-ray spectroscopy (EDS) was used to study elemental concentration. The crystal structure of TiO_2 nanotubes was studied using a transmission electron microscope (TEM), operated in diffraction mode which was confirmed by x-ray diffraction (XRD) studies, performed on the bulk TiO_2 nanotube substrates. Electron energy loss spectroscopy (EELS), operated in parallel and serial mode, in combination with scanning transmission electron microscope (STEM-EELS) allowed for the study of the fine structure of the nanotubes and the phase transformation along tube length.

This chapter will focus on the physics principles behind the instruments used for characterisation and describe their basic operating principles. More emphasis will be placed on electron microscopy, which forms the main analysis technique for this study. As such, each component of the two instruments (SEM and TEM) together with the underlying physics will be discussed extensively in the sections that follow.

3.2 Electron Microscopy

3.2.1 Introduction

The optical components of an electron microscope can be divided into three sectors according to their functionality. Firstly, the instrument consists of an illumination system commonly known as an electron gun that is situated at the top of the instrument. An electron gun is responsible for the generation of a large number of electrons sometimes called electron cloud which are fed into the instrument column by means of an applied biased voltage. Secondly, the instrument consists of a region of electromagnetic lenses commonly known as the instrument column. In this region, the electromagnetic lenses focus and concentrate the cloud of electrons fed into the column, thereby producing an electron beam. Lastly, in the case of a TEM, the instrument has an image formation section. In this section, a very thin specimen mounted on the specimen chamber situated on the column is bombarded with the electron beam resulting in beam-specimen interaction. The transmitted electrons are thereby processed by series of electromagnetic lenses situated below the specimen to produce first intermediate images that is enlarged and displayed on the viewing screen. However, in the case of the SEM, a series of objective lens apertures are used for aberration corrections induced during the beam formation before the bombardment of the specimen. The image is then formed digitally after processing signals that were produced during beam-specimen interactions. [3.1, 3.2].

3.2.2 Components of the Electron Microscope: The Electron Gun

There are two types on electron guns that can be utilised for electron beam generation, namely: (i) the triode or thermionic gun and (ii) the field-emission gun (FEG). These guns differ in the way onto which electrons are formed and the resulting beam properties which include beam diameter (spot-size) and beam intensity, thus they affect the instruments resolution.

a) Thermionic (Triode) Gun

A triode gun employs an equivalent principle to that of electrostatic lenses where the focusing of the electron cloud is attributed to the presence of electric fields [3.2]. A triode gun consists of an electron source, a high voltage power supply and the anode plate as shown in figure 3.1. The electron source can either be a tungsten (W) filament or lanthanum hexaboride (LaB_6)

crystal that is connected to the negative terminal of a high voltage power supply. The Wehnelt cap around the source is held at a slightly higher negative potential than the filament (>2500V), whereas an anode plate connected to the positive terminal is held at a grounding potential. The resulting potential difference between the anode plate and the gun varies at approximately 1 kV to 50 kV for SEM depending on the required beam intensity [3.1]. This potential is known as the accelerating voltage. Primarily, the purpose of accelerating voltage is to rapidly accelerate the thermionically liberated electrons situated between the filament (or crystal) tip and Wehnelt cap towards the anode plate. However, as electrons emanate from the Wehnelt opening, they are electrostatically repelled by the Wehnelt walls, which are at higher negative potential than the filament. This electron repulsion result in a crossover (d_0) region in space just above the anode plate as shown in figure 3.1. The diameter of the crossover point also known as spot-size is largely dependent of the sharpness of the filament tip used and is very crucial in determining the brightness of the gun and instrument resolution [3.2, 3.3].

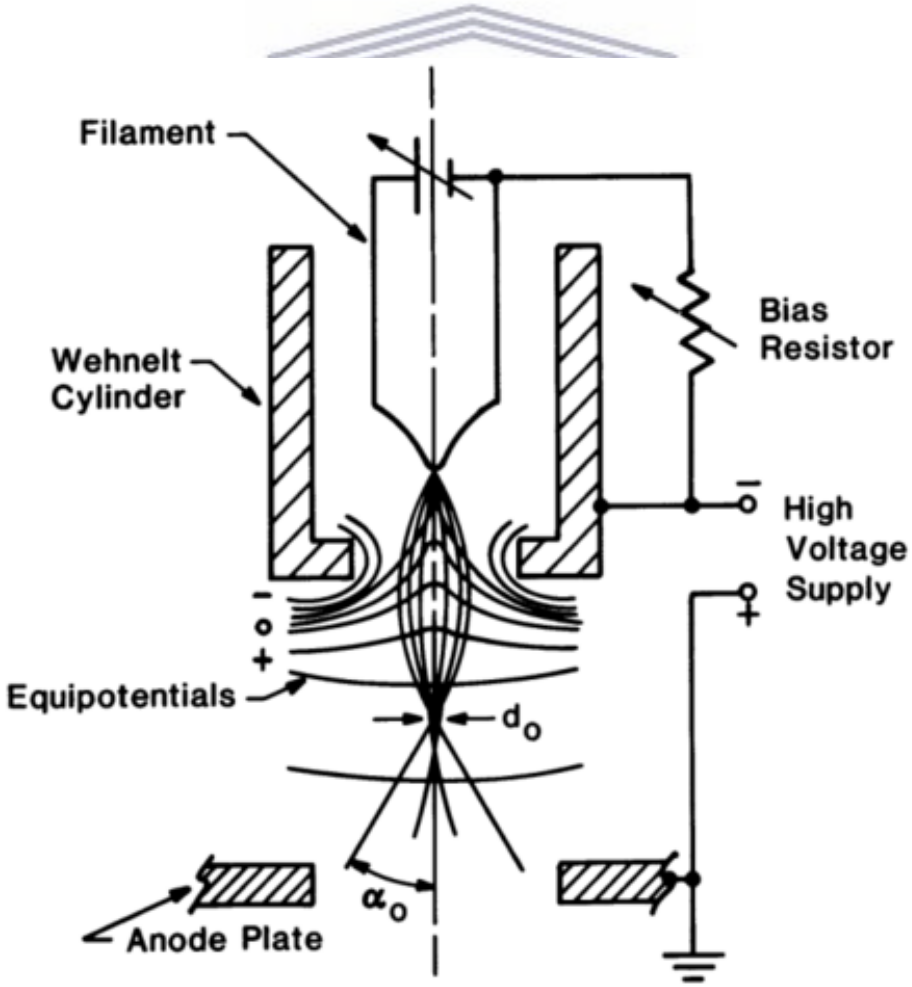

Figure 3.1: Tungsten Filament Source versus Lanthanum Hexaboride (LaB_6) Crystal [3.3]

As previously mentioned, the triode gun can either use a W-filament or LaB_6 crystal as electron source. These two have different work functions, hence require different thermal treatment to overcome their individual work functions and are operated in different vacuum chambers. The use of hairpin-shaped W-filaments with tip radius of 100 µm requires an operating temperature of about 2700K to overcome the filament's work function, which is approximately 4.2 eV. At increasing operation temperatures, the number of electrons produced by the tungsten filament is also increased and thus, in a good vacuum, this ultimately enhances the brightness of the gun. However, the increase in operating temperature consequently results in rapid evaporation of W, thereby reducing the lifetime of the filament. The development of new characterization techniques that requires higher brightness than that offered by the tungsten filament resulted in the use of the LaB_6 crystal as the electron source.

LaB_6 is a compound formed by the presence foreign lanthanum atoms in the crystal lattice of boron. This compound has a very low work function of approximately 2.7 eV. This means, to obtain the same brightness produced by tungsten filament, LaB_6 with tip radius of 5µm would only require a temperature which is half of that required by W-filament, hence when operated at same temperature; LaB_6 would produce a brighter electron beam. Due to this improvement in the beam brightness when LaB_6 crystal is used, it has been regarded as the best cathode material compared to W-filament for two main reasons. Firstly, for having longer lifetime due to low evaporation and secondly, for the higher brightness achieved when operated at the same temperatures. However, LaB_6 is highly reactive with most elements when heated, except carbon and rhenium. Thus, its use in the instrument would require ultra-high vacuum compared to that required when W-filament is used. Furthermore, when using LaB_6, shielding around the electron gun is crucial as it prevents the evaporated lanthanum from attaching to the surrounding surfaces and helps in maintaining good vacuum, as shown in figure 3.2 [3.3, 3.4].

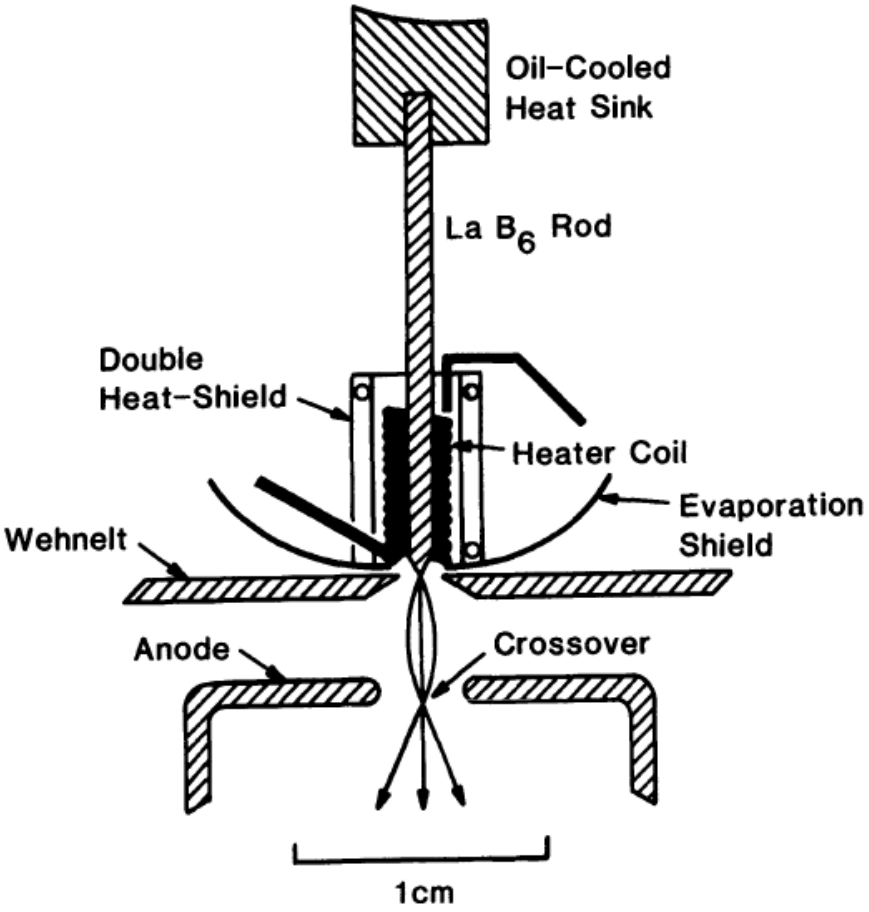

Figure 3.2: Electron gun with shielded LaB6 cathode [3.3]

b) Field Emission Gun

Field-emission guns operate on a different principle to triode guns since they do not require thermal treatment to overcome the cathode work function, as necessary for triode gun cathodes. This is advantageous for the microscope society since it eliminates cathode evaporation, thus increasing its life span while enhancing brightness. FEGs use cathode in the form of a rod with a sharp tip diameter of 100 nm (0.1 μm) which is usually made from single crystalline tungsten, as shown in figure 3.3 below. The production of electrons in this type of gun is achieved by applying an electric field of less than 10^9 V/m to the cathode material, causing the reduction in height of the potential barrier while in turn increasing the probability of electrons to tunnel through without any additional energy used. The tunnelled electrons with energy spread of less than 0.5 eV, which is much smaller than that of triode guns, are extracted from the tip through the opening of the first anode, which is held at an extraction potential voltage of few kilovolts.

A second anode, held at higher accelerating voltage than the first anode accelerates the electrons into the instrument's column [3.2].

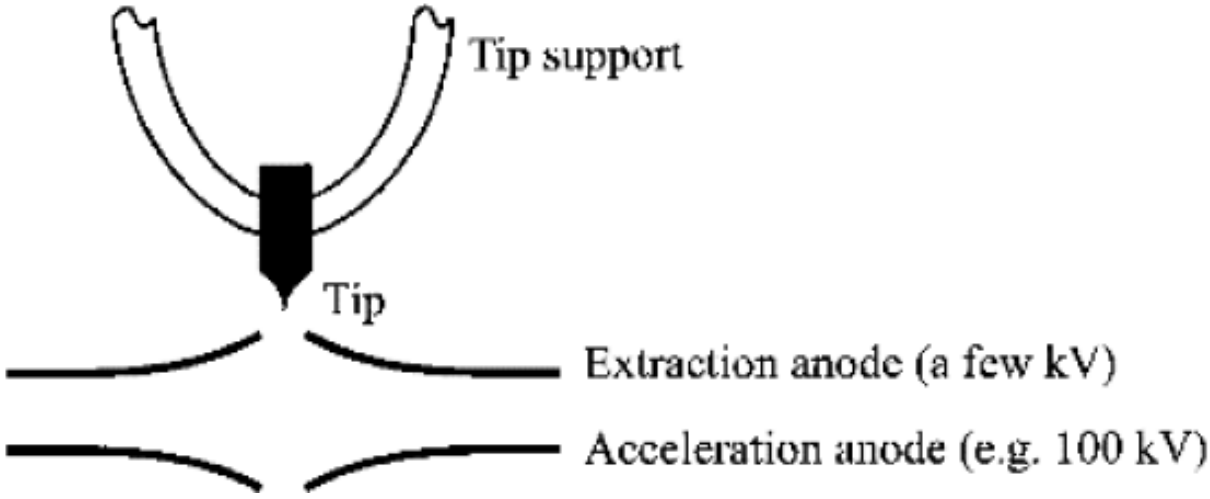

Figure 3.3: Schematic assembly of field-emission gun with two anodes [3.2]

Similar to triode guns, a crossover point in space also exists in FEGs with a beam diameter (spot-size) of about 10 nm, which is much smaller than that of triode guns, thus eliminating the necessity of using de-magnifying lenses. However, the use of FEG requires a very high vacuum, in order of 10^{-9} Pa (or better) since a low work function is obtained on clean cathode surfaces while any surface contamination by foreign atoms would drastically increase the work function, thereby lowering the emission [3.2-3.5].

3.2.3 Electromagnetic Lens: Effect of Inhomogeneous Fields on Electrons

An electromagnetic lens consists of a coiled wire that is surrounded by ferromagnetic pole pieces which are made up of iron. When a current is passed through the coiled wire, a magnetic field is induced around the wire and between the pole pieces with its field strength proportional to the number of coils (or loops) and the current that flows through the wire. When charged particles such as electrons encounter a region of uniform magnetic field, their incident paths will be affected by the presence of a magnetic force which is exerted perpendicular to both the velocity of the incident electron and the direction of the magnetic field. According to electromagnetic theory, the direction of the force is established by performing the cross

product; shown in equation (3.1) of the velocity $\vec{v}$ and the magnetic field $\vec{B}$ vectors while the magnitude can be calculated using equation (3.2),

$$\vec{F} = e(\vec{v} \times \vec{B}) \tag{3.1}$$

$$F = e\,|\vec{v}|\left|\vec{B}\right|\sin(\alpha) \tag{3.2}$$

where $e = 1.602 \times 10^{-19}\ C$ represent the electron charge, $|\vec{v}|$ and $\left|\vec{B}\right|$ the magnitude of the electron velocity and magnetic field respectively, while α represents the angle between the velocity and the magnetic field [3.6]. If an electron encounters the magnetic field at an acute angle, it possesses both the vertical and the horizontal components of the velocity with one of the components being parallel to the magnetic field. Due to the homogeneity of the field, the parallel component is unaffected by the magnetic force and will continue on the same path as was incident with unchanged magnitude of the velocity, whereas the perpendicular component will be forced to follow a circular path depending on the strength of the magnetic field as shown in figure 3.4 [3.2-3.7]

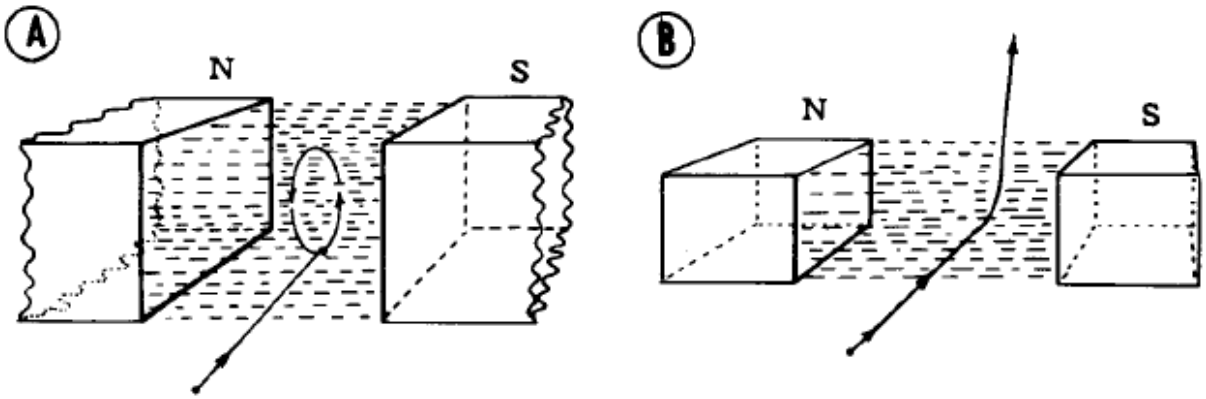

Figure 3.4: Schematic diagram showing the effect of (A) strong magnetic field and (B) weak magnetic field on electron entering these regions [3.7].

In the electron microscope, the above-mentioned scenario is much more complex due to the presence of rotationally symmetric and inhomogeneous (varying) magnetic fields which arise from the coil and the surrounding ferromagnetic material. The magnetic field distribution is then decomposed into two predominant components namely the radial (along the radius) and

axial (along optical axis) components. These components are perpendicular to one another as shown in figure 3.5 and their primary purpose is to focus the diverging electrons emanating the electron gun to a point on the optical axis.

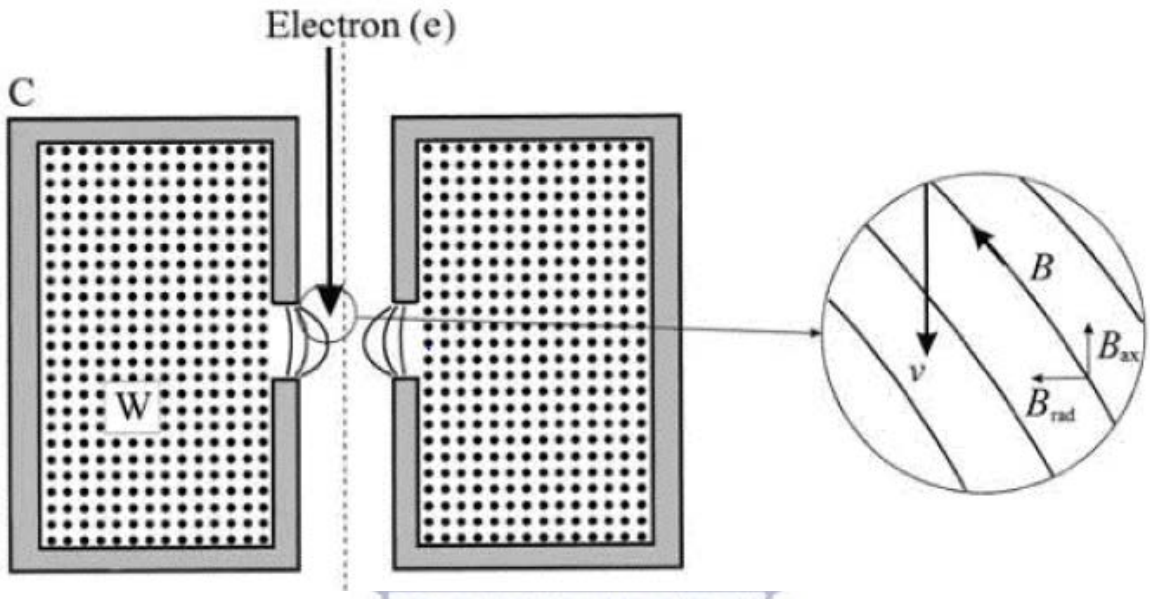

Figure 3.5: Schematic illustrating the effect of magnetic field components on an electron path [3.2]

When the diverging electrons enters the magnetic field region at acute angles, their velocities are decomposed into two components namely; the axial (v_{ax}) and the radial (v_{rad}) that are parallel to the radial (B_{ax}) and axial (B_{rad}) components of the magnetic field respectively. Electrons in axial direction initially experienced a force due the radial component (B_{rad}) of the magnetic field, which causes the electrons to travel in helix along the lens. Towards the centre of the magnetic field region, the radial component decreases while the axial component is increases. This result in increase of azimuthal (along circumference of helix) velocity v_{circum} which is perpendicular to the plane of this page and therefore it experiences a force due to the axial component B_{ax} of the magnetic field. Consequently, this causes the electrons to spiral towards the optical axis until they cross at some point. The point at which the electrons cross is called the focal point and it can be varied by the applied current and the magnetic field strength. Shorter focal points are achieved increasing current passed through the coiled wire and by concentrating the magnetic field by means of magnetic pole-piece [3.2-3.4, 3.6-3.8].

3.2.4 Deflector Coils: Deflection of Electrons by Electromagnetic Fields

Deflector coils are defined as two coiled wires that are connected in series and placed on both side of microscope optical axis just below the electromagnetic lenses as shown in figure 3.6. Similar to the operation of electromagnetic lenses discussed in section 3.2.3, a magnetic field is induced when a current is passed through the coils. However, in the case of deflector coils, the source of current is the sawtooth wave generator which provides the scanning current on deflector coils on both sides of the optical axis.

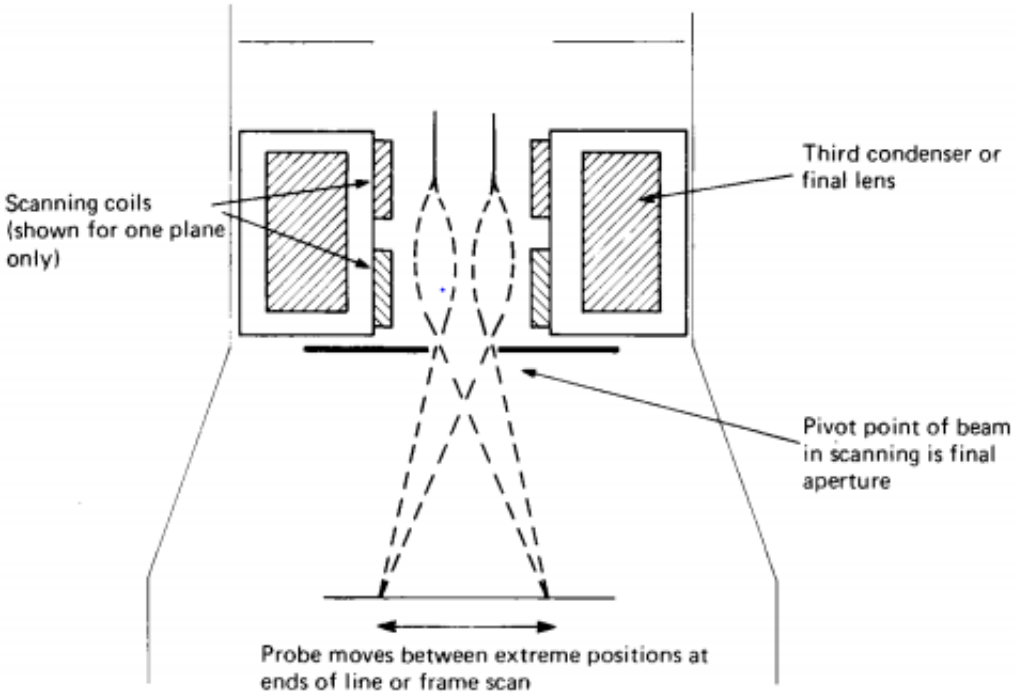

Figure 3. 6: Principle of double deflection system providing a scanning electron beam [3.9].

When a beam of electrons passes through the final lens aperture it encounters a region of weak magnetic field generated by the two deflector coils. The magnetic field strength in the region is sufficient to deflect the electron beam to the direction that is perpendicular to both the direction of the magnetic field and the electron path. The operating principle of electron deflection by deflector coils employs the same physics as the path change of electrons in an homogeneous magnetic field; as described in section 3.2.3 and illustrated by figure 3.4 (A) and (B). Having deflector coils on both sides of the optical axis results in back and forth deflection of the electron beam which allows scanning over the whole surface area of the subject specimen [3.1-3.2, 3.6, 3.9].

3.2.5 Apertures: Effect of the Use of Apertures on the Electron Beam

The electron beam produced by the first EM lens acquires a very high intensity, larger diameter and supplies a very good signal to noise ratio. However, such intensity and diameter result in severe specimen damage and overall loss of image quality, respectively. The use of an aperture, which is a variable circular opening on a disk, allows the manipulation of the intensity and the diameter of the beam by restricting the number of electrons passing through the opening. In optical microscopes where the focal lengths are short, aperture angles are so large that the instruments resolution is limited. The relationship between the aperture angle, which is the angle between the rays and the perpendicular line drawn from the specimen to the centre of the circular aperture, and the resolution, was established by the German Optician named Ernest Abbe with the mathematical equation (3.3) [3.2, 3.9]

$$r = \frac{0.61\,\lambda}{\mu \sin(\alpha)} \tag{3.3}$$

where μ represents the refractive index, α the aperture angle and λ the wavelength of the illumination source. To reduce the aperture angles, the aperture opening must be reduced, hence the resolution is enhanced, from equation 3.3. However, rays passing through the aperture suffer from the diffraction effect, which gives rise to cone shaped rays (rings when viewed in 2D) with the centre of the ring comprising most of the intensity. These rings, also known as airy disks, are inversely proportional to the aperture angle and are partially eliminated by increasing the aperture angle. This, consequently, deteriorates the resolution as portrayed by the Abbe's equation in 3.3. Another important aspect in microscopy that is affected by varying the aperture angle is the depth of field, which can be calculated from [3.2]

$$h = \frac{0.61\,\lambda}{\mu \sin(\alpha) tan(\alpha)} \tag{3.4}$$

where *h* is the depth of field and defined as the range of positions where the sharpness of the image is unchanged when viewed with human eye. In contrast to the optical microscope, the use of electrons in electron microscope improves both the depth of field and resolution of the instrument owing to the electron's shorter wavelength which enables the use of small aperture angles. Figure 3.7 below shows that short working distances result in reduced depth of field, while longer distances enhance the depth of field [3.2, 3.3].

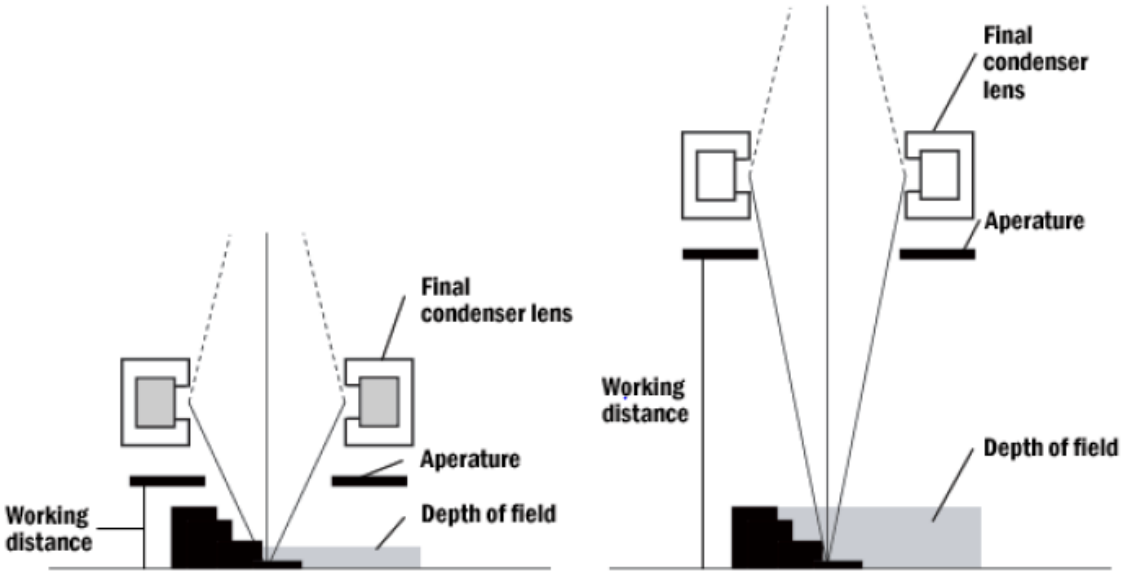

Figure 3.7: Effect of varying the working distance on the depth of field [3.1].

Although the depth of field and resolution are enhanced in the electron microscope, there exists a concern of lens aberrations. These aberrations affect both the multiple and single wavelength(s) sources as a result of the spread of energies in a chromatic source and the variation in ray path lengths in the case of a monochromatic source. The elimination of such aberrations in an optical microscope is achieved by use of compound lenses with different focal lengths and/or aspherical lenses with zero spherical aberration coefficients. However, in an electron microscope, chromatic aberrations are eliminated by the use of FEGs due to their reduced energy spread of less than 0.5 eV compared to the few eV provided by thermionic guns. Whereas spherical aberrations are nearly impossible to eliminate, they can be reduced by use of small apertures that allow only those electrons near the optical axis to enter the instrument's column, without a consequent loss of resolution [3.1-3.3, 3.5-3.9].

3.3 The Scanning Electron Microscope

The SEM is a characterisation tool used to study the surface or near surface structures of bulk samples. This technique is widely utilised in many research fields where the study of smaller materials, typically at micrometre scale, requires imaging at high magnification. The use of electrons as illumination source in SEM allows for imaging at relatively high magnifications at spatial resolution typically between 1 and 10 nm. The high quality three-dimensional images obtained from SEM can be used to deduce very useful information about the specimen surface morphology and topography at nanometer scale. In modern SEMs, the incorporation of high-efficient spectrometers allows high spatial resolution chemical analysis by means of energy or wavelength dispersive x-ray spectroscopy (EDS/WDS) [3.2, 3.5].

3.3.1 Operating Principle of the Scanning Electron Microscope

The operation of the SEM commences with the illumination with electrons, generated by either a triode or FEG, situated at the top of the instrument's column, as shown in figure 3.8 below. The gun generates a cloud of electrons that are accelerated into the column of the microscope by a biased voltage, typically between 1 and 30 kV. Below the gun crossover, the diverging electrons enter the column and are converged by the first electromagnetic lens, known as the condenser lens.

As evident in figure 3.8, the condenser lens system comprises of two lenses namely condenser lens 1 (C1) and condenser lens 2 (C2), with C2 located half way between the specimen and the gun, while C1 is halfway between the gun and C2. The operation of these two lenses at different magnetic field strengths, with C1 operated at a field while C2 is held at a weaker magnetic field, allows the demagnification of the electron closer to the optical axis and the reduction of beam diameter by C1, while C2 controls the illumination angle by focusing the beam at larger focal length than C1. However, below this focal point, divergence still occurs and is counteracted by the magnetic field produced by the current-carrying coiled wires known as scan coils, placed on both sides of the optical axis. The final lens, called the objective lens and its corresponding objective aperture placed just above the specimen chamber, are responsible for further demagnification and focusing of the aligned electron beam, produced by the condenser aperture and the scan coils, into to a small area on the specimen. The objective aperture is used to reduce the intensity of the electron beam and to further reduce the final beam

diameter or spot-size. Thus, this determines the instrument's brightness and spatial resolution [3.2]

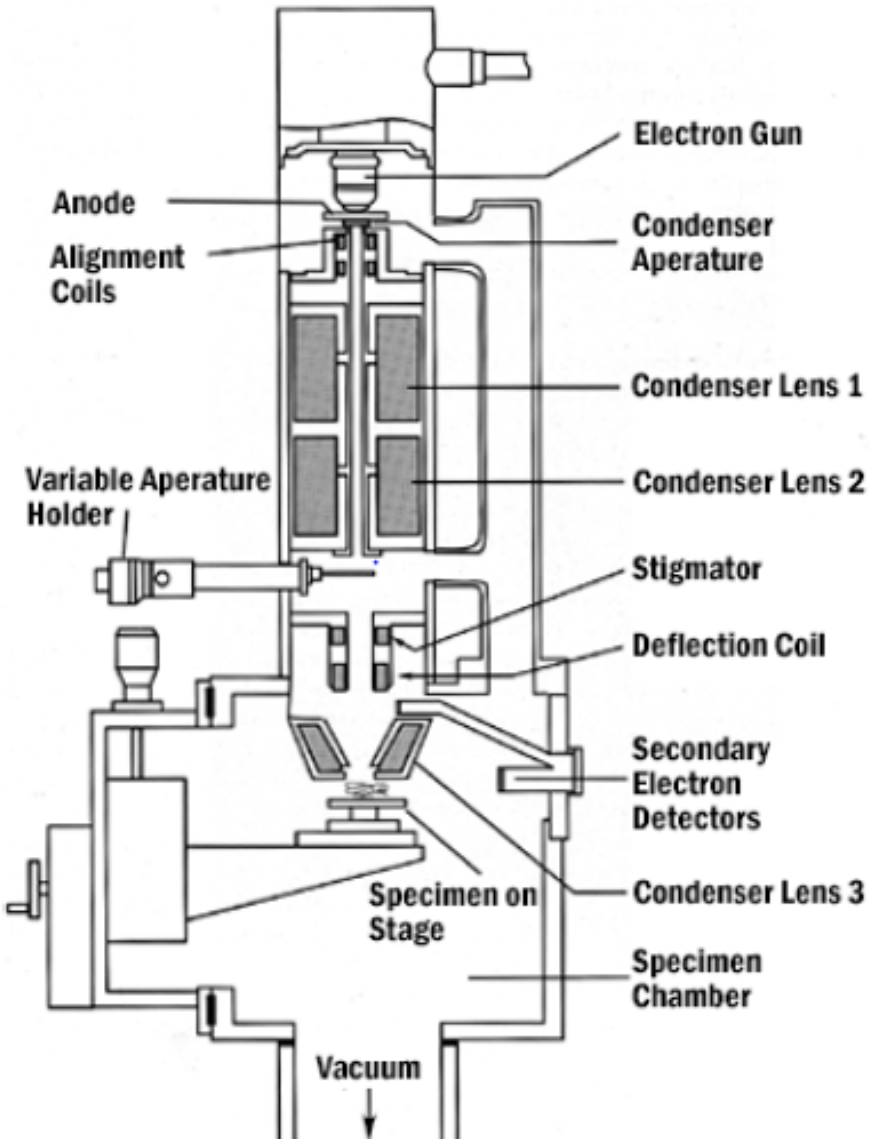

Figure 3.8: The schematic representation of the positioning of SEM components [3.9]

3.3.2 Beam-Specimen Interaction - Signal Generation

Incident electrons, used to bombard the specimen, encounter both elastic and inelastic scattering by the atoms in the specimen. Elastically scattered electrons, by surface atoms of the specimen, are said to maintain their incident kinetic energy since they lose undetectable amount of energy while their trajectory is changed. The signals produced during this type of

interaction are known as backscattered electrons. Another contribution to the backscattered signal arises in the form of low-energy backscattered electrons, which are produced by interactions of the incident electrons with the inner atoms of the specimen. Because of a large number of collisions encountered by these inner backscattered electrons, they emanate from the surface of the specimen with little energy, due to the energy transfer to the surrounding atoms, thereby generating secondary electrons which in turn are easily absorbed by specimen atoms.

In the case of inelastically scattered electrons, the incident electron loses most of its energy in the form of heat, while a small portion is transferred to the atoms of the specimen, giving rise to signals such as x-rays, Auger electrons, cathodoluminescence and secondary electrons. However, there are also some incident electrons that pass through the specimen and are known as transmitted electrons; they carry information about the specimen. Such signals are used in transmission electron microscopy (discussed in later sections). Figure 3.9 below illustrates the signals produced during beam-specimen interaction with signals such as secondary electrons and backscattered electrons of importance in the SEM, as they provide information about the morphology and topography of the sample, whereas the Auger electrons, x-rays and cathodoluminescence provide information about the chemical composition of the specimen [3.1-3.2].

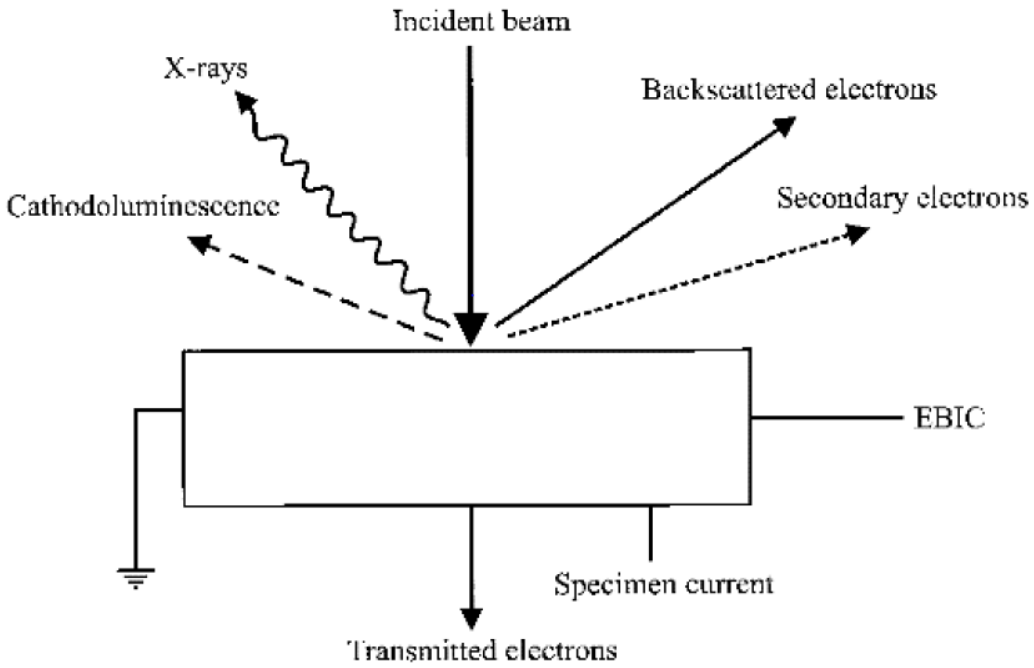

Figure 3.9: Signals produced during Beam-Specimen Interaction [3.9]

The region into which the primary electrons enters and interact with specimen atoms is known as the *interaction volume* and is shown in figure 3.10. In this interaction volume, signals are generated at different depths with those generated near the surface such as backscattered electrons and secondary electrons of great importance in image formation as they provide information at good spatial resolution. Illustrated in figure 3.10 are the three most important SEM signals, used for imaging and chemical analyses, and the different depths in the interaction volume from which they are generated [3.1-3.2].

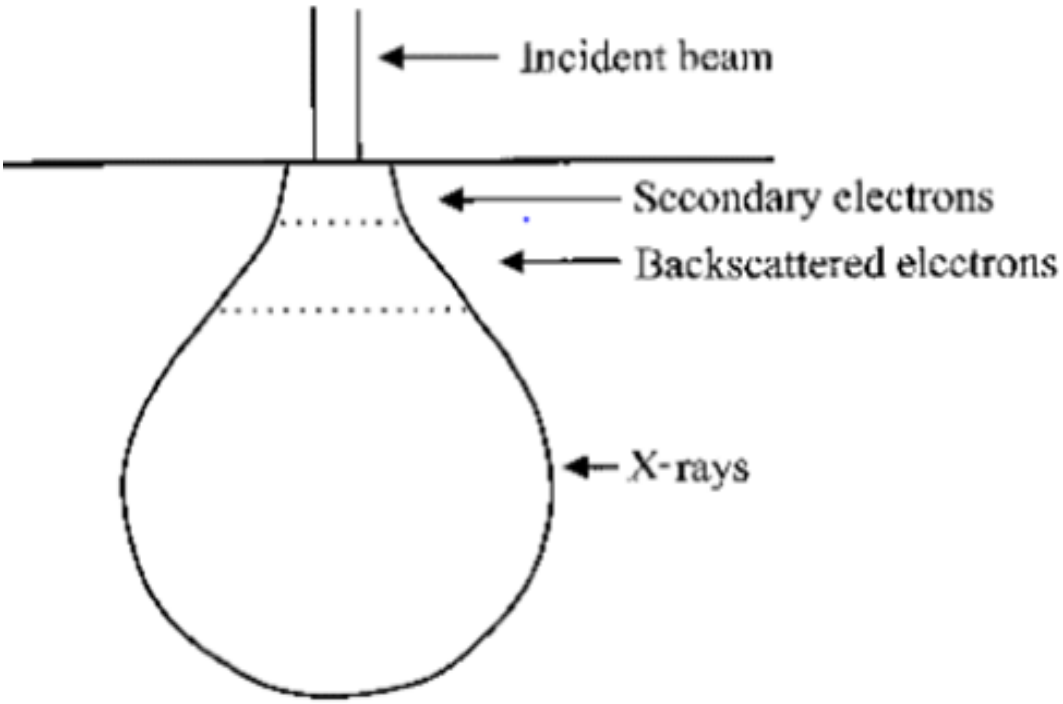

Figure 3.10: Depth profiles for signals produced in the interaction volume [3.2].

3.3.3 Signal Detection for Image Formation in the SEM

As previously mentioned, secondary electrons and backscattered electrons provide information about the specimen with good spatial resolution. Of the two, secondary electrons are the more commonly used signal in the SEM since they have a smaller sampling volume than the backscattered electrons, hence providing better spatial resolution. The detection of secondary electrons is accomplished by used of a scintillator-photomultiplier detector known as an Everhart-Thornley detector (ETD). This detector consists of (a) collector which is held at positive bias responsible for collecting secondary electrons from all directions towards the

surface of a (b) scintillator that contains phosphor which produces light when electrons fall on it, and is covered with a thin aluminium film held at a potential of a few kV to give electrons excess energy to excite the phosphor, and finally (c) a photomultiplier which amplifies the generated signal into measurable electronic pulses, which are then used to modulate a cathode ray tube with the brightness proportional to the collected secondary electrons [3.1-3.2]. Figure 3.11 shows a simplified schematic of a typical ETD system [3.2].

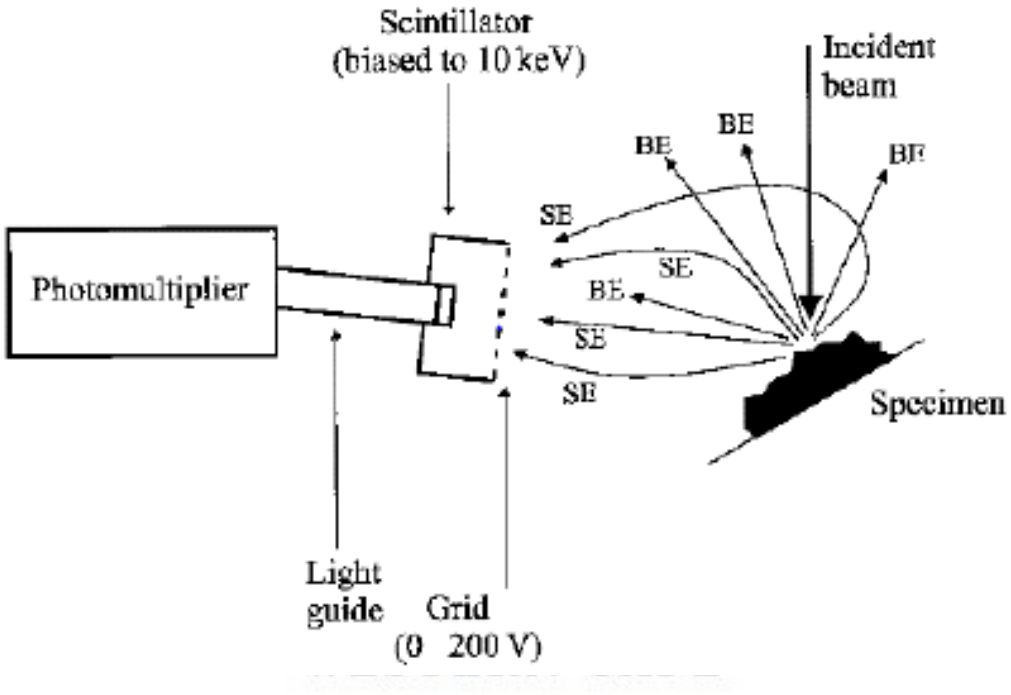

Figure 3.11: Schematic representation of the components of Everhart-Thornley detector [3.2]

Evident from the figure above, backscattered electrons travelling towards the ETD are also detected, thus the image is formed with contribution of backscattered electrons. However, a large portion of backscattered electrons are not detected due to their scattered directions, as shown in figure 3.11. Thus, a scintillation detector known as a *Robinson detector*, with large cross-sectional area, is placed near the specimen for efficient collection of a large number of backscattered electrons. For high resolution SEM, a special type of scintillation detector is placed within the strong magnetic field of the objective lens, whose spherical aberration coefficient is reduced. This detection system is known as the *in-lens detector* and it allows

operation at very short working distances (distance from specimen to objective pole piece) owing to the efficient collection ability of both secondary and backscattered electrons [3.1-3.2, 3.6-3.9]

3.3.4 Characteristic X-ray Detection and Energy Dispersive Spectroscopy

X-ray signals are formed in greater depths of the interaction volume as a result of excitation of atoms innermost electrons upon gaining sufficient energy from the incident primary electrons. Consider the schematic diagram of energy levels of atoms around the nucleus also known as electron shells labelled K, L, M, as shown in figure 3.12. The interaction of the specimen atoms with highly energetic primary electrons results in increased probability of the innermost electrons, typically in the K-shell, to be dislodged into higher energy states leaving behind a vacancy in the K-shell. Electrons in higher energy state are termed to be in an *excited state*. Electrons in neighbouring shells can jump and fill the vacancy left by the excited electron, thereby emitting a photon of characteristic short wavelength known as x-rays. For example, when an electron from L-shell fills the vacancy in the K-shell, the type of radiation formed would be the K_α radiation, while a transition from M to K forms the K_β radiation. Similar nomenclature is applied when an electron in the outer shells has been dislodged.

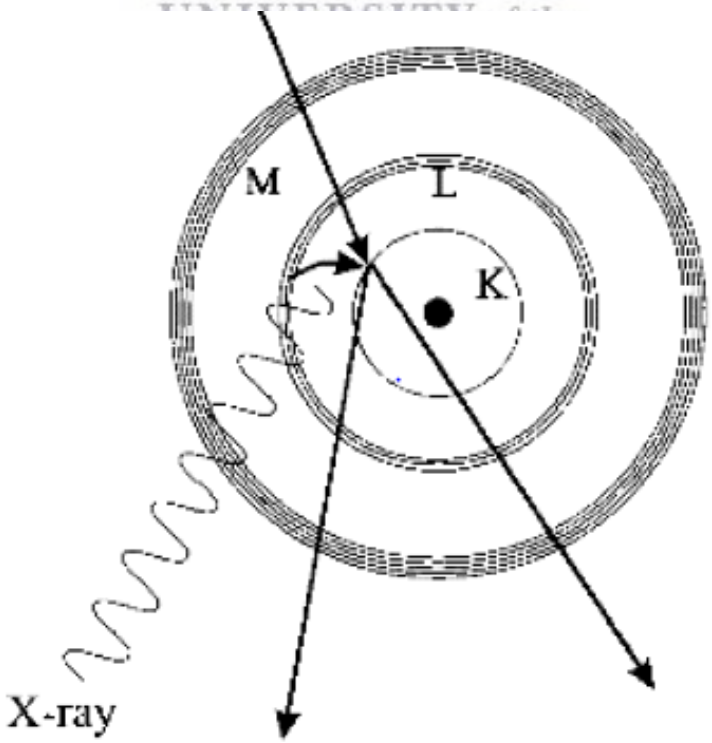

Figure 3.12: Schematic diagram of inner electron shells of atoms [3.2]

Since the energy levels of each atom are determined by its atomic number, the energy of the characteristic x-ray is unique for every element; hence the x-ray signal collected can be used for elemental analysis during energy dispersive x-ray spectroscopy (EDS). Due to scintillation damage upon impingement of x-rays on their surface, a semiconductor detector is preferably used for the detection of x-rays, as it also helps in dispersing the x-rays according to their energies. A typical semiconductor detector used for this purpose is usually in form of a thin plate that is mounted on the objective aperture without any interference with the beam and is made up of semiconductor crystals such as Si or germanium (Ge) with a beryllium (Be) window. When the x-rays strike the surface of the semiconductor crystal, the electrons in the crystal absorbs the x-ray energy, which is sufficient to overcome the energy-gap (E_g). They are thus excited from the valence band (V_B) to the conduction band (C_B) with the number of excited electrons proportional to the x-ray energy. Recombination of the electron-hole pairs is restricted by the presence of an electric field in the depleted region called the p-n junction in the semiconductor crystal used. However, due to dominant absorption of x-rays by the Be-window, elements lighter than sodium (Na) cannot be detected. Thus, for analysis of light elements, one requires a specialised technique, as will be discussed in section 3.4 [3.2]. The electric current produced during this process is contacted to a thin gold (Au) layer and then to an amplifier where it is amplified into electric pulses. An analogue-to-digital converter (ADC), that is built in to a multichannel analyser (MCA), digitalises the amplified signal into electric pulses, which are then sorted according to their energy, by the MCA. In addition, the MCA counts the number of x-rays striking the semiconductor crystal at each energy level, thereby producing an intensity distribution which can be used to plot typical a EDS spectrum, as shown in figure 3.13 below [3.1, 3.2].

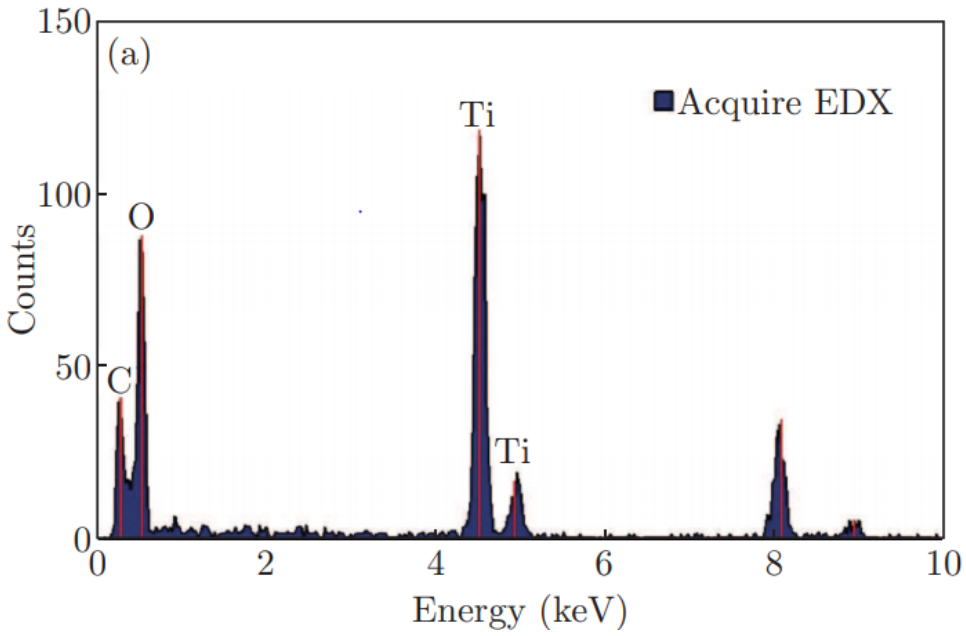

Figure 3.13: Energy dispersive spectroscopy spectra of pure TiO2

3.3 Sample Preparation

Samples to be studied under SEM need to be electrically conductive, since the instrument column is very sensitive to *charging*. Charging forms as a result of rapid impingement of charged particles on the surface of non-conductive samples. This causes the deflection of electron beam by the charged particles which build up on the surface of the sample, resulting in overall loss of image quality. For this reason, non-conductive samples are required to be coated with conductive material such as gold (Au), palladium (Pa) or copper (Cu). The coating of the samples does not only prevent the damage on the instrument or loss of resolution, but also prevents damage of the specimen, which results from heating of the specimen. Powdered samples to be studied in the SEM need to be adhered on a metal surface such as copper and the dusting eliminated as any remnant powder particles will be injected in the chamber of the microscope, which is a high vacuum zone. Out-gassing samples need to be monitored prior to the injection into the sensitive column of the instrument. Both powder and out-gassing samples are important to consider since any particle found in the column will interact with the beam, which will also result in loss of quality in the images. [3.2, 3.10]

In this study, the TiO_2 nanotube samples that were examined under the scanning electron microscope were coated with carbon. The coating was performed on Emitech K950X carbon

coater (shown in figure 3.14(a)) that was operated at high vacuum (10^{-8} Pa). For each sample, the sputter coating was performed twice with each run taking up to approximately five minutes. This was done to establish a uniform conducting layer on the surface of the sample since it purveys very good conductivity and improves image quality. Moreover, to obtain the cross-sectional images of the samples, they were either polished, bent and/or scratched with razor blade as to disturb the intact film. A Zeiss Auriga FEG-SEM shown in figure 3.14 (b) that is hosted within the Department of Physics and Astronomy of the University of the Western Cape was used to investigate the surface morphology and topology of the samples. The instrument was operated at electron beam energy of 5 keV during imaging, with varying working distance (5-10 mm) and magnification. Furthermore, the instrument is equipped with an Oxford instruments X-Max solid state drift detector for EDS measurements; an accelerating voltage of 20kV was used to collect good signal-to-noise ratios during spectrum collection.

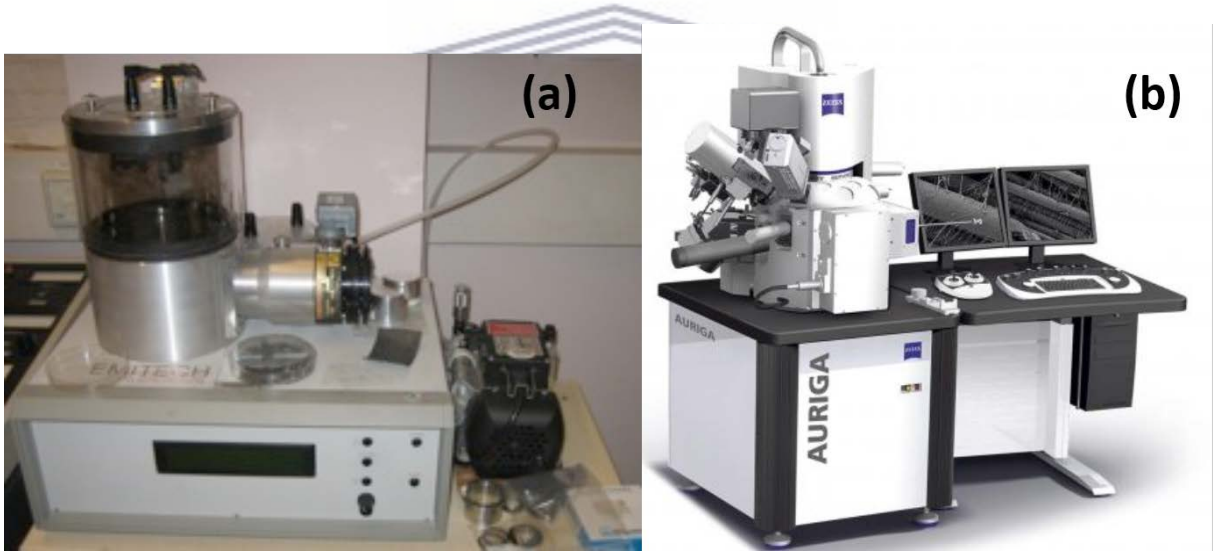

Figure 3.14: Pictorial representation of (a) Emitech K950X carbon coater and (b) Zeiss Auriga field-emission scanning electron microscope hosted at the University of the Western Cape.

3.4 Transmission Electron Microscopy

3.4.1 Introduction

The TEM was first invented in the 1930s by Ruska and Knoll following a series of experiments Germer, Davisson, Thompson and Reig on electron-diffraction to demonstrate the wave nature of electrons [3.11]. The invention of the TEM was motivated by the limited resolution of 200 nm in light microscopes at the time. TEM developments which satisfied the need of material scientists to study thin specimens were perfected in 1950s by the collaboration of Bollman from Switzerland and Hirsch from Cambridge in United Kingdom; they also developed the widely used electron diffraction theory.

Modern TEMs permit the manipulation and modelling of matter at dimensions of 1-100 nm and are operated at intermediate potentials of 200-400kV [3.2]. The use of such high accelerating voltages, compared to 1-30kV used in SEM and electromagnetic lenses with corrected spherical and chromatic aberration coefficient, has enhanced the resolution to a fraction of a nanometre [3.9]. This enables the operation of high-resolution TEM (HRTEM) and provides material scientists with a tool of imaging atomic planes of thin specimens, thereby extracting useful information from the transmitted signals. Furthermore, TEMs coupled with modern spectrometers allow investigations of elemental analysis by means of a superior technique, to EDS, called electron energy-loss spectroscopy (EELS) and probing for the chemical bonding nature of samples via electron energy-loss near edge structure (ELNES) at the nanometre scale. The superiority of EELS is ascribed to the fact that the technique can be used for identification of light elements, which are not easily detected by conventional elemental analysis during EDS. Further information, such as the crystal structure and fine structure of single nanoparticles (or nanotubes, nanowires, *etc.*) can be obtained by operating the TEM in selected-area electron diffraction (SAED) mode and by performing EELS imaging coupled with scanning TEM (STEM-EELS), respectively [3.9].

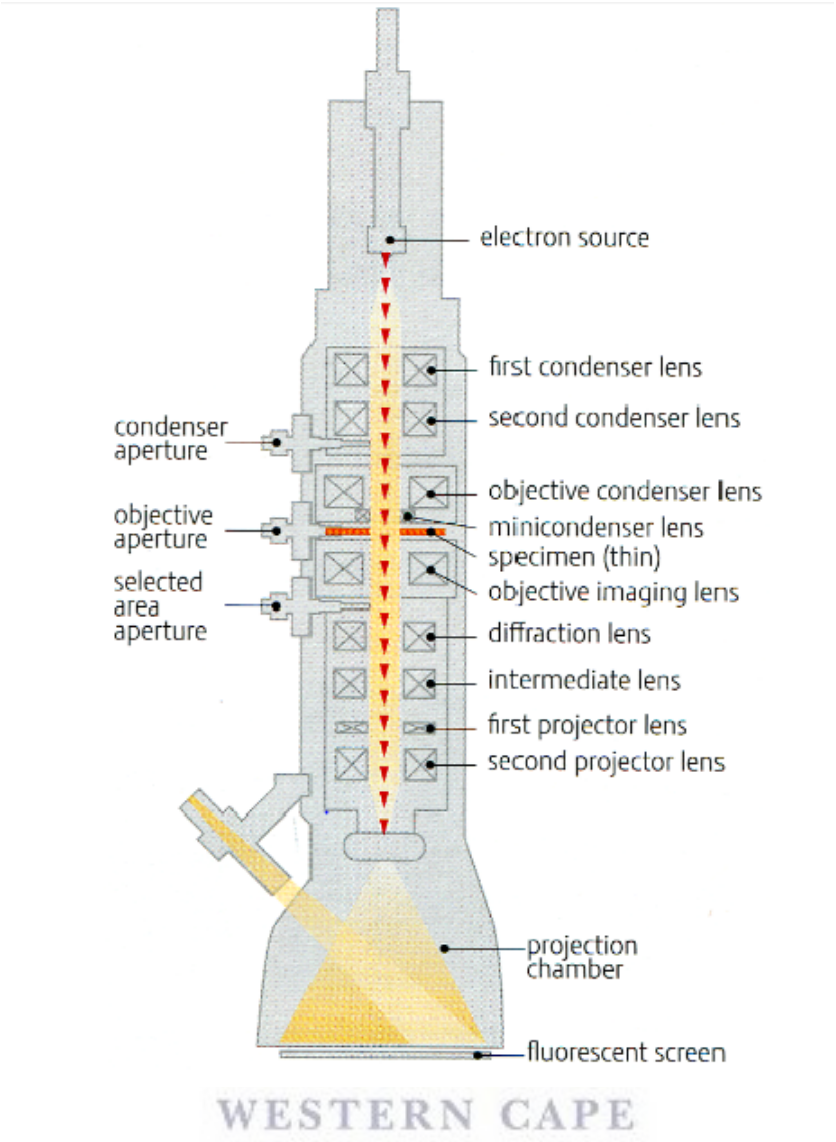

Figure 3.15: TEM schematic with all the components labelled [11].

3.4.2 Operating Principle of the Transmission Electron Microscope

Similar to the SEM, the operation of the TEM begins with an electron gun, which generates electrons used to illuminate a thin specimen. However, unlike the case in SEMs, thermionic guns are commonly used in TEMS, with biased voltages ranging 200 and 400 kV, which is much higher than that applied in operation of the SEM. Reason for this high accelerating voltage is to obtain sufficient electron transmission from the bottom of the specimen after interaction with the atoms of the specimen [3.2]. As the electron cloud diverges below the gun crossover (figure 3.1 and 3.2) and enter electromagnetic lenses, they are once more processed by two condenser lenses, C1 and C2, as shown in figure 3.15. The presence of these two lenses

just below the gun permits control over the magnification of the electron beam and the area of the specimen to be illuminated with C1 operated at strong magnetic to demagnify the diverging electron beam whereas C2 operated at weaker magnetic field control the convergence angle of the beam, hence the focal point on the specimen. Moreover, a condenser aperture determines the intensity of the electron beam and selects an area on the specimen that will be illuminated with the parallel electron beam [3.2, 3.9].

Electrons emanating from the condenser lens system hit the selected surface of the thin specimen mounted in the specimen chamber, situated inside objective lens pole pieces, are transmitted through the specimen into the objective lens system where they are used by the first objective lens to produce a first intermediate image and/or diffraction pattern, which is then enlarged by means of projector lenses and viewed on the display screen [3.2]. The first objective lens, sometimes referred to as the *diffraction or intermediate lens*, can be tuned between two modes: the diffraction mode and image mode, depending on the desired information required. For studies which require just images of the sample, the projector lens in switched to image mode and focuses on the objective lens, whereas in studies where diffraction patterns are needed, the projector lens is switched into diffraction mode, which displays the diffraction pattern at the back-focal plane of the objective lens onto the display screen.

Thus far, the discussed formation of TEM images consists of contributions from both the elastically and inelastically scattered electrons. These types of images show diffused backgrounds, which degrades the image quality. This is ascribed to the presence of inelastically scattered electrons, which are known to degrade image quality, as is the case in the SEM [3.2]. To counter for such a loss in image quality, modern TEMs are equipped with energy filters, situated just below the specimen. These are devices that can be tuned to allow only elastically scattered electrons to participate in image formation, hence improving image quality. In addition, the use of energy filters such as the Gatan image filter (GIF) is of importance in quantitative analysis during EELS [3.2, 3.9].

3.4.3 Contrast Mechanisms

Contrast is a term used to define differences in intensities between two adjacent areas of the specimen and is of importance in TEM imaging as it enables extraction of meaningful information about the specimen. When high resolution imaging is not necessary, contrast is

achieved by narrowing the objective aperture, allowing only electrons which pass closer to optical axis to contribute to image formation. In the absence of the specimen the resulting image would appear bright whereas in presence of thick specimen (in terms of its density) the image would appear dark; hence the two imaging modes are called bright-field and dark-field imaging respectively with contrast mechanism employed being *mass-thickness contrast* [3.2]. Usually, TEM micrographs are bright-field images while dark-field images are produced when TEM is operated in scanning (STEM) mode in presence of a high-annular angular dark-field detector (HAADF). Since high resolution is necessary in STEM, the use of FEGs with beam diameter of 0.2 nm [3.9] offers ability to image single atom (i.e to study structure of catalyst) and atomic planes present in crystalline specimens. Atoms with large atomic number (Z) appear bright in dark-field images since the inelastic scattering ability is proportional to the square of Z. This type of contrast mechanism is known as *Z-contrast* and it is of importance in studying compositions of complex structures together with atomic plane imaging which permits extraction of information about interplanar d-spacing of crystalline specimens [3.2, 3.9].

In addition to mass thickness contrast and the Z-contrast, there are other two contrast mechanisms exploiting the wave nature of electrons, namely diffraction contrast and phase contrast, which are of importance in imaging diffraction patterns and atomic planes at high magnifications, respectively. Diffraction refers to scattering of electrons by means of coulomb fields generated by the atomic nuclei of crystalline specimen. Such scattering increases in intensity at plane orientations in which Bragg's law (discussed in later sections) is satisfied with planes scattering the most showing strong contrast in the diffraction image. However, forming a diffraction image in dark-field imaging requires that the objective aperture is displaced so that diffracted signals contribute to the image, resulting in contribution of off-axis electrons, which degrade image quality. Tilting the specimen while the objective aperture is still positioned to select electrons near the optical axis has proven to be and efficient improvement of quality in the formed diffraction image.

Supplementary to the crystal information extracted from diffraction images, high magnification phase contrast images enable extraction of information about atomic planes of single crystalline material, grain boundaries in polycrystalline materials and also thin film-substrate interfaces [3.2, 3.9]. Phase contrast arises as the consequence of the varying electron wave phase after scattering by atoms of a thin specimen. Because modern TEM have high resolution, images

which utilise the phase contrast mechanism are formed by displacing the aperture, thereby collecting both the deflected and incident electrons by mean of digital cameras such as *charge-coupled devices* (CCDs), unlike in the case of the above-mentioned contrast mechanisms where an aperture is used to select electrons that can contribute to the image [3.11].

3.4.4 Charge-Coupled Devices

Charge-coupled devices are metal-insulator silicon devices, shown in figure 3.15 (a) that are used to store charge generated by the electron beam. The CCD camera consists of two-dimensional small light detectors known as pixels that are stacked to form pixel arrays (or capacitors) which are several mega-pixels in size, as shown in figure 3.15 (b). The two-dimensional pixel frames are electrically separated by the potential well in each pixel cell. When the incident beam (or photons) strikes the surface of the specimen, each small point of the specimen (specimen pixel) is collected and recorded on the element of a framestore which typically consists of ~1200 × 1000 CCD cells (pixels) [3.2].

The recorded specimen pixel (input) is stored as numbers between 0 and 255 depending on the intensity of the specimen pixel and used for image formation. When forming an image, pixel shifting along the line is established by varying the potential well of the cells which results in serial registering of data fed into the build-in amplifier, which then converts the optical and/or electronic inputs into electronic signals. Shifting occurs until the frame is completely empty and is re-exposed for the next acquisition when the instrument is operated in scan mode.

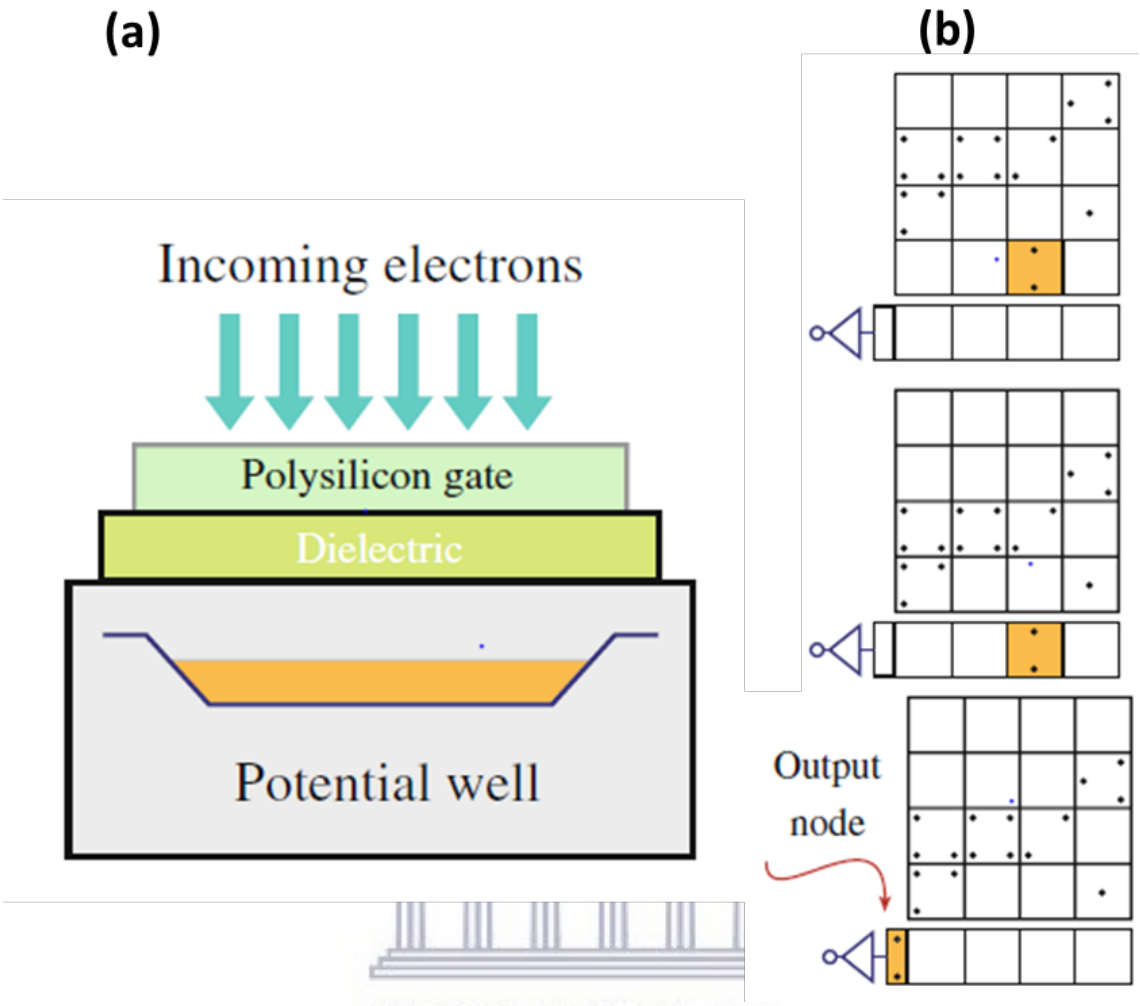

Figure 3.16: Schematic representation of (a) a single cell in a CCD array, and (b) its operation principle [3.11]

However, in the TEM data is registered parallel. This means rather than pixel by pixel or line by line registering of data, the whole frame can be transferred to the adjacent storage array leaving the main frame array empty and ready for another acquisition. This is called full-frame transfer and is essential for HRTEM data acquisition since it permits faster acquisition rather than the longer exposures which may result in overall loss of resolution as result of external vibrations, specimen drifts, *etc.* It is recommended that for better performance of CCDs they are thoroughly cooled as to enhance the signal-to-noise ratio, as well as the use of good electrodes for efficient charge transfer purposes [3.2, 3.11].

3.4.5 Electron Diffraction

Electrons used in electron diffraction studies encounter scattering by specimen atoms in the same way as x-rays (discussed in section 3.7) are scattered by atoms of bulk samples, generating signals as shown in figure 3.9. Of particular importance in TEM diffraction studies are the elastically scattered electrons that are used in dark-field imaging to image diffraction patterns on which crystallographic information about the specimen can be extracted. When the incident electron strikes the surface of a crystalline specimen with atomic plane arrangements that are nearly parallel to the incident beam, electrons are scattered by atoms of the specimen at point A and B into small angles, 2θ, as shown in figure 3.16 below [3.2]

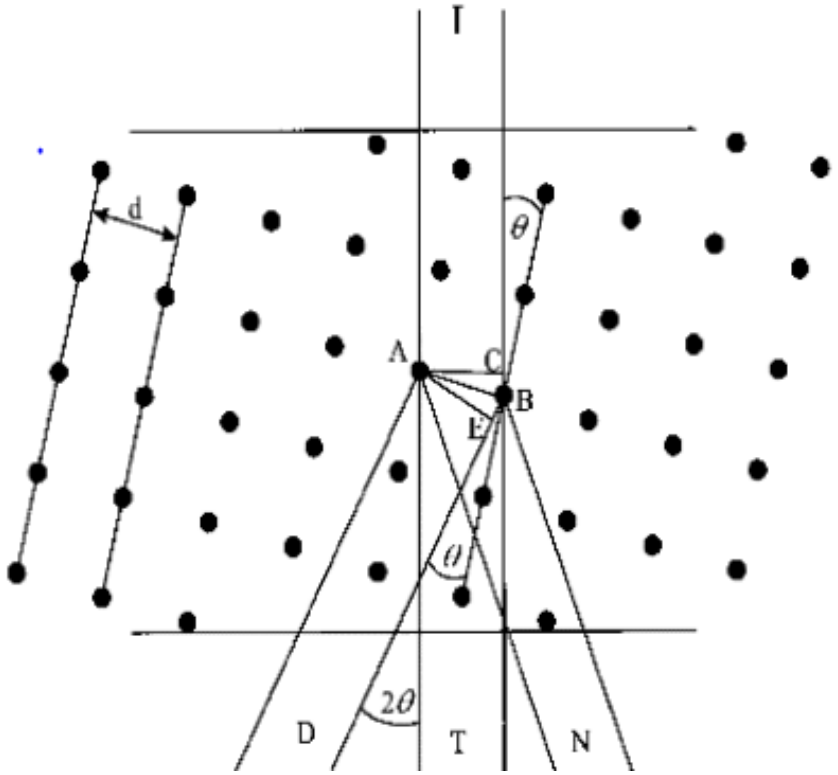

Figure 3. 17: Scattering of the incident electron beam by the nearly parallel atoms of single crystal of the specimen [3.2]

The scattered rays at D, shown in figure 3.17, are in-phase if and only if their path distances vary by the integer multiple of the electron wavelength and this is mathematically represented by

$$CB + BE = n\lambda \tag{3.5}$$

where *n* is an integer number (or sometimes called the order of diffraction) and λ the wavelength of the electron beam. From simple geometry and trigonometry, it follows that triangles ACB and ABE are similar and hence CB and BE are equivalent to *dsin(θ)* when using. Thus equation (3.5) can be rewritten as:

$$2dsin(\theta) = n\lambda \tag{3.6}$$

This is the mathematical representation of the known Bragg's Law used in x-ray diffraction studies which states that the diffraction pattern can only be obtained from those incident electron waves whose deflection angle (θ) is the solution to equation (3.6). However, Bragg's law is also applicable in electron diffraction studies owing to wave nature property of electrons. Because electrons used in this study are very energetic (i.e short wavelength), the resulting diffraction angles for a known standard, such as Al are so small, the term *sin(θ)* can be approximated to θ; and considering only the first order of diffraction (*n=1*), Bragg's law can be reduced to

$$2d\theta = \lambda \tag{3.7}$$

The above equations simplify electron diffraction studies and its analysis as it signifies that strong diffraction occurs to those atomic planes nearly parallel to the incident electron beam and that the atomic spacing *d* can be computed by using the indexed diffraction pattern according to its miller indices (*hkl)* in the equation below.

$$d_{hkl} = \frac{1}{\sqrt{\frac{h^2}{a^2}+\frac{k^2}{b^2}+\frac{l^2}{c^2}}} \tag{3.8}$$

The crystal lattice parameters a, b and c are also determined provided the spacing is known from other analysis techniques, to be discussed in sections that follow [3.2, 3.9, 3.11].

3.4.6 Formation of Diffraction Patterns in the Transmission Electron Microscope

Sharp diffraction patterns in the TEM are obtained when a well collimated electron beam hits the surface of the crystalline specimen whose atomic planes are almost parallel to the incident beam as in figure 3.17. The presence of the condenser aperture ensures the fulfilment of this requirement as it eliminates electrons which have paths deviating from the required parallel beam, thus restricting the area to be illuminated on the specimen. Alternatively, a selected area aperture is inserted into the objective lens plane below the specimen to select certain electrons to contribute in the formation of the diffraction pattern. During the interaction of the specimen with the parallel beam, some of the incident electrons pass through the thin specimen without being diffracted and hits the fluorescent screen (sometimes called the operator's monitor) which is located a distance, L known as the camera length, below the specimen, as shown in figure 3.18 [3.2].

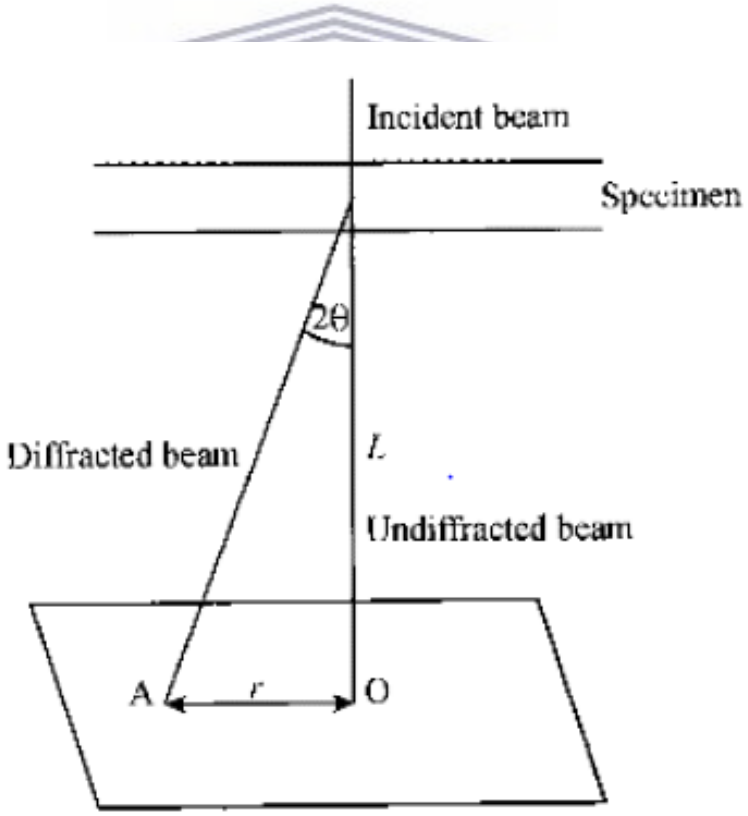

Figure 3.18: Simplified diagram illustrating simple geometry of diffraction formation [3.2].

However, some incident electrons are diffracted through an angle 2θ hit the screen at position A, which is a distance, r, away from the undiffracted incident electron. Simple geometry proves that small angle diffraction results to

$$2\theta = \frac{r}{L} \tag{3.9}$$

Combining equation (3.9) and the Bragg's equation (3.7) gives

$$\frac{r}{L} = \frac{\lambda}{d} \tag{3.10}$$

Rewriting the above equation gives $L\lambda = rd$ in which $L\lambda$ is called the *camera constant* since it is independent of the specimen. It is evident that the d-spacing is obtained by an inverting distance, r; this allows material scientists to directly obtain the atomic d-spacing from diffraction patterns [3.2]. Moreover, single crystalline specimen gives diffraction in form of "spot" with corresponds to atoms in the diffracting plane and in polycrystalline specimens where crystals are randomly orientated, the resulting diffraction pattern form rings with spots that are very close to each other in a ring shape. TiO_2 NTs are polycrystalline, hence diffraction pattern expected to be obtained should be in form of rings.

3.4.7 Structure Factor

The structure factor is one of the most valuable properties in both x-ray and electron diffraction since is provides information about the variation in diffraction intensities. This observed variation in diffraction intensity is attributed to the difference in areal density of atoms in different planes of the crystal (as mentioned in section 3.3.2) and their position in the crystal. Determining the structure factor, which is related to the amplitude of the incident beam and the diffracted beam by the proportionality relation below gives direct indication of the diffraction intensity

$$A_{hkl} \propto F_{hkl} A_0 \tag{3.11}$$

where A_{hkl} and A_0 represent the amplitude of diffracted and the incident beam respectively, while F_{hkl} is the structure factor of (*hkl)* planes. In theory, the structure factor is the collection

of the entire scattering of electrons by individual atoms in the diffracting plane. Adding all the scattering contributions in from all atomic planes gives:

$$F_{hkl} = \sum_{n=1}^{m} f_n(\theta)\exp[-2\pi i(\, hx_n + ky_n + lz_n)]\,, n = 1, 2, 3\,, \ldots \qquad (3.12)$$

In the above equation, the factor $f_n(\theta)$is the scattering factor of the nth atom which determines the amplitude of the diffracted beam in the θ direction from the atoms. The complex part of the equation takes into consideration the phase of each wave while the (hkl) and (x_n, y_n, z_n) represents the plane and the co-ordinates of the nth the atoms respectively. A typical example of the use of the structure factor in determining the intensity of the diffraction spot is to consider a cubic crystal structure such as face-centred cubic (FCC) or body-centred cubic (BCC) whose diffracting planes are well known from their selection rules and the co-ordinates of their atoms. In the FCC crystal, the combination of (hkl) values which gives rise to diffraction have to all odd or all even, whereas in BCC crystal the (hkl) combination can contain mixture of odd and even value. However, the summations of these combinations need to give an even number for the diffraction to occur. Thus, it is only those planes responsible for diffraction in the FCC or BCC crystal will give a non-zero structure factor. The zero structure factors mean that there is no diffraction occurred on that particular plane; say for example the (100) plane of the FCC crystal, thus the intensity is zero. Such planes are called the forbidden reflection and are usually omitted when calculating the structure factor to simplify the math [3.2, 3.8-3.9, 3.11].

3.5 Electron Energy Loss Spectroscopy

3.5.1 Introduction

Electron energy loss spectroscopy (EELS) is a technique used mostly by material scientists to study the chemistry and electronic structure of the specimen, which in turn reveals detailed information about the bonding of atoms in the specimen, atomic structure (or crystal structure) and the energy band-gap of semiconducting specimens [3.11, 3.14]. Recent advances in monochromators for electron guns combined with availability of lenses with corrected spherical and chromatic aberrations has enabled performance of EELS studies at energy resolution of less than 100 meV [3.11]. Thus, this makes EELS a preferred microanalytical

technique to study heavy and light elements efficiently compared to EDS (discussed in section 3.3.4) which cannot be used to study elements lighter than sodium [3.2].

When the monochromatic electron beam interacts with the specimen, a variety of signals (elastic and inelastic scattered electrons) is produced in the interaction volume (as described in section 3.3.2). Of particular interest to the EELS technique are the inelastically scattered electrons who suffer detectable energy loss (ΔE) upon their interaction with atoms of the specimen. Inelastically scattered electrons lose their energy in four ways, including energy loss of: (i) less than 1 eV by excitation of phonon vibration in solids; (ii) about 1 eV due to single excitation from the valence band (V_B) to higher energy states in the conduction band, C_B; (iii) 30 – 50 eV by collective excitation of electrons from V_B into C_B in semiconductor material or by plasmon excitations; and (iv) few hundreds or thousands of eV by excitation of inner-shell electrons as mentioned in section 3.3.2 [3.2, 3.10-3.15]. The signals emanating the specimen are detected and dispersed by means of post or an in-column magnetic prism spectrometer to generate EELS spectra, which are recorded by means of a photodiode array (PDA) or CCD [3.11]. For the purpose of this study, the TEM instrument used for characterisation of TiO_2 NTs is equipped with post-column Gatan-Image Filter (GIF, model GIF-2001) spectrometer. Thus, only the operation principle of post-column GIFs will be discussed in the next section.

3.5.2 Acquisition of EELS spectra using Magnetic Prism

The post-column Gatan-Image Filter used for acquisition of EELS consists of (i) an entrance aperture, (ii) focusing or alignment coils, (iii) a magnetic prism with magnetically isolated drift tube, (iv) multipole system, and (v) the detection system in the form of a CCD array or PDA, as shown in figure 3.18 [3.11].

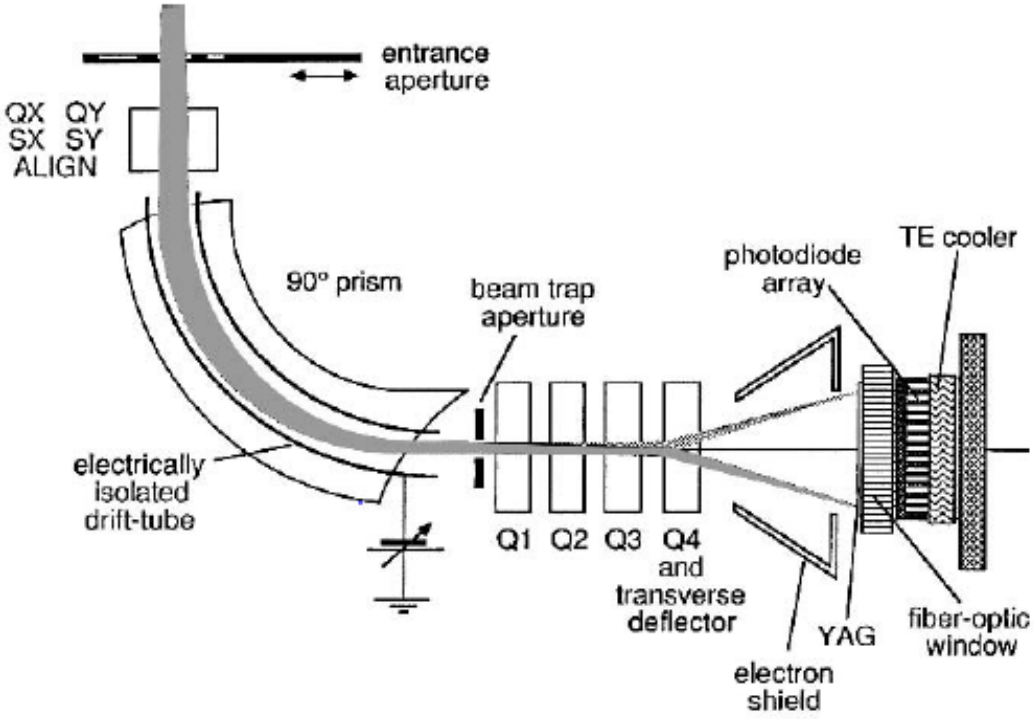

Figure 3.19: Schematic of typical Gatam image filtering spectrometer used for acquisition of EELS spectra [3.15].

The diverging electrons emanating at the back of the specimen enters the spectrometer through the entrance aperture, and are converged by the alignment coils towards the central axis (axis of the incident beam) before entering the magnetic prism [3.15]. Inside the prism, there exists a uniform magnetic field in the direction perpendicular to the velocity of the incoming beam of electrons. Electrons entering magnetic prism move through a circular orbit, with radius of curvature given by equation (3.13), proportional to both the velocity of the electrons and the intensity of the magnetic field

$$R = \left(\gamma m_0 / eB\right)v \tag{3.13}$$

where $\gamma = (1 - \frac{v^2}{c^2})^{\frac{1}{2}}$ is the relativistic factor, m_0 the rest mass of an electron, e the electron charge, B and v the magnitude of the magnetic field intensity and speed of electrons, respectively [3.13]. Equation (3.13) reveals that electrons which have lost energy during their interaction with specimen atoms will have lower velocities, thus smaller curvature radius compared to the elastically scattered (zero-loss) electrons, whose radius of curvature will be

larger as a result of their high velocities, which is equivalent to the velocity of the primary electrons as shown in figure 3.20 below.

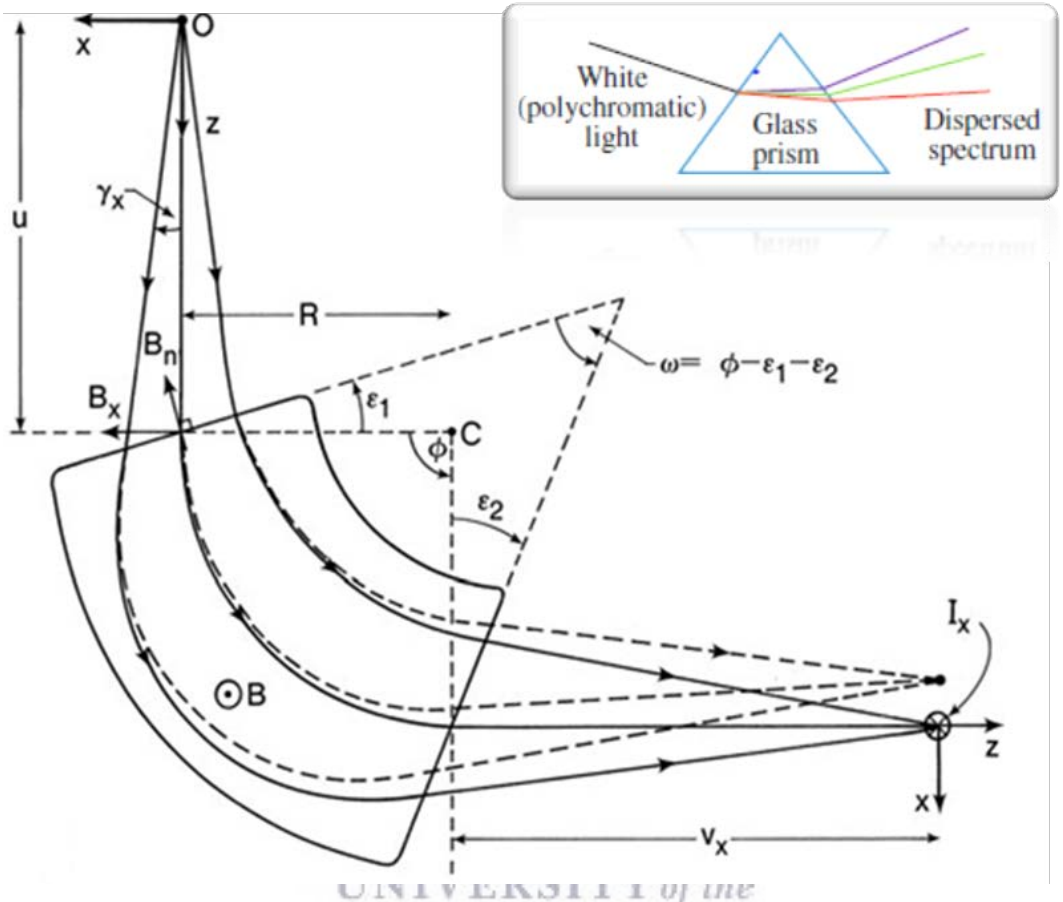

Figure 3.20: Working principle of magnetic prism to disperse electrons according to their energy loss during acquisition of EELS spectra [3.13]

The deflection of electrons inside the magnetic prism according to their energy loss, thereby resulting in energy dispersion, is analogous to the principle of the glass prism shown in the inset of figure 3.20 where the polychromatic light entering the prism is dispersed into light of different wavelengths (colours) [3.11]. However, in the magnetic prism the dispersed electrons exiting the prism are focused to the dispersion/image plane I_x, as shown in figure 3.20, while this focusing is not observed in a glass prism. The focusing in the magnetic prism occurs because electrons with positive γ_x (measured radially) travel greater distances in the magnetic field, thereby experiencing larger deflection compared to electrons which have negative γ_x which travel shorter distances, as shown with dashed lines in figure 3.19 [3.11,3.13, 3.15].

Prior to the acquisition of EELS spectra, a series of quadrupoles, shown in figure 3.19, are used for magnification and further focusing of the electron dispersion prior to recording on the PDA or CCD, placed at the dispersion plane. Modern instruments make use of CCD arrays for acquisition of EELS spectra over PDA due to the improved resolution, better photon sensitivity, high dynamic range and straight forward recording offered by CCDs. Since EELS spectra consist of wide energy range of electrons, both PDA and CCD are coupled with an yttrium aluminium garnet (YAG) scintillator that converts electrons into photons that are proportional to the incident radiation to reduce the radiation damage possibilities [3.11, 3.15]. When photons from the scintillator falls onto the CCD detector with 100 × 1340 arrays of 25 μm pixels, a full frame transfer (as described in section 3.3.3) of the array permits efficient collection of EELS spectra with good resolution over a short exposure periods compared to multiple integration in PDAs as a result of its saturation at counts of approximately 16 000 electrons. Furthermore, in the presence of beam a trap aperture as shown in figure 3.19, electrons furthest from the optical axis are filtered, thereby allowing simultaneous recording of selected EELS and the performance of energy filtered TEM (EFTEM) imaging [3.11].

The resulting EELS spectra recorded by CCD detector has two dominant artefacts namely; dark current and the ghost peak. Dark-current artefacts form as result of background noise in detectors while the ghost peaks arises as result of overexposing the YAG scintillator to the high energy radiation such as the zero-loss electrons. The former can be minimised by subtracting the pre-recorded spectrum in the absence of electrons from the gathered EELS data, whereas the later can be minimised by subtraction of the extrapolated data using a decay power law, since ghost peaks decay over exposure times. Hence, the resulting EELS spectrum reveals true proportionality of the intensity and the energy loss, thus enabling extraction of meaningful information about the specimen [3.11, 3.13, 3.15].

3.5.3 Characteristics of an Electron Energy Loss Spectrum

A typical EELS spectrum is divided into two regions namely the *low-loss* and the *core-loss* regions, as shown in the schematic of figure 3.21. The low-loss region consists of the zero-loss peak (ZLP) which is the most intense peak that is constituted mainly by elastically scattered electrons (no energy loss) and a numerous number of plasmon peaks (although the schematic show only one peak), while the core-loss region consists of only ionisation peaks or sometimes

called edges. The former and later arise as a result of the processes described in section 3.5.1 [3.2, 3.11 – 3.15].

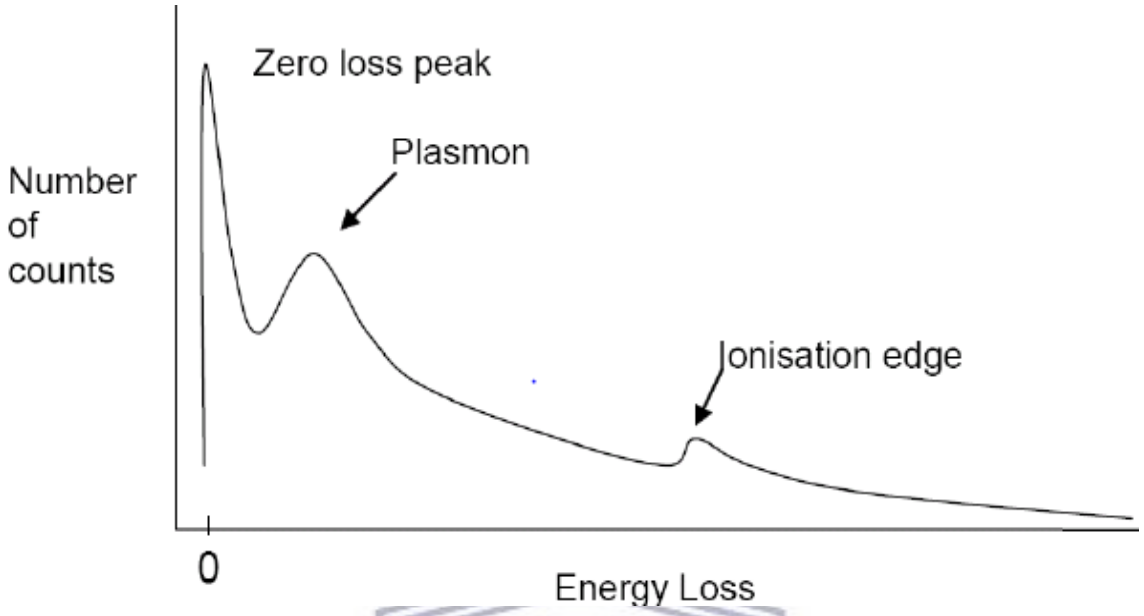

Figure 3.21: Schematic of a typical EELS spectrum with exaggerated peak broadening [3.14].

Theoretically, the ZLP is supposed to have zero width, but due to broadening effects caused by the electron source and instrumentation used, an electron energy spread is observed and is measurable; the result in figure 3.20 is exaggerated to highlight this phenomenon [3.2, 3.11]. For microanalytical studies, the ZLP is of no significant importance as it purveys no useful information about the specimen. Nevertheless, microscopist use this peak when performing instrument calibration because of its known centre and measurable full-width half maximum (FWHM) that enables performance of beam alignment and determination of instrument resolution, respectively [3.2, 3.11].

Several number of plasmon peaks with intensities that get progressively weaker towards higher energy losses are also not often used for microanalysis since their occurrence is very similar for all elements. Thus, ionisation edges that are observed at higher energy losses between 100 eV and 2000 eV [3.2] are the commonly used peaks since they are characteristic for each element and enables identification of elements present in the specimen. For example. The ionisation edge occurring from 456 eV to approximately 465 eV can only be that of Ti-$L_{3,2}$

edges as shown in figure 3.21(a) and those occurring from 520 eV to approximately 540 eV can only be ionisation edges of oxygen's K edge (O-K). Quantitative analysis is also performed utilising this region since the edge size is proportional to the number of atoms present in the specimen, thereby enabling determination of exact elemental concentration [3.2, 3.11, 3.12-3.16].

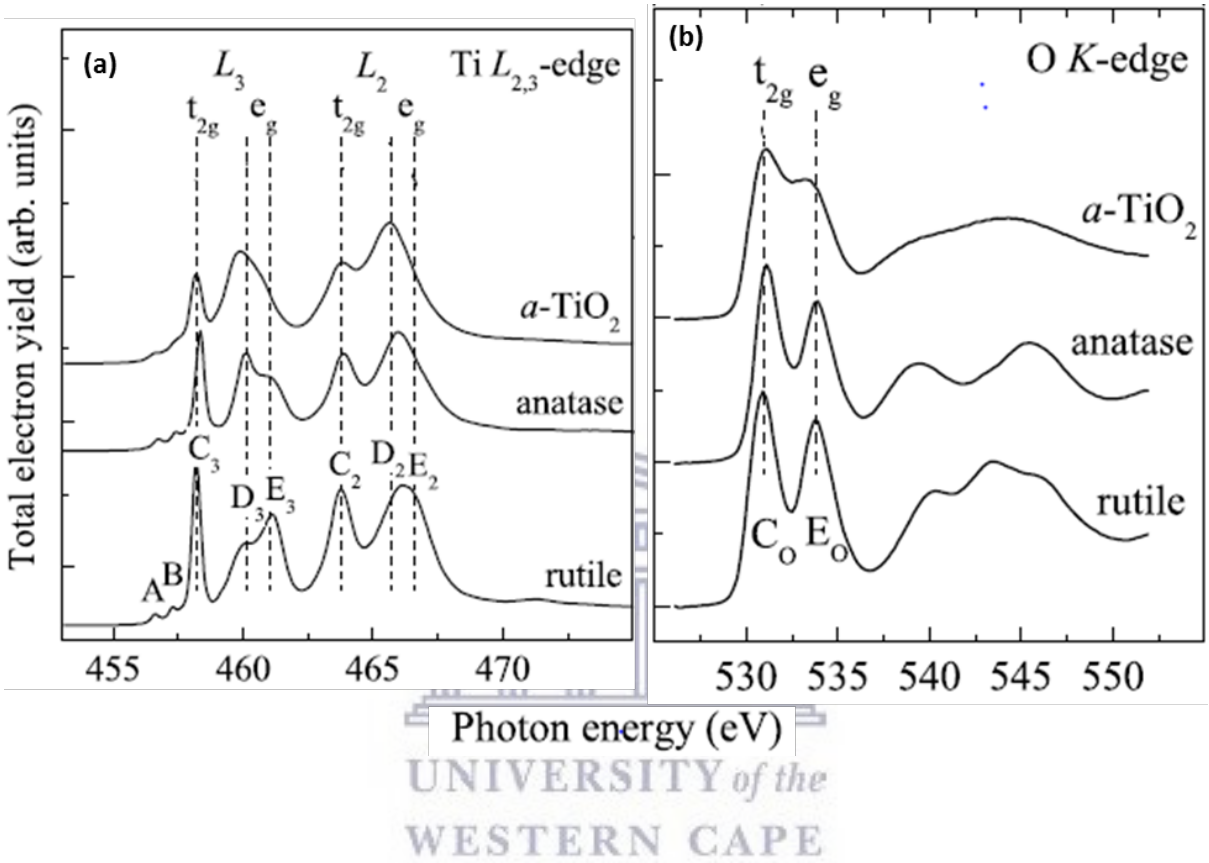

Figure 3.22: Ionisation edges of different TiO_2 polymorphs showing (a) Ti L3, 2 and (b) O K- edge of amorphous, rutile and anatase phases of TiO_2 [3.17].

3.5.4 Electron Energy Loss Spectra of Rutile and Anatase TiO_2

Figure 3.22 above compares the high-resolution Ti $L_{3,2}$ edges, also known as white lines, and O K edges of two different TiO_2 polymorphs namely, anatase and rutile, against that of amorphous TiO_2. In figure 3.22 (a), the separation of approximately 5.5 eV between the white lines in 3d transitional, which are indicative of dipole allowed ($\Delta l = \pm 1$) transitions from 2p states to d states, is ascribed to the spin orbit coupling 2p states [3.18]. This effect is common for all 3d transitional metals, but is absent in metals such as Copper (Cu) where the 3d orbitals are completely full [3.19]. A further splitting of Ti $L_{3,2}$ –edges into higher energy e_g and low

energy t_{2g} maxima is observed for all three phases. This splitting is ascribed to the presence of the ligand field, also known as crystal field, which consequently results in separation of the lowest unoccupied 3d band [3.16-3.19]. Due to large hybridisation by O ligands, the Ti e_g related peaks are observed to be broader than the t_{2g} related peak. A similar feature of band splitting is also observed for O K edges, shown in figure 3.22 (b) and is indicative of transition from O 1s core level into t_{2g} and e_g band, while the higher energy peaks are indicative of excitations into anti-bonding 2p states [3.16-3.18].

Brydson et al [3.16] observed a further splitting of Ti L_3 edge into two peaks of varying intensities with rutile having low-energy shoulder (peak) and anatase with higher energy shoulder. Similar observations were made by [3.18] as shown in figure 3.22 (a) and attributed the splitting of the e_g band as the consequence of interaction of Ti atoms with the second neighbouring shell. However, no splitting observed in the e_g of O K edge, thus this suggests that the splitting is specific to titanium [3.16]. Another noticeable feature between the $L_{3,2}$ edges of anatase and rutile is the shifting of the t_{2g} related peaks (C_3 and C_2 in figure 3.22) into higher energies compared to the t_{2g} related peaks of rutile which is attributed to the difference in energy bang gap of anatase (E_g~3.2 eV) and rutile (E_g~3.0 eV) [3.18]. Poorly discernible pre-edge peaks (labelled A and B) in figure 3.22 (a) observed for both rutile and anatase, are believed to be related to spin forbidden transitions [3.16].

3.6 Energy-Filtered Transmission Electron Microscope

3.6.1 Introduction

Energy-filtered transmission electron microscope (EFTEM) is an analytical technique that utilises the properties of an EEL spectrum to form images with enhanced contrast and resolution [3.11]. The enhancement of contrast and resolution of images are a result of use of energy-selecting that selects certain electrons to participate in image formation. The EFTEM techniques combine the information rendered by EELS (as described in section 3.5) and its enhanced spatial resolution to acquire maps that elucidate quantitatively or qualitatively the spatial distribution of any feature in an EEL spectra [3.20]. Typically, an elemental distribution map using ionisation edges and variation in chemical bonding can be obtained at good spatial resolution. As for this result, the EFTEM technique has become a powerful tool for material

scientists and biologists since it enables them to perform versatile studies on their samples and allowing them to develop sensible theoretical models to explain sample properties. In recent years, several new techniques have emerged from the standard EFTEM, such as imaging spectroscopy and EFTEM tomography. The former is a technique that creates images that contain a complete EELS spectrum, while the latter is a technique used to record three-dimensional element specific images [3.21].

EFTEM studies can be performed in dedicated EFTEM instruments that are equipped with the in-column *Omega-filter* that was developed by Zeiss and later by JOEL. Alternatively, a conventional TEM instrument can be modified by installing as an attachment a post-column GIF in the optical-column of the instrument, thereby enabling its use for EFTEM studies in the same way as dedicated instruments. As mentioned in section 3.5.1, the TEM instrument used in this study is equipped with post-column GIF (model GIF 2001), thus the techniques be discussed are those that were performed during the study.

3.6.2 Energy-Filtering of Electron Energy Loss Spectrum

a) The Energy-Filtering of Low-Loss region

The energy-filtering of the low-loss region of the EEL spectrum, also known as the Valence EELS (VEELS) has been widely used for identification of different phases in the material through the investigation of the plasmon peak shape [3.12]. This process is known as “fingerprinting” and is achieved by tuning the energy-selecting slit of the energy filter to acquire an energy-filtered VEEL spectrum which is then compared with known VEELS standards [3.11]. Through the development of proper spectral processing methods and the use of high-resolution FEGs combined with monochromators for removal of the ZLP tail, VEELS is now amongst the preferred characterisation tools used to probe for band-gap, dielectric constant and optical properties of semiconductor materials [3.12].

The information about the energy band-gap is extracted in the region just after the ZLP and before the first plasmon peak where the spectral intensity approached the intensity of the dark-current (noise) of the detector. When there are no intraband transitions occurring, the low-intensities suggest the existence of transition-forbidden region which can be directly correlated

to the separation between the valence and the conduction band of semiconductor/insulator. Measuring the energy range of the gap out to the rise of the first plasmon peak purveys information about the band-gap of the material. Furthermore, because the intensities of the properly processed spectrum reveal true information about the specimen, the information about the dielectric constant or permittivity (ε) can be extracted in the low-loss region (1-30 eV). If the "free-electron" model is assumed, the intensity of the single scattering *I(E)* is related to the imaginary part of the dielectric constant by equation (3.14);

$$I(E) = I_0 \left(\frac{t}{\kappa}\right) Im \left(-\frac{1}{\varepsilon}\right) \ln \left[1 + \left(\frac{\beta}{\theta_E}\right)^2\right] \tag{3.14}$$

where I_0 is the intensity of the ZLP, t is the specimen thickness, κ is the constant incorporating the electron momentum and the Bohr radius, β and θ_E are the collection angle and the scattering angle, respectively [3.11]. Using Kramers-Kronig analysis, which a bidirectional mathematical relation that enables the calculation of the real part from the imaginary part of complex function, the energy-dependence of the real part of the dielectric constant can be obtained.

b) The Energy-Filtering of Ionisation Edges

The energy-filtering of ionisation edges is the most extensively used technique to probe for elemental distribution and (sometimes) the concentration of a specific element by means of elemental maps or images [3.13]. However, the acquired elemental maps/images are not directly interpretable due to the existence of non-elemental-specific background in the ionisation region. As a result, two techniques namely; the "three-window" method and the "jump-ratio" method are frequently used to eliminate or reduce the unwanted background signal.

c) Three-Window Method

This method makes use of three EFTEM images that are formed from electrons that come from three different regions. The first two images are collected in the pre-edge region as shown in figure 3.23 and are used to estimate the parameters of the decay-power law background extrapolation expression, while the third image is obtained from the ionisation edge of interest. The estimated background is the subtracted from the post-edge image, thereby resulting in an

excitation image with intensities that are proportional to the number of electrons that have made the excitation [3.21].

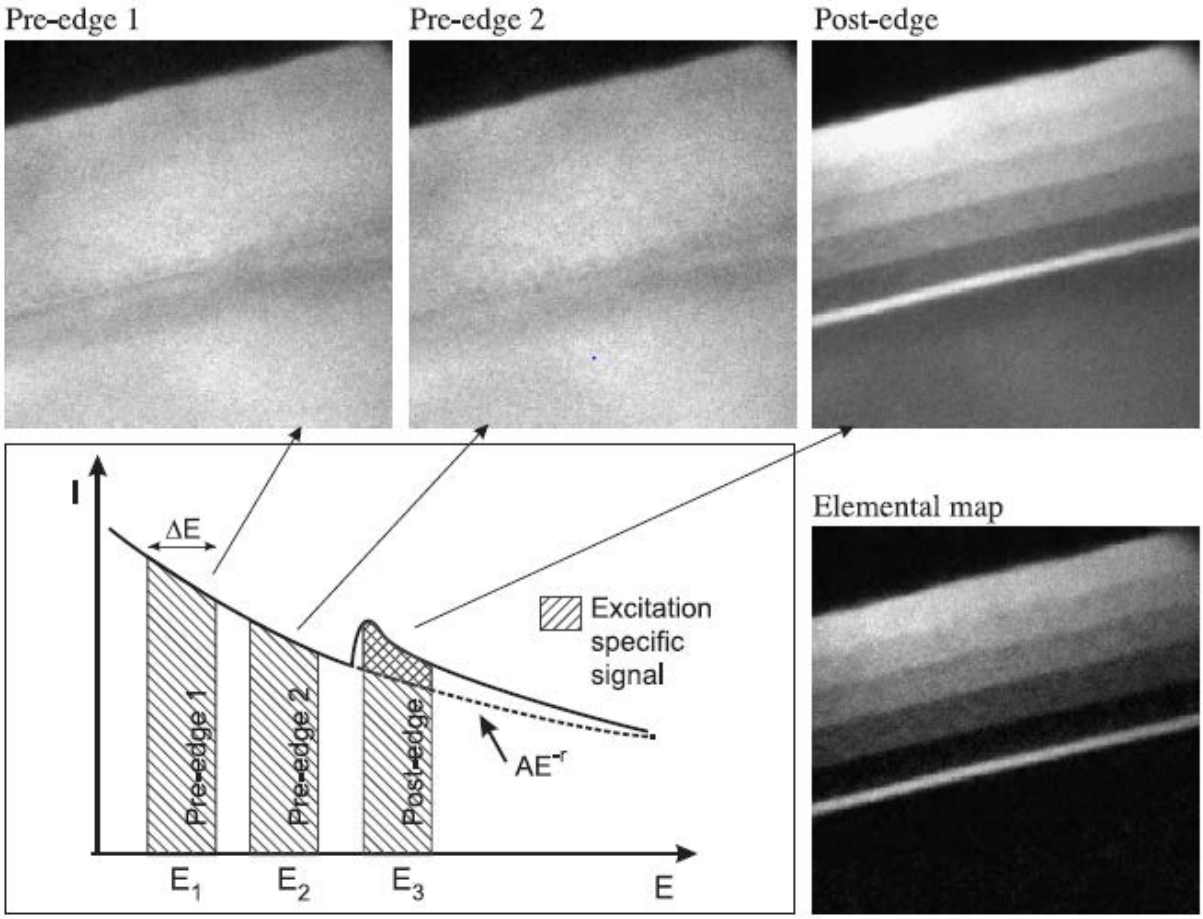

Figure 3.23: A schematic overview of a three-window method illustrating the regions into which the pre-edge images and the post-edge images were acquired to form an elemental map [3.21].

The obtained elemental map can be used to perform quantitative elemental analysis provided that the cross-section for the excitation is known. However, due to several artifacts such as drift and preservation of elastic contrast that may result in false quantification, the three-window method may not be an ideal technique. Hence, the "Jump-ratio" method would be preferred.

d) The Jump-Ratio Method

In this method, two EFTEM images are recorded from the pre-edge region and the post-edge region of the ionisation edges the same way as for three-window method. When the post-edge image is divided by the pre-edge image, a jump-ratio image is formed. The resulting image can be used for only qualitative elemental analysis due to the relative intensities that are not directly related to the excitation edge. As for this result, the quantification is lost, thus the jump-ratio image can be used to investigate chemical changes in the specimen by means of monitoring the post-edge to pre-edge ratio. Although the loss of quantification is disadvantageous for the technique, a jump-ratio method is still preferred over the three-window due to the less sensitivity to the preserved elastic contrast, reduction of drift problems since only images are required, and that the resulting image has a better signal to noise ratio (SNR) [3.12-3.14, 3.20-3.21].

3.7 Scanning Transmission Electron Microscopy

3.7.1 Introduction

The development of condenser-objective (c/o) lenses in early 1970s, with strong magnetic fields of approximately 2 Tesla between the objective pole-pieces, has seen many modern TEMs equipped with c/o lenses and scan coils, enabling operation of the instrument in scanning transmission electron microscopy (STEM) mode. Unlike conventional TEM where a parallel beam of illumination is used for imaging, STEM requires that the beam is converged to a small area on the specimen, thereby building an image of the specimen by collection of specimen pixels via a detection system (CCD) that acts as interface between transmitted signals and the viewing screen. The convergence of the electron beam in modern TEM instruments to satisfy STEM requirement is achieved by focusing the condenser lens (C2) on the specimen plane, rather than the defocusing setting in conventional TEM in the absence of condenser mini lens, thereby creating an image of C1 on the specimen plane as shown in figure 3.24 (a). Alternatively, if C2 is set to a relatively weak magnetic field such that it has no effect on the beam, the upper pole-piece of the c/o lens can operate as C3, thereby generating the smallest probe on a very large convergence angle as in figure 3.24 (b) [3.11].

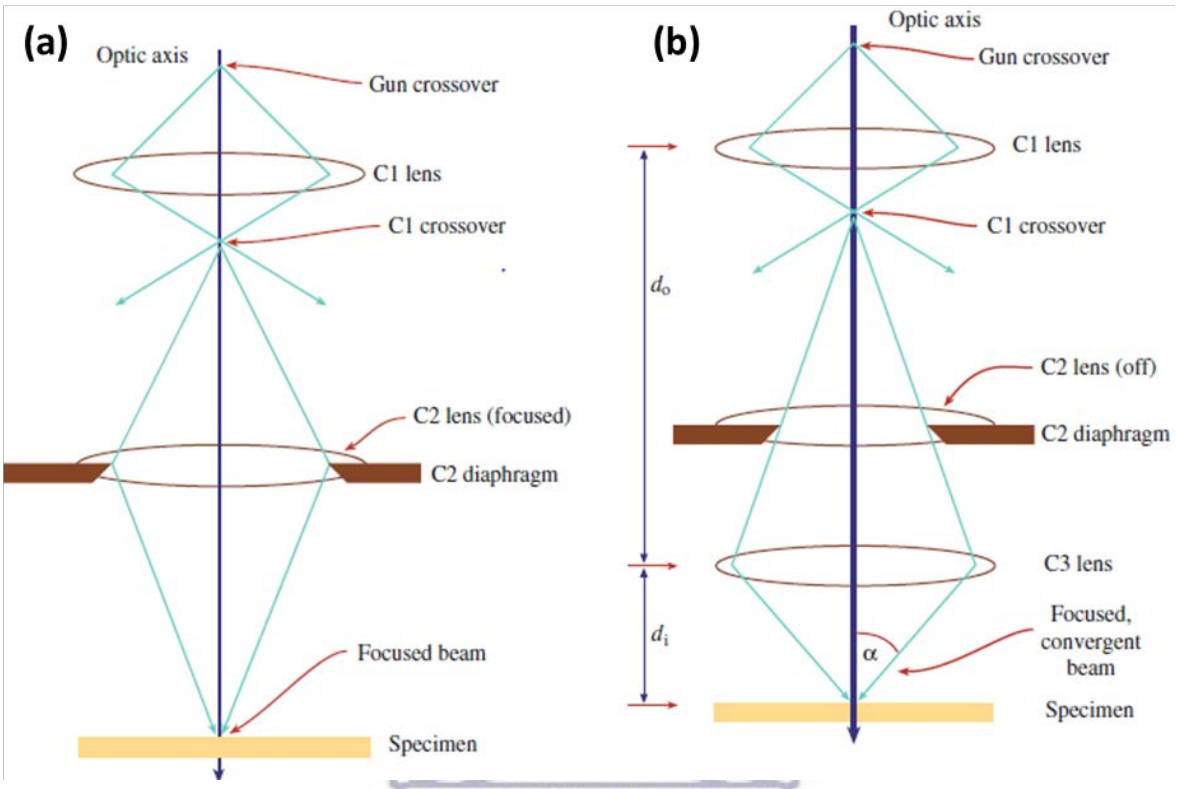

Figure 3.24: Ray diagrams illustrating the formation of convergent electron beam by (a) the focused condenser lens C2 and (b) upper pole-piece of the c/o lens in absence of C2 [3.11]

The presence of two or three scan coils, shown in figure 3.25, on both sides of the optical axis is essential for STEM as it provides raster scanning by deflection of the beam moving parallel to the optical axis. This provides material scientists with a tool to perform analytical techniques such as Z-contrast dark-field imaging and spectroscopic mapping by EDS and/or EELS.

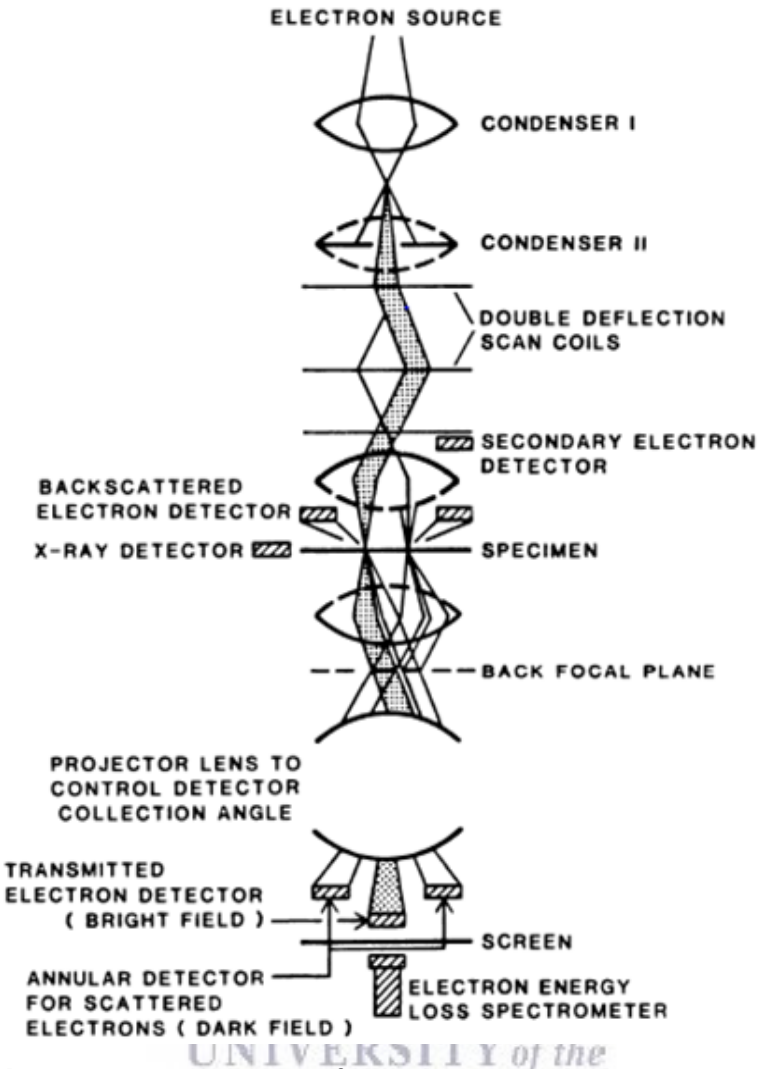

Figure 3.25: Schematic representation of the electron path during STEM operation [3.4]

3.7.2 Scanning Transmission Electron Microscopy: Bright and Dark Field Imaging

In section 3.4.2 it was mentioned that image formation in conventional TEM is achieved by placing/displacing an aperture to select a certain range of electrons to contribute to the formation, subsequently projected onto a display screen by a series of projector lenses. However, in STEM there are no post-lenses used to form the image, but rather a detection system used to collect signals which are then modulated and displayed as images on TEM display screens. This is advantageous since the resolution of the image formed is unaffected by lens aberrations which deteriorates the quality of the image [3.2]. For bright-field imaging in STEM, a scintillator detector is placed on the optical axis of the instrument as shown in figure 3.25 to collect all electrons scattered at relatively low angles with respect to the scan position on the specimen. Images and diffraction patterns formed this way are illustrated in figure 3.26

(b) with inset being the corresponding diffraction pattern. In the case of dark-field imaging, a high angular annular dark-field detector (HAADF) with circular opening at the centre is used to collect signals over a wide range of scattering angles, thereby producing Z-contrast images with dark background, as shown in figure 3.26 (a) [3.11].

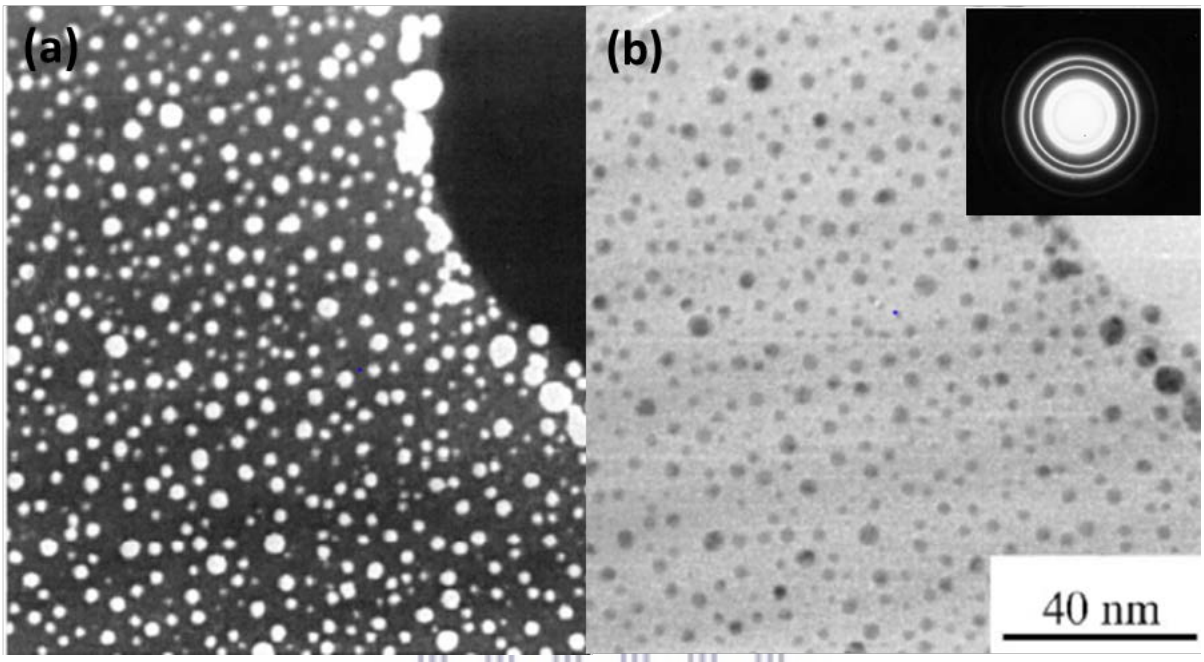

Figure 3.26: STEM (a) dark-field image and (b) bright-field images with inset of corresponding diffraction pattern [3.11]

3.7.3 Advanced Scanning Transmission Electron Microscopy Techniques

Since during STEM operation there are no post-lenses required below the specimen, there is a large space available for signal detectors and spectrometers. This enables multi-signal detection, such as x-ray detectors, backscattered and secondary electron detectors as shown in figure 3.25, placed around the specimen just as in SEM. This enables performance of EDS in the TEM instrument in the same way as it is performed in SEM. Moreover, when an energy loss spectrometer is placed below the specimen an EELS spectrum, which can be used as a complementary technique to the EDS, can be simultaneously recorded. However, the recording of EELS spectra in STEM is somehow different to the way the spectrum is collected in conventional TEM (CTEM). In section 3.5.2 it was mentioned that the electron beam entering

the spectrometer through the adjustable entrance aperture, as illustrated by figure 3.18, is dispersed and recorded parallel by magnetic prism and CCD arrays, respectively. In STEM, the recording is serial instead of parallel. Serial recording of EELS spectra require long acquisition periods, thus reducing the saturation of the detector. Major concern in serial recording is based on specimen and beam drift, which can result in difficulty during analysis [3.2-3.7, 3.11].

3.8 Sample Preparation

As a requirement for TEM investigations, the samples must be relatively thin to allow the transmission of the incident electrons. With that regard, a small drop (30 µl) of anhydrous ethanol (99.9 % purity) were dropped onto the TiO_2 nanotube substrate to soften the intact oxide film before it was scrapped of the Titanium foil using a razor blade. A holey-Carbon coated Copper grid was then placed on the TiO_2 nanotubes substrate to attach the film that contained nanotubes. The grids were then dried off using a 250 W Xenon lamp for five minutes prior to their use for TEM investigation. A modified TEM specimen sample holder was used to mount three samples at a time and was inserted into the side-column of the instrument for analysis. The TEM micrographs, SAED patterns, EDS, EELS and EFTEM data were all acquired using a Tecnai $G^2$20 FEG-TEM operated at accelerating potential of 200kV. EDS investigations were made possible by a retractable EDAX liquid nitrogen cooled Lithium doped Silicon, Si(Li), detector that is fitted within the instrument column, while EFTEM and EEL spectra were acquired using the post-column Gatan-Image filter, mounted at the bottom of the instrument is shown in figure 3.27(a). The instrument is hosted within the Electron Microscope Unit at the University of the Western Cape, South Africa. Other investigations such as STEM-EELS and bright-field imaging were performed using a Tecnai F30 Twin 300 kV FEG-TEM (shown in figure 3.27 (b)) hosted within the Electron Microscopy Core (EMC) of the University of Missouri-Columbia, Columbia USA. The instrument is equipped with a Gatan Ultra-scan 4000 CCD, Fischione HAADF detector for STEM imaging and a Gatan-image filter (GIF-Tridiem) with 2k x 2k CCD for EELS and EFTEM investigations.

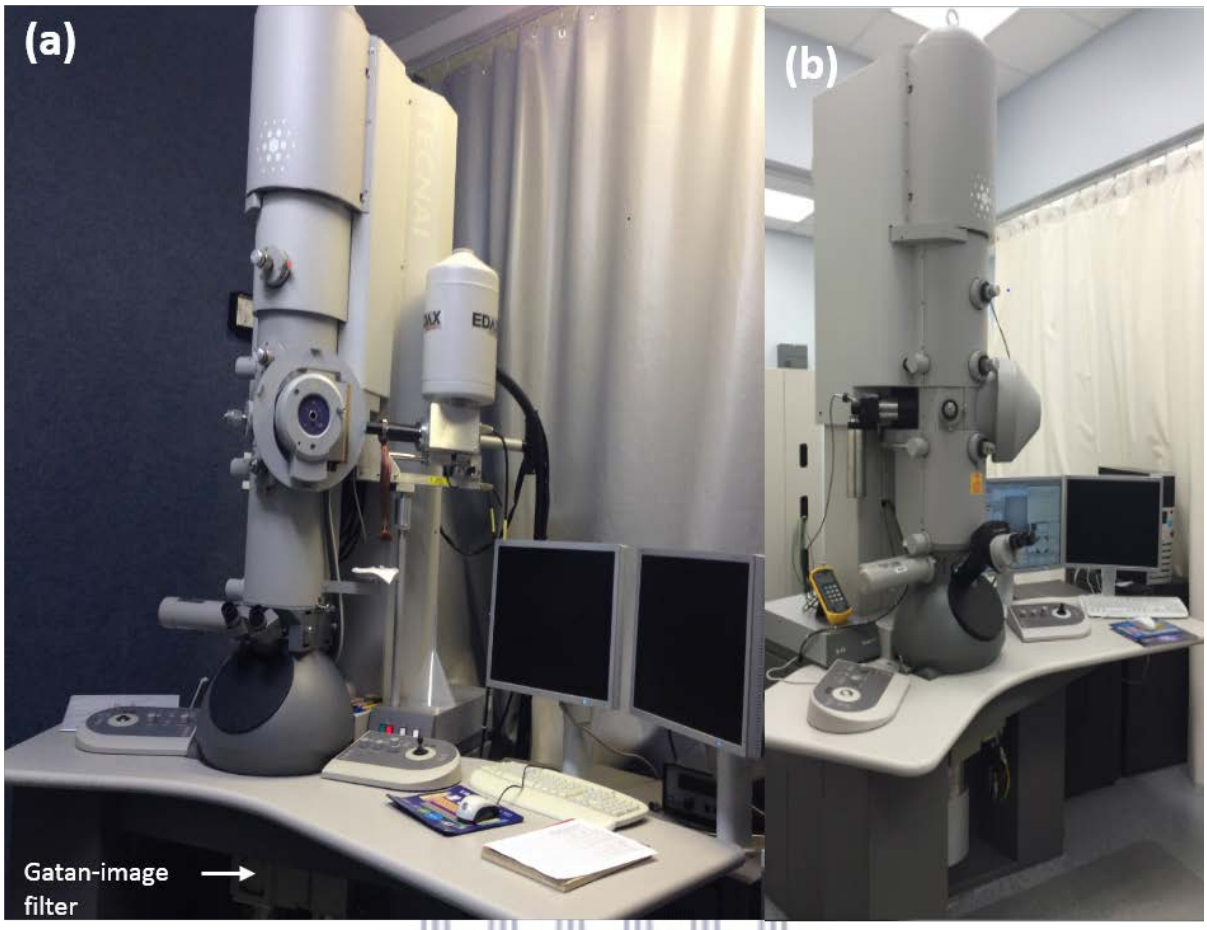

Figure 3.27: A pictorial representation of (a) Tecnai G^{2}20 200kV and (b) a Tecnai F30 Twin 300kV field-emission gun TEM

3.9 X-Ray Diffraction

3.9.1 Background

X-rays are highly energetic photons with wavelengths ranging from 0.5- 2.5 Å (Å = 10^{-10} m) which is much smaller compared to the wavelength of light, which is approximately 6000 Å. The discovery of X-rays dates back to 1895 when a German physicist Wilhelm Roentgen noticed a barium platinocyanide screen fluorescing in his laboratory while experimenting on cathode rays in a Crookes tube at the University of Wurzburg. At the time, the nature of these energetic rays was unknown; hence he named them "X-rays" with "X" being a widely used

variable in mathematics for unknowns. The high energy of X-rays enables them to penetrate through many materials which light could not. As a result of this high penetration ability, X-rays were immediately used by physicists to study internal structures of opaque objects without having any understanding about the nature of this radiation.

In 1912 Max Von Laue discovered the diffraction of X-rays by crystals while he was experimenting on the interference of X-rays passing through crystals. This discovery simultaneously proved the wave nature of X-rays. Diffraction of X-rays by crystals indirectly reveals details about fine structure in the order of 1 Å, which corresponds to the interplanar spacings of planes in a crystal. This provided metallurgical scientists with a new method of studying internal structures of matter. To date X-ray diffraction is one of the most widely used techniques in material science to study the materials' crystal structure and elemental composition [3.22-3.23].

3.9.2 Generation of X-rays

X-rays used in diffraction studies are generated when an electron from the outer shell fall into the inner-core vacancy caused by the excitation of inner-core electrons as consequence of their interaction with the primary electrons of sufficient ionising energy (Also discussed in section 3.3.4). Coupled in a typical X-ray diffractometer as main source of x-rays is the *X-ray tube,* which consists of three components namely; (a) electron source, (b) accelerating voltage, and (c) a target material with water cooling system around it [3.22]. The schematic of an X-ray tube is shown in figure 3.28 below:

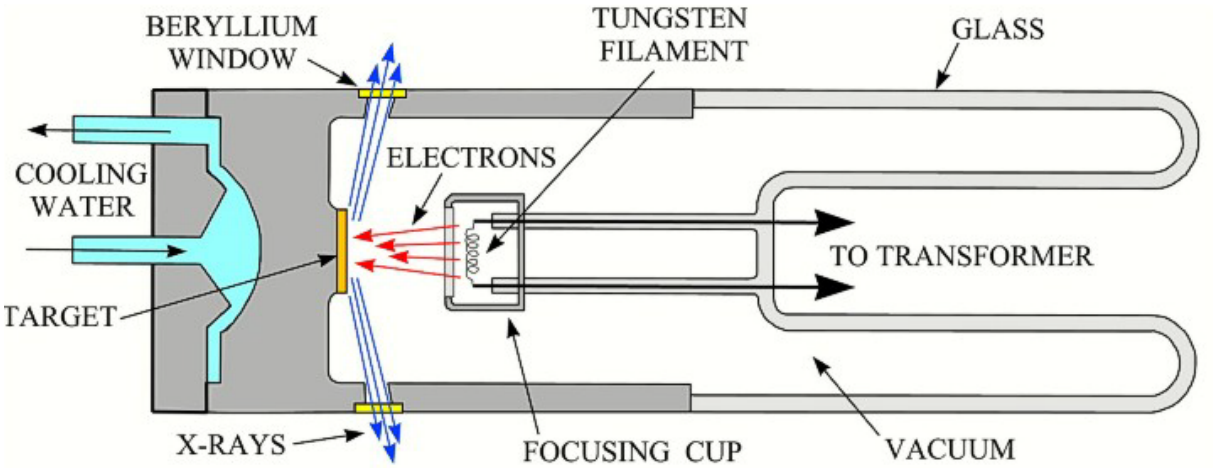

Figure 3.28: Schematic cross-section of a filament X-ray tube [3.25]

Ideally all X-ray tubes (i.e. gas and filament tubes) consist of two electrodes with the anode being the target material. Copper (Cu) is the most commonly used anode target with a W filament the corresponding cathode. The presence of the evacuated glass around the tube is to insulate the electrodes and maintain good vacuum inside the tube. When the filament is heated up by applying a current via the transformer, electrons are liberated from the W-filament, forming an electron cloud inside the focusing cup, which is held at negative biased potential, ranging from 30 – 50 kV for diffraction studies, while the target is grounded. Because of the existing potential difference between the anode and the cathode, electrons are repelled from the negatively biased cathode and accelerate towards the target material (Cu) with focusing towards a narrow spot, called the *focal spot* on the target material. Upon impact of the electrons with the target material, X-rays are generated and radiate in all directions, as shown in figure 3.28. They escape the tube through X-ray transparent beryllium (Be) windows (typical tube consists of two windows). The generated X-ray beam, however, consists of a variety of wavelengths as it may have contributions from other transitions, such as K_α and K_β. As part of the requirements for diffraction studies, the beam of X-rays must be monochromatic; thus, filters such as Nickel (Ni), Zirconium (Zr), Iron (Fe) and graphite are used to reduce the contribution of the unwanted transitions [3.22].

3.9.3 Crystal Structure

A crystal is defined as a solid that is composed of atoms arranged in three-dimensional periodic arrangement. Materials with such periodicity are said to be crystalline materials while other

materials such as glass, which does not possess the periodicity, are said to amorphous. In a crystalline material, the arrangement of atoms or molecules, known as lattice points, defines the crystal structure (also referred to as point lattice) of the material; shown in figure 3.29 (a).

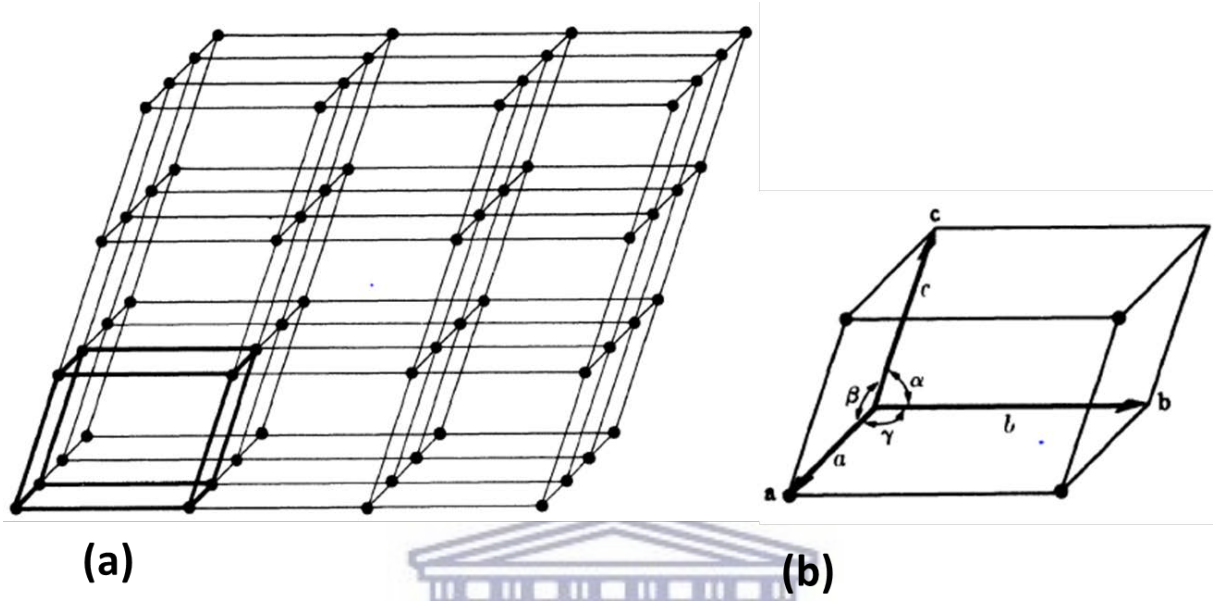

Figure 3.29: Schematic of (a) point lattice and (b) a unit cell [3.22]

In the above point lattice, the arrangement of lattice points is such that they have identical surroundings, in other words, when the point lattice is viewed from a particular lattice point, it would have exactly the same appearance when viewed from another lattice point, provided they are in the same direction. Since the point lattice cells are all identical, any cell in the lattice is considered to be the unit cell; shown in figure 3.29 (b). The shape and size of the unit cell is described by three translational vectors, also known as crystallographic axes $\vec{a}$, $\vec{b}$ and $\vec{c}$, which in turn can be described in terms of their magnitudes *(a, b, c)* and the angles between them (α, β, γ). These crystallographic defining parameters are known as lattice parameters or lattice constants. Variation in lattice parameters consequently results in a deformed unit cell; in terms of size and shape, thus defining a new unit cell. As for such variations, fourteen types point lattice, known as Bravais lattices, exist and are divided into seven space groups, or crystal systems, according to their axial relations. Table 3.1 below provides the description of the fourteen Bravais lattices according to their space groups.

Furthermore, the translational vectors defining a unit cell can be used to describe any point in the lattice by considering the linear combination of crystallographic axes as shown in equation below.

Table 3.1: Description of fourteen Bravais lattice with their crystal systems [3.22]

System	Axial length and Angles	Bravais lattice	Lattice symbol
Cubic	3 equal axis at right angles $a = b = c$, $\alpha = \beta = \gamma = 90°$	Simple Body-centred Face-centred	P I F
Tetragonal	3 axis at right angle, 2 equal $a = b \neq c$, $\alpha = \beta = \gamma = 90°$	Simple Body-centred	P I
Orthorhombic	3 un-equal axis at right angles $a \neq b \neq c$, $\alpha = \beta = \gamma = 90°$	Simple Body-centred Base-centred Face-centred	P I C F
Rhombohedral (Trigonal)	3 equal axes, equally inclined $a = b = c$, $\alpha = \beta = \gamma \neq 90°$	Simple	P
Hexagonal	2 equal co-planar axes at 120°, 3rd axis at right angles $a = b \neq c$, $\alpha = \beta = 90°$, $\gamma = 120°$	Simple	P
Monoclinic	3 unequal axes, one pair not at right angles $a \neq b \neq c$, $\alpha = \gamma = 90° \neq \beta$	Simple Base-centred	P C
Triclinic	3 unequal axes, unequally inclined and none at right angles $a \neq b \neq c$, $\alpha \neq \beta \neq \gamma \neq 90°$	Simple	P

$$\vec{\mathbf{r}} = u\,\vec{\mathbf{a}} + v\,\vec{\mathbf{b}} + w\vec{\mathbf{c}} \tag{3.15}$$

where *u, v* and *w* are the smallest integer numbers describing the co-ordinates; denoted by [*u, v, w*] of any vector in the point lattice represented by $\vec{r}$. For example, consider the coordinates $(1\ \frac{1}{2}\ 0)$ shown in figure 3.30, the preferred representation of crystallographic direction of the coordinates would be [2, 1, 0] with negative direction being denoted by a bar index. Hence the

[*u, v, w*] are known as the indices of direction and are used to represent any line that is parallel to a given combination of indices. Furthermore, the direction related by symmetry are called the directions of form and denoted by **<*u w v*>.** For example, the $[1\bar{1}1]$, $[11\bar{1}]$, $[\bar{1}\bar{1}1]$, and $[\bar{1}11]$ may all be represented by <111>.

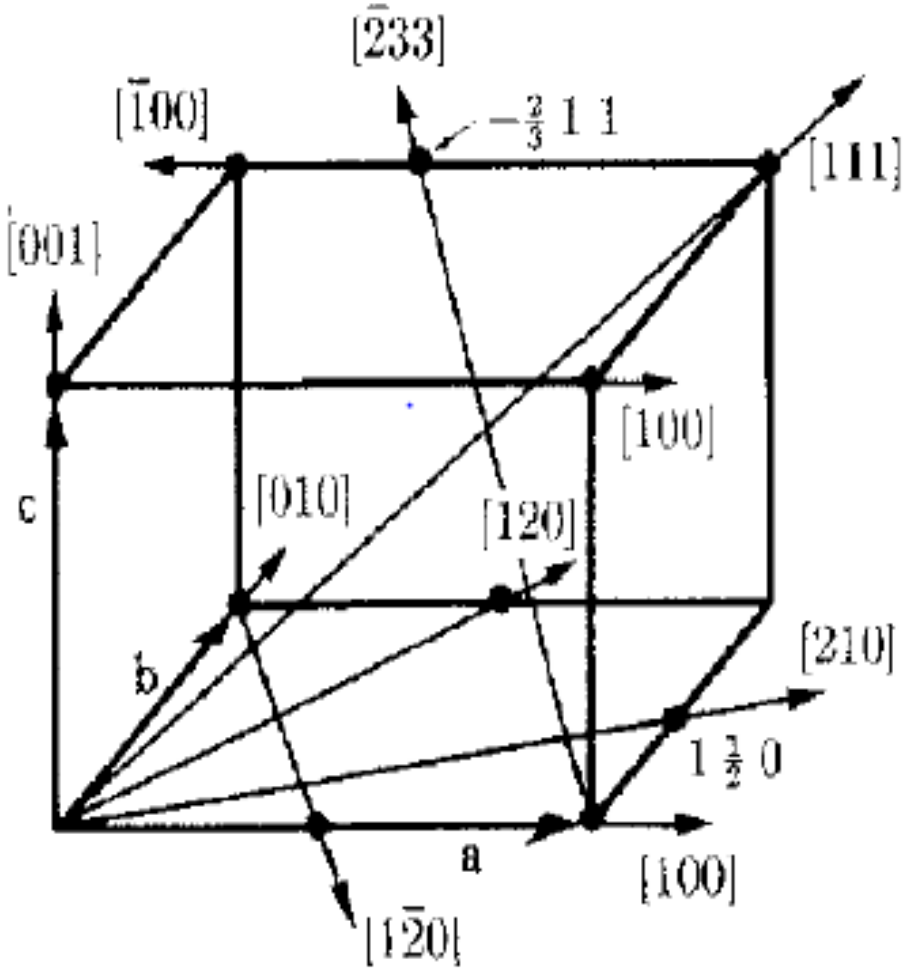

Figure 3.30: Schematic of cubic system showing indices of directions [3.22]

The orientation of planes in crystal lattice is symbolically represented in terms of its Miller indices (*h k l)* which are of important significance in diffraction studies. Planes related by symmetry are called planes of form and are denoted by {*h k l*}. Such planes have same interplanar d-spacing but different indices. For example, the faces of a cube (100), (010), (001), $(\bar{1}00)$, $(0\bar{1}0)$ and $(00\bar{1})$ are planes of the form {100}. However, if the Miller indices of a plane (*nh nk nl*) where "*n*" is any number in real-space, which is the multiple of (*h k* l), the interplanar d- spacing of such planes is given as fraction of the common factor "*n"* multiplied by the d-spacing of (*h k l*) plane.

3.9.4 Bragg's Law of X-ray Diffraction by Crystals

When a monochromatic, parallel X-ray beam strikes the surface of a crystal with stacked (*hkl*) planes and interplanar d-spacing, *d*, at glancing angle θ_B, as shown in figure 3.31, the incident beam interacts with the atoms of the crystal resulting in reflection and/or sometimes transmittance of the beam. Of interest in diffraction studies are the reflected x-rays which may coherently combine, forming a diffracted beam if and only if their path differences are an integer multiple of the wavelength of the x-ray beam, i.e.:

$$\mathrm{CA} + \mathrm{AD} = \mathrm{n}\lambda \tag{3.16}$$

Where n is an integer multiple (order of diffraction), λ the wavelength of the X-ray beam and the arc $CA = AD = d\sin(\theta_B)$ are the path differences of the reflected beams. Equation 3.16 can be simplified to

$$2\mathrm{d}\sin(\theta_\mathrm{B}) = \mathrm{n}\lambda \tag{3.17}$$

The resulting equation (3.17) is known as *Bragg's Law of X-ray diffraction*. This relation gives the angle θ_B at which a set of (*hkl*) planes with unknown interplanar d-spacing coherently diffracts the incident beam in the n^{th} order. The unknown d-spacing can be directly obtained from Bragg's law provided that the order of diffraction, n, and the X-ray beam wavelength, λ, are known. The obtained value for *d* is used to calculate the lattice parameters *a*, *b* and *c* of tetragonal systems using the following expression:

$$\frac{1}{d^2{}_{hkl}} = \frac{h^2+k^2}{a^2} + \frac{l^2}{c^2} \tag{3.18}$$

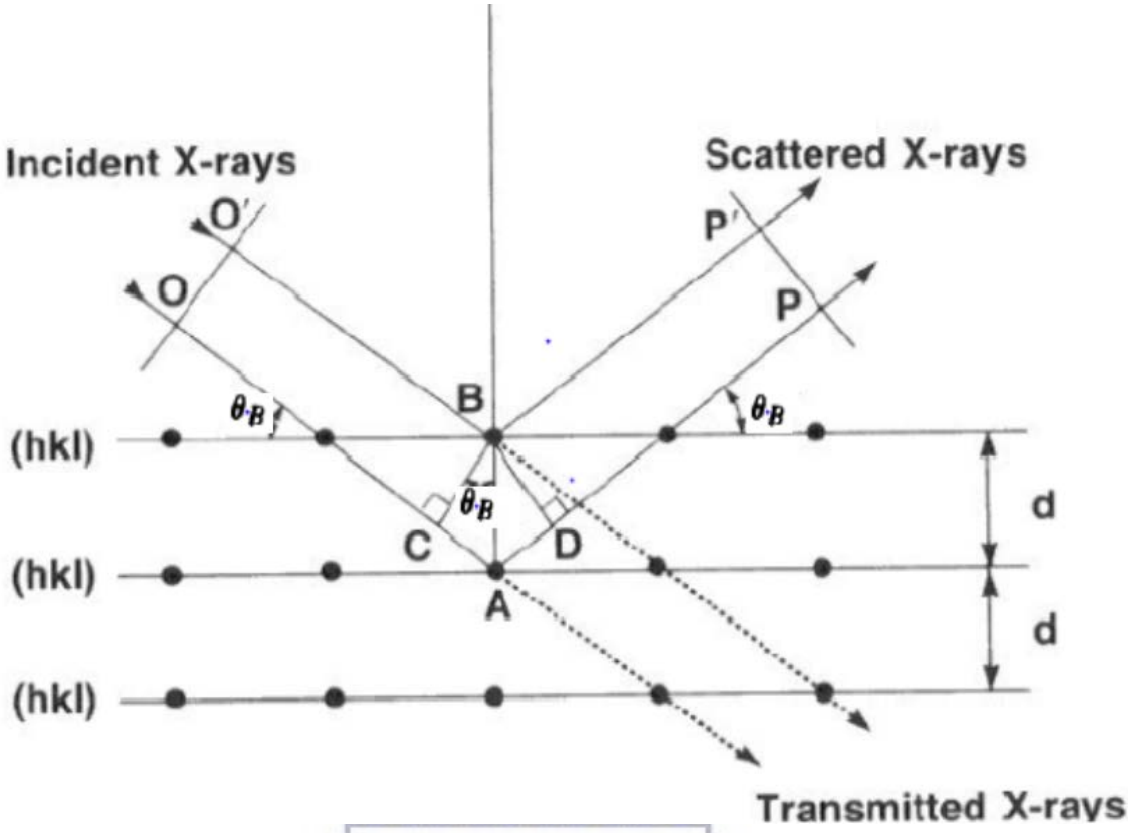

Figure 3.31: Schematic representation of X-ray diffraction by perfect crystal according to Bragg's Law [3.22]

3.9.5 Scherrer Formulation for the Determination of Crystallite Sizes

An important analytical tool of XRD is the ability to determine the crystal size of small crystallites, by analysing the width and intensity of a diffracted x-ray peak. Bragg's law of (3.17) is based on the assumption that the incident-ray beam is composed of perfectly monochromatic and parallel radiation, which is rarely the case in reality. Suppose that the crystal has a thickness, t, measured in a direction perpendicular to a particular set of reflecting planes and have (m + 1) planes as shown in figure 3.32 below.

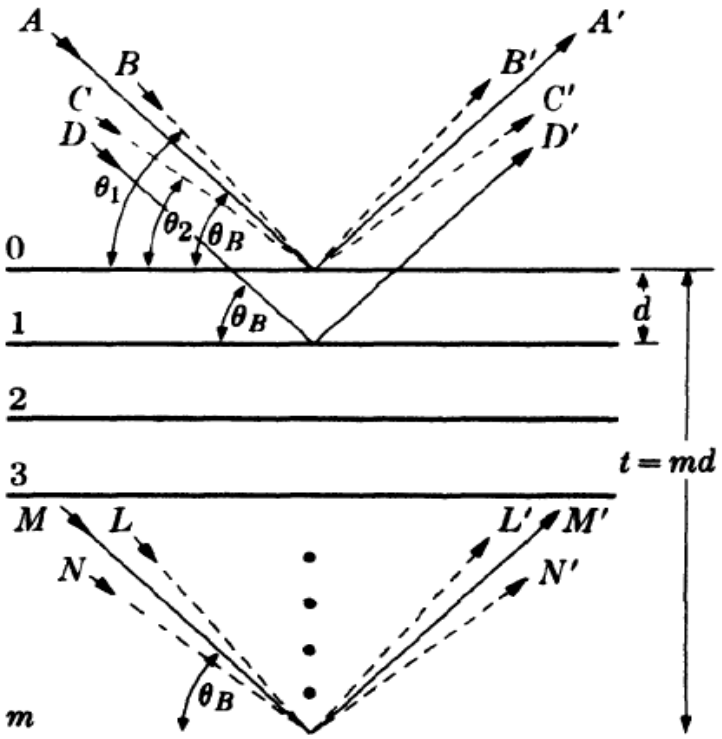

Figure 3.32: Effects of crystal size on diffraction [3.22]

When rays **A**, **D**,..., **M** are incident at angle θ_B to the reflecting planes of the crystal, the scattering of the incident rays by the crystal planes occurs, with ray **D'** resulting from the scattering of ray **D** by the first plane below the surface. This implies that ray **D**' is one wavelength out of phase with ray A' and that ray M' that is scattered by the m^{th} plane below the surface is m wavelengths out of phase with A'. Therefore, at diffraction angle $2\theta B$, rays A', D',..., M' are completely in phase and interfere constructively to form a diffraction of maximum amplitude, i.e. a beam of maximum intensity, since the intensity is proportional to the square of the amplitude.

However, when one considers incident x-rays at slightly different angles from θ_B, it is found that destructive interference is not complete. For example, ray **B** makes a slightly larger angle θ_1, such that ray **L'** that is scattered by the m^{th} plane below the surface is (m + 1) wavelengths out of phase with **B'**. This implies that midway in the crystal there is a plane that scatters a ray which is half a wavelength out of phase with ray **B'**. Subsequently, these planes cancel each other out and so do the other rays from similar pairs of planes throughout the crystal. The net

effect is that, rays scattered by the top half of the crystal annul those scattered by the bottom half. The intensity of the beam diffracted at an angle $2\theta_1$ is therefore zero. It is also zero at an angle $2\theta_2$ where θ_2 is such that ray N' scattered by the m^{th} plane below the surface is (m – 1) wavelengths out of phase with ray C' from the surface plane.

It follows that the diffracted intensity at angles near $2\theta_B$, but not greater than $2\theta_1$ or less than $2\theta_2$ is not zero, but has an intermediate value between zero and the maximum intensity of the beam diffracted at an angle $2\theta_B$. Figure 3.33 illustrates this relationship between the diffracted intensity and $2\theta_B$, and compares it to the ideal diffraction condition implied by Bragg's law.

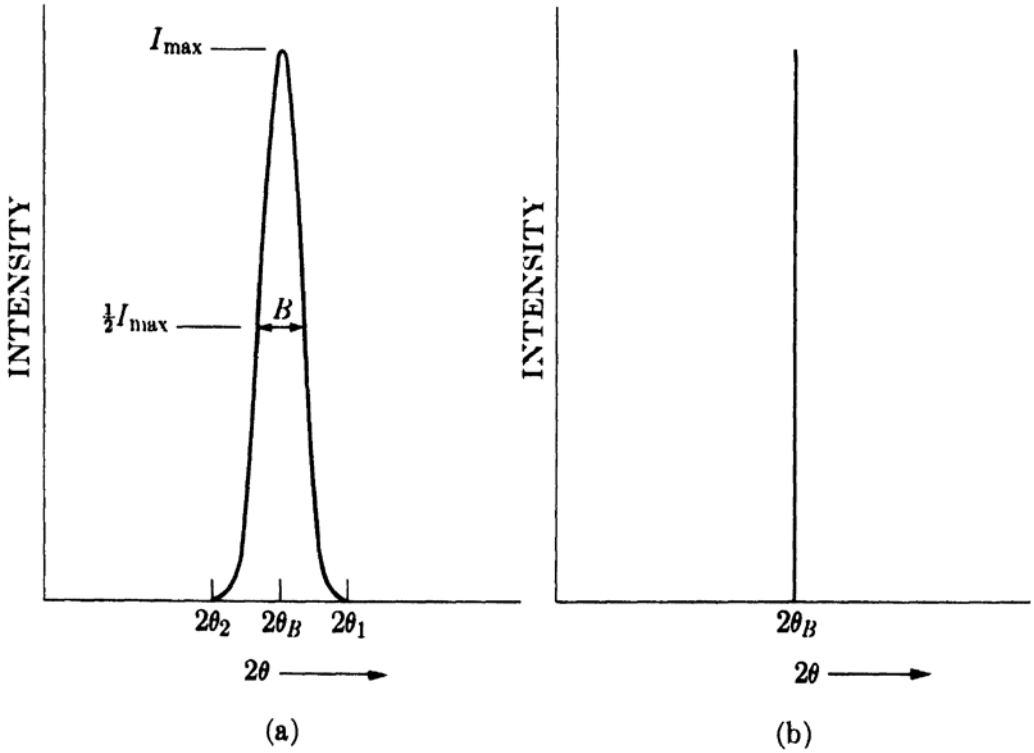

Figure 3.33: Effect of crystal size on the diffraction curve under (a) real conditions and (b) ideal Bragg conditions [3.22]

The width of the diffraction curve of figure 3.33 (a) increases as the thickness of the crystal decreases. The width B is usually measured in radians, at an intensity equal to half the maximum intensity. As a rough measure of B, one can take half the difference between the two extreme angles at which the intensity is zero, i.e.:

$$B = \frac{1}{2}(2\theta_1 - 2\theta_2) = \theta_1 - \theta_2 \quad (3.19)$$

The path difference requirements from Bragg's law for these two angles implies that

$$2t\sin(\theta_1) = (m+1)\lambda \quad (3.20)$$

$$2t\,Sin(\theta_2) = (m-1)\lambda \quad (3.21)$$

Subtracting (3.21) from (3.20) gives

$$t(\sin(\theta_1 - \sin(\theta_2) = \lambda \quad (3.22)$$

which can be rewritten to (3.23) when trigonometric identities are used.

$$2t\cos\left(\frac{\theta_1+\theta_2}{2}\right)\sin(\frac{\theta_1-\theta_2}{2}) = \lambda \quad (3.23)$$

However, θ_1 and θ_2 are both very close to θ_B, and that implies that $\theta_1 + \theta_2 = 2\theta_B$. So, by small angle approximation, $\sin\left(\frac{\theta_1-\theta_2}{2}\right) = \frac{\theta_1-\theta_2}{2}$ and this implies that (3.23) can be rewritten to

$$2t\left(\frac{\theta_1-\theta_2}{2}\right)\cos(\theta_B) = \lambda \quad (3.24)$$

where $\beta_{obs} = \frac{\theta_1-\theta_2}{2}$ is the observed full-width half maximum intensity of the diffraction curve measured in radians. Note, thus far, the formulation of Scherrer equation assumes that observed peak broadening is only due to the crystallite size. In fact, that is not the case. An observed broadening of the diffraction peak consists of both the instrumental broadening (β_{instr}) and the crystallite size broadening (β_{Size}). To decouple these contributions, it is necessary to collect diffraction pattern from a line broadening of a known standard material such as silicon. When assuming a Lorentzian shape of the diffraction peak, the size broadening can be computed as

$$\beta_{size} = \{\beta_{obs} - \beta_{inst}\} \quad (3.25)$$

Combining (3.24) and (3.25) results in the well know Scherrer formula (3.26) that is used to determine the crystallite size,

$$t = \frac{k\lambda}{\beta_{size}\cos(\theta_B)} \quad 3.26)$$

where t is the crystallite size, *k* the shape constant normally assumed to be 1, and λ the wavelength of the Cu K_α radiation [3.22].

3.9.6 Williamson-Hall Analysis for the Determination of Crystal Size and Strain

Following Scherrer's famous equation (3.26), Stokes and Wilson observed that the strained or imperfect crystals contains line broadening of a different sort to that of crystallite size and that the strain-related broadening is given by

$$\varepsilon_{str} = \frac{\beta_{str}}{4\tan(\theta_B)} \quad (3.27)$$

where ε_{str} is the average strain and β_{str} strain related broadening (measured in radians 2θ). Again, for accurate determination of the crystallite size and strain, one must account for the line broadening contributions. In Lorentzian shape

$$\{\beta_{obs-}\beta_{inst}\} = \beta_{size+}\beta_{str} \quad (3.28)$$

In 1953, Williamson and Hall proposed a method of deconvoluting the size and strain by looking at the peak width as function of 2θ. Substituting (3.26) and (3.27) it can be deduced that:

$$\{\beta_{obs-}\beta_{inst}\} = \frac{k\lambda}{t\cos(\theta_B)} + 4\varepsilon_{str}\tan(\theta_B) \quad (3.29)$$

Rearranging (3.29), results (3.30):

$$\{\beta_{obs-}\beta_{inst}\}\cos(\theta_B) = \frac{k\lambda}{t} + 4\varepsilon_{str}\sin(\theta_B) \quad (3.30)$$

Equation (3.30) is known as Williamson and Halls simplified integral breadths method that is used to determine the crystallite size and strain from the y-intercept and the slope of the straight-line fit to the obtained data points. To obtain a Williamson-Hall plot, one should plot cos (θ_B) in the y-axis and 4sin (θ_B) on the x-axis [3.23-3.24]. The intercept with y, i.e. when x = 4sin (θ_B) = 0, yields the crystallite size according to:

$$\tau = \frac{k\pi}{y(x=0)} \tag{3.31}$$

whereas the slope of the linear fit yields the lattice strain, ε_{str} , within the film of nanotubes.

3.9.7 The X-Ray Diffractometer

An X-ray diffractometer is an instrument that is used to measure the intensity of the diffracted x-ray beam by means of electronic counter [3.20]. This instrument consists of three basic components namely; (a) an x-ray source positioned at (S and T), (b) the diffractometer circle centred at sample stage at C supported by H, and (c) the detector system situated on the circumference of the circle at position G. The three basic components orientation of these components is illustrated on the schematic below.

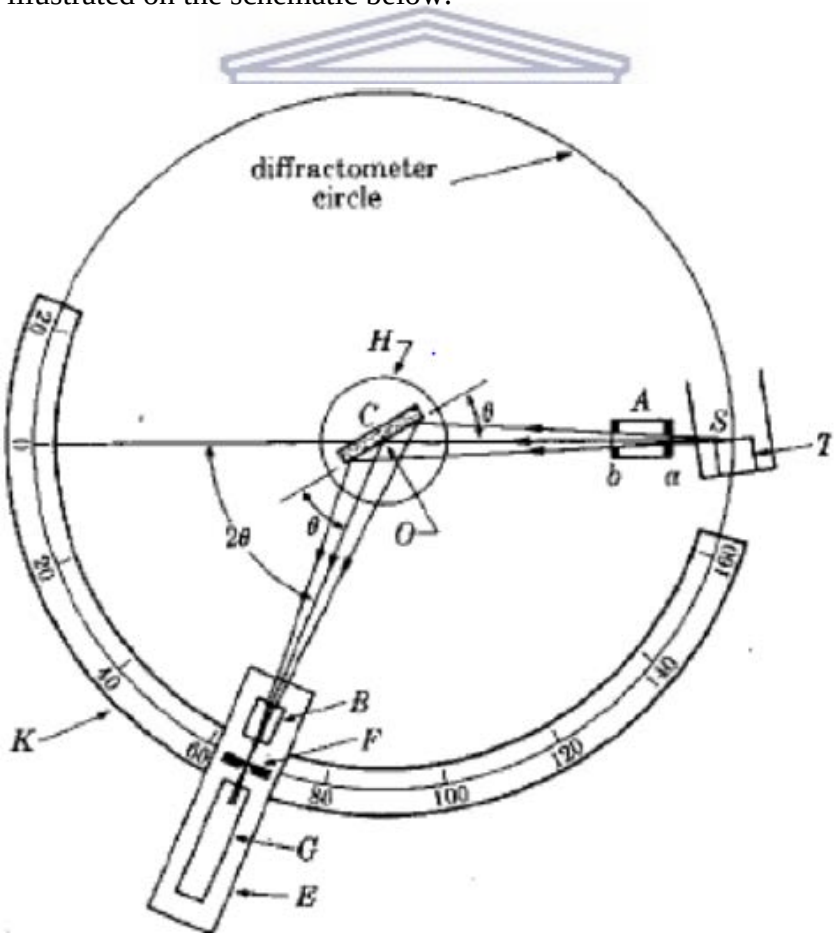

Figure 3.34: Schematic representations of the three basic components of x-ray diffractometer and its operation principle [3.20]

Originating from the x-ray source at S, the incident beam passes through the defining slit labelled “A” and diverges towards the sample mounted at C inside support H. The support rotates the sample about an axis O which is perpendicular to the page at angle θ. Upon impingement of the sample with the beam, the atoms of the sample interact with the beam resulting in diffracted x-ray beam which is collimated at slit B. Following the collimator slit, the beam is converged to a focal spot on slit F before being detected at G which supported by E. The support E also rotates about axis O and has angular angle 2θ. Moreover, the supports E and H are mechanically coupled in such a way that a rotation of the detector through 2θ is simultaneously accompanied by rotation of sample through θ. This mechanical coupling permits the conservation of the focussing conditions [3.20].

References

[3.1] T. M. Poster, S. K. Howard, A. H Johnson and K. L. McMichael, 2001, "Scanning Electron Microscope", Ladd Research Industries. United States of America

[3.2] P. J. Goodhew, J. Humphreys and R. Beanland, 2001, "Electron Microscopy and Analysis" Taylor & Francis, London and New York

[3.3] D. E. Newbury (auth.), David C. Joy, Alton D. Romig Jr., Joseph I. Goldstein (eds.). 1986, "Principles of Analytical Electron Microscopy 3rd Edition", Springer, United States of America

[3.4] D. E. Newbury (auth.), David C. Joy, Alton D. Romig Jr., Joseph I. Goldstein (eds.), 1979. "Principles of Analytical Electron Microscopy 2nd Edition", Springer, United States of America

[3.5] N Yao and Z. L Whang (eds),2005, "Handbook of Microscopy for Nanotechnology", Kluwer Academic Publishers. London

[3.6] R. F Egerton, 2005, "Physical principles of Electron microscopy", Springer + Business Media Inc, New York.

[3.7] S. Wischnitzer, 1970, "Introduction to Electron Microscope, 2nd Edition" Pergamon Press Inc. United States of America

[3.8] L. Reimer and H. Kohl, 2008, "Transmission Electron Microscope- Physics of Image Formation, 5th Edition", Springer & Business Media Incl. New York

[3.9] I. Watt, 1997, "The principles and Practice of Electron Microscopy", Cambridge University Press. Great Britain

[3.10] J. Goldstein, D. Newbury, P. Echlin, D. Joy, C, Fiori and E. Lifshin, 1981, "Scanning Electron Microscopy and X-ray Microanalysis", Plenum Press, New York

[3.11] D. B. Williams and B. C. Carter, 2009, "Transmission Electron Microscopy- A textbook for material science", Springer Science + Business Media LLC, United States of America

[3.12] J Palisaitis, 2012, "Valence electron energy loss spectroscopy of III-Nitrate of Semiconductors", Linkoping University, Sweden

[3.13] R. F. Egerton, 1996, "Electron Energy-Loss Spectroscopy in the Electron Microscope". Springer, United States of America

[3.14] K Jorissen, 2007, "The improvement of calculations of Electron energy loss spectroscopy", University Antwerpen, Netherlands (Unpublished PhD thesis)

[3.15] C.C. Ahn (ed), 2004, "Transmission electron energy loss spectrometry in Material science and the EELS atlas, 2nd Edition" Wiley-VCH, California, United States of America

[3.16] R. Brydson. J. Phys.Condens. Matter 1 (1989) 797

[3.17] R Brydson J. Phys.Condens. Matter 4 (1994) 3429

[3.18] S.O Kucheyev, T. Van Buuren, T.F Satcher Jr., T. M Willey, R. W. Meulenberg, T. E Felter, J. F Poco, S. A Gammon, L. J Terminello, Physical Review B. UCRL-JRNL-202402

[3.19] L. A Grune, R. D Leapman, Physical Review Letters 45 (1980) 5

[3.20] N, Grogger, M. Varela, R, Ristau, B. Schaffer and K. M. Krishnan. Journal of Electron Spectroscopy and Related Phenomena 143 (2005) 139

[3.21] J. Verbeeck, D. Van Dyck, and G. Van Tendelo. Spectrochimica. Acta Part B 59 (2004) 1529

[3.22] B. Cullity, 1978, "Elements of X-ray diffraction", Addison-Wesley Publishing Company, United States of America

[3.23] P.P Ewald, 1962, “Fifty years of X-ray diffraction”, International Union of Crystallography, Netherlands

[3.24] G. K. Williamson and W. H. Hall. Acta Metall. 1 (1953) 22

[3.25] L.J. Poppe, V.F. Paskevich, J.C. Hathaway, and D.S. Blackwood, 2001,“A Laboratory for X-Ray Powder Diffraction” Retrieved from: https://pubs.usgs.gov/of/2001/of01-041/index.htm

CHAPTER FOUR

Results and Discussions

4.1 Introduction

This chapter will present the results of the TiO_2 nanotubes synthesised in various electrolyte regimes via the anodisation technique, as discussed in chapter two. To understand the effect of the electrolyte composition on the resulting morphology of TiO_2 nanotubes, the current-time transient curves were recorded. Scanning electron microscopy studies were conducted to investigate the structural features such as pore-diameter, wall-thickness, length and the overall distribution of nanotubes across the sample by collecting top and cross-sectional micrographs. Transmission electron microscopy was used to investigate elemental composition by means of EDS and the structure of individual TiO_2 nanotubes by means of various imaging methods (discussed in chapter three). As mentioned in chapter one, prior to the use of TiO_2 nanotubes in technological and/or biological applications, it is crucial to understand the material's localised properties such as the crystal and electronic properties as they are believed to heavily influence the opto-electronic performance of the material. Thus, TEM operated in diffraction (SAED) mode and an XRD were used to probe the crystal structure of bulk and single TiO_2 nanotube(s) respectively. Moreover, the XRD data was used to determine the crystal size using the Scherrer and Williamson-Hall formulation, discussed and derived in chapter three. Electron energy loss spectroscopy and scanning transmission electron microscopy coupled EELS (STEM-EELS) were used to probe for the fine structure of single TiO_2 nanotubes together with the crystallographic transformation along the tube length respectively. Jump ratio mapping, combined with valence EELS were then conducted to provide visual evidence of the evolution of the localised TiO_2 crystallinity along the nanotube structure. The techniques are also complementary to those used to probe for the crystal structure of TiO_2 nanotubes.

The chapter will be summarised and conclusions made based on the results obtained on all analytical techniques. The experimental conditions for the synthesis of TiO_2 nanotubes and operational conditions of analytical techniques will not be mentioned into detail as they were rendered in chapter two and three respectively.

4.2 Morphology

4.2.1 Effect of the Electrolyte Composition

Figure 4.1 compares top- and cross-sectional SEM micrographs of TiO_2 nanotubes synthesised in the various electrolyte regimes described in chapter two. From the top-view images, the average nanotube diameter and wall-thicknesses were determined, whereas the cross-sectional images allowed for measurement of the nanotube lengths. It must be noted that the SEM micrographs show a presence of unwanted debris, commonly known as the remnant oxide layer formed during the anodisation process; the images also reveal, that the formed nanotubes have opened tops and closed bottoms. Similar results have been observed by various authors, for example [4.1, 4.2]. A further note, the side view images were obtained by polishing the Ti/TiO_2 nanotube samples using a 100 nm fine diamond lapping paper; this approach did not always yield positive results, however, and in some instances, the as-synthesised Ti film was bend to expose the vertically aligned film of nanotubes perpendicular to the electron beam when performing SEM. The remnant oxide layer is commonly removed by heat treatment or chemical etching using chloric acids prior to application in the various devices, e.g. photocatalytic experiments or DSCs. In this study, however, this approach was not followed as the study is aimed at investigating the growth of the nanotube structures, and any post treatment of the specimens following these processing methods may compromise the data collected from the characterisation techniques.

The dimensions of the nanotube diameter, wall thickness and lengths are summarised in Table 4.1. As shown, anodisation of the Ti foil in neutral, organic electrolytes (i.e. regime 3, consisting of 0.14 M (1 vol%) NH_4F + 97 vol% PEG + 2 vol% H_2O) at longer anodisation durations yields nanotubes with high aspect ratios compared to those obtained when using an acidic (regime 1, 0.14 M (0.5 vol%) NaF + 0.5 M (2.5 vol%) H_3PO_4 + 97 vol% H_2O) and neutral (regime 2, 1 M (3 vol% NaF + 2 vol% H_2O + 95 vol% glycerol). This is ascribed to the constant growth of nanotubes due to the reduced diffusion rate of fluoride ions by highly viscous PEG electrolyte. Also, the increase in anodisation duration and voltage play a major role in this morphological change since longer synthesis periods allow for the formation thicker oxide layers, which is in turn, continuously etch the resulting pits (discussed in chapter two) into longer nanotubes.

However, even though it is a known fact that organic electrolytes with reduced water content below 5% yield nanotubes of greater lengths, the nanotubes synthesised in regime 2 have the shortest length compared to the other two regimes. This may be ascribed to a rather lower donation of O^{2-} species in organic electrolytes as a consequence of reduced water content, which results in growth of thinner oxide layer through which the ionic transport is enhanced. Furthermore, the incorporation of organic components from the electrolyte into the oxide film reduces the permittivity of the oxide layer and increases its dielectric breakdown potential [4.11]. As such, the use of a high anodisation potential of 60 V and high concentration of fluoride (F^-) ions to synthesis regime 2 samples, enhances the inward transport of F^- ions which ultimately, due to their small radii compared to O^{2-} ions, compete with oxygen species (as mentioned in chapter 2), thereby enhancing the chemical dissolution of the formed oxide layer (2.4). In addition, since it also a known fact that anodisation in organic electrolytes required longer anodisation duration to achieve longer nanotubes, the use of 4 hours duration in synthesis of regime 2 samples may have been another restricting factor to achieving longer nanotubes.

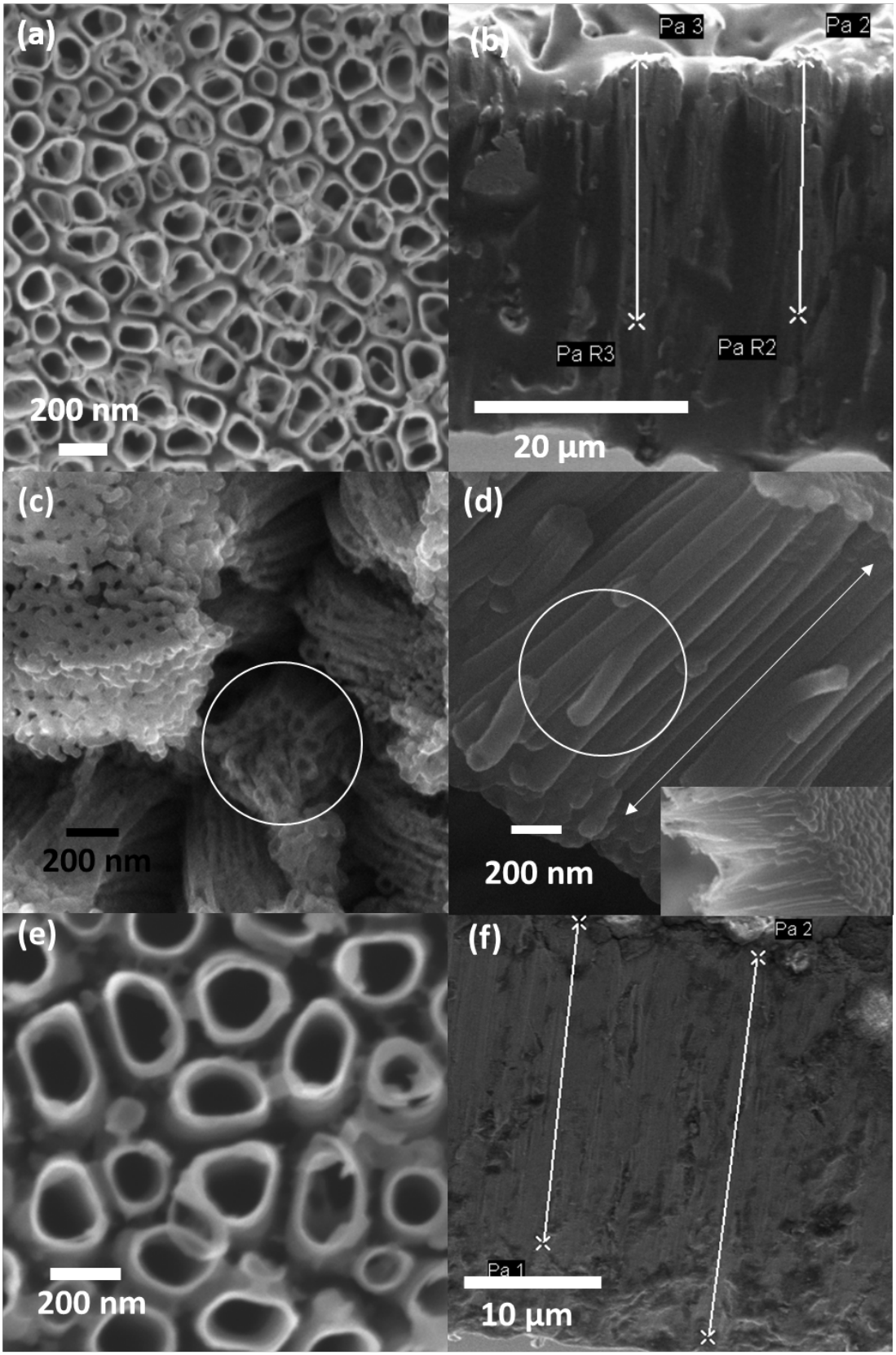

Figure 4.1: Top and cross-sectional SEM micrographs of (a)-(b) regime 1, (c)-(d) regime 2 and (e)-(f) regime 3 electrolytes with inset in (f) revealing the closed bottom nature of TiO2 nanotubes.

Table 4.1: Dimensions of the resulting morphologies of TiO_2 nanotubes for all three electrolyte regimes

Regime	Pore-Diameter (nm)	Wall-Thickness (nm)	Length (µm)
1	150	23	26
2	58	36	1.9
3	200	29	39

At closer inspection of figure 4.1, it is apparent that TiO_2 nanotubes synthesised in regime 2 (figure 4.1 (d)) have smooth side-walls, while those of regime 1 and 3 are not clearly observed as a result of polishing method used prior to imaging. However, Cummings et. al [4.3] reported that TiO_2 nanotubes synthesised via acidic electrolytes yielded nanotubes with rippled side-walls whereas organic electrolytes yield generally smoother side-walls. The observed ripples are ascribed to the occurrence of local acidification at the tube bottom that increases the dissolution rate of the formed compact layer [4.4]. Besides the low aspect ratio of regime 2 nanotubes, a more interesting feature is observed in marked region of figure 4.1 (d) where nanotubes appear to have branched. The branching of TiO_2 nanotubes in glycerol based electrolytes have been reported by Anitha et. al. [4.5] where they employed a two-step potentiostatic anodisation of Ti foil at different ramp rates. They ascribed the occurrence of branching to the different ramping rates used. However, the occurrence of branching observed in figure 4.1 (d) is unclear and open new ideas for future investigations. One possible explanation for this phenomenon, however, may lie in the observed smaller nanotube pore diameter and wall thicknesses, shown in Table 1. The smaller pores are directly linked to the pit sizes, as described in Chapter 2, which in turn, are driven by the diffusion coefficient of the electrolyte system used. In this case, when using the glycerol system, a much higher aerial density of nanotubes is obtained, as shown by figure 4.1 (c), which subsequently yield the bunched ropes of nanotubes as can be observed. Because of this high density, and the continuous etching of the oxide layer, the available space for continuous oxide formation becomes limited and since saturation is not yet attained, alternative pathways of etching is found, subsequently leading to the branched nanotube structures.

4.2.2 Effect of Anodisation Potential and Fluoride Ion Concentration on the Morphology

It is well documented [4.3, 4.6] that no nanotubes are formed at anodisation potential of 5V and below in aqueous electrolyte, but only evidence of pore-formation or pits. This due to the dominance of the oxide formation (reaction 2.3) over the chemical dissolution rate. In this study, when a 60V anodisation potential was used to synthesise TiO_2 nanotubes in regime 1 electrolyte, similar results were observed as shown in figure 4.2. This result is ascribed to the enhanced field-aided chemical dissolution (reaction 2.5) rate of the compact layer by the fast-diffused fluorine species compared to the oxide forming rate. As for this result, the formed oxide film detached from the substrate and could be observed as white remnant on the electrolyte beaker.

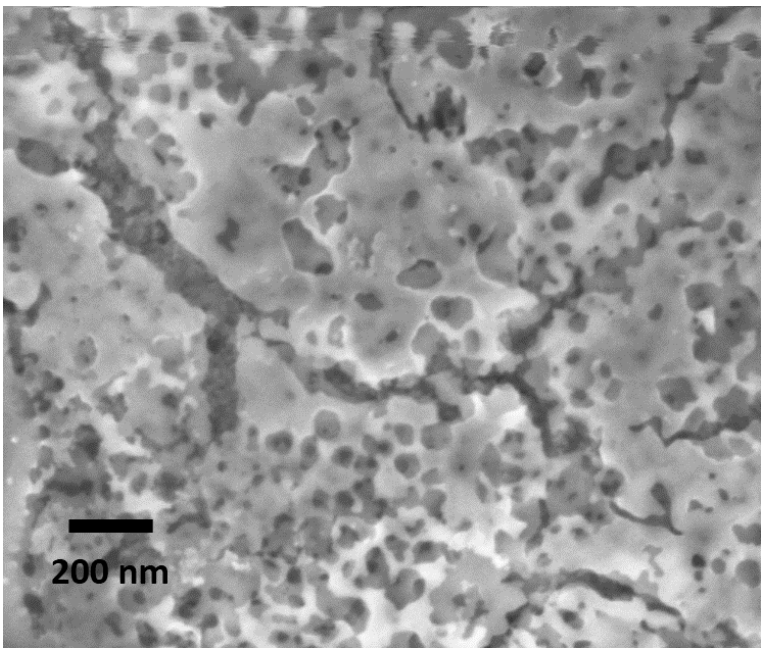

Figure 4.2: SEM micrograph of Ti surface after anodisation at 60V for 3 hours in regime 1 electrolyte

Figure 4.3 (a) illustrates the current-time transient curves recorded during the potentiostatic anodisation of Ti foil at anodic potential of 30 V in regime 1 electrolytes with varying fluorine ion (F^-) concentrations. Evident from the figure, during the initial phase of anodisation (stage i), the current density follows a steep drop as mentioned in chapter 2. This drop is ascribed to the formation of the resistive compact oxide layer. Following this region (stage ii), a current

recovery is observed in all three plots which is evidence of pore-formation. A striking feature in figure 4.3 is the shift in current-density peak position of (red-line) of the 1.2g NaF towards longer time duration. This shift is directly related to the enhanced dissolution rate of the oxide film as a result of the increased F^- species that interact with the oxide layer, thereby increasing the number of activation sites. Since there are so many activation sites, the resulting nanotubes are expected to have larger pore diameters at increasing F^- ion concentrations; this result is depicted in figure 4.4. Beyond stage ii, the current maintains as steady-state (stage iii) which is indicative of balance between the oxide formation etching rate, thus stage (iii) is regarded as the length determining stage as mentioned in chapter two.

Figure 4.3 (b) shows EDS spectra of the resulting TiO_2 nanotube revealing the presence of oxygen (O^- ion species) which suggest that resulting structure is in titanate form. Striking from the EDS spectra of TiO_2 nanotubes, is the presence of small phosphorous species. The intake of foreign species from the electrolyte have been also observed by [4.6- 4.8] and are believed to have influence on the formation of nanotube structures. Cummings et. al [4.8] reported that high concentrations of phosphor species (PO_4^{3-} ions) resulted in formation of rods with exterior walls containing large amounts of phosphor, which he later proposed that the presence of phosphor may have been an inhibiting factor in the formation of nanotubes. However, as shown in the EDS spectra, the phosphor concentration is so small, thus, it did not have impact as proposed.

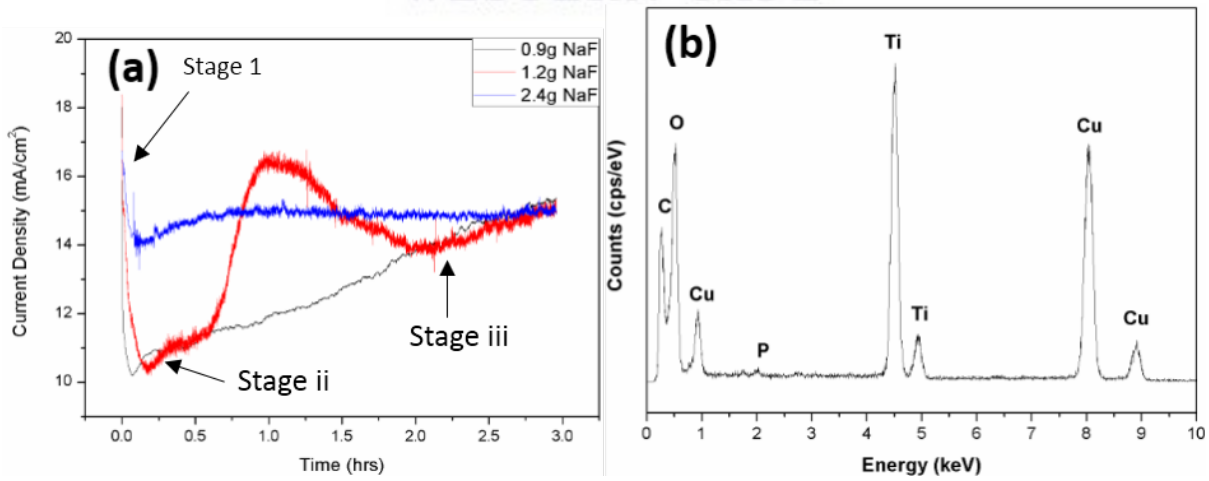

Figure 4.3: (a) Current-Time transient curves recorded during anodisation of Ti foil in at various F- ion concentrations, (b) the EDS spectra of the resulting nanotubes.

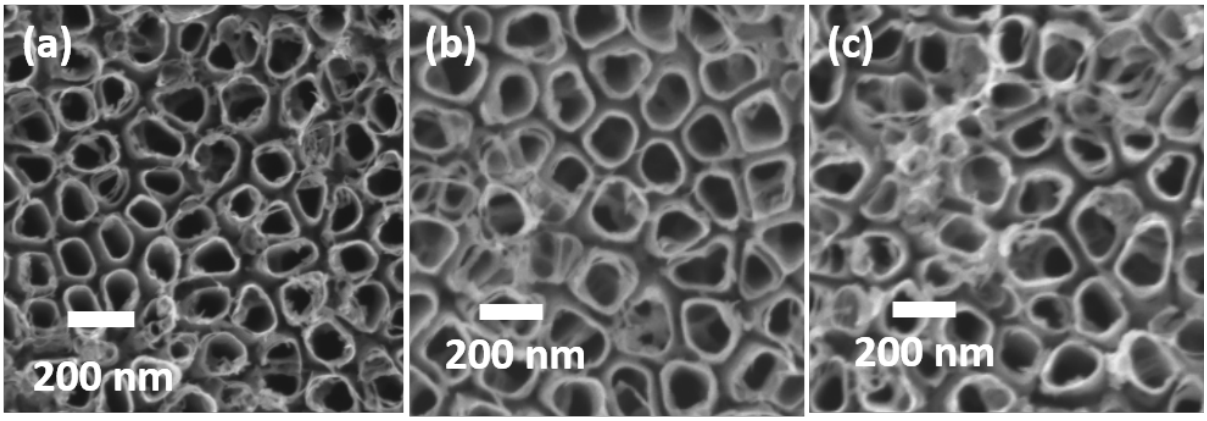

Figure 4.4: SEM micrographs of TiO2 nanotubes synthesised in different F- ion concentrations with their corresponding pore-diameters. (a) 0.9g NaF, 110 nm, (b) 1.2g NaF, 150 nm, and (c) 2.4g NaF, 180 nm

For conciseness, the results of the parametric studies performed on regime 2 and 3 are not shown, as the results obtained in regime 2 reveal similar trends with that observed in regime 1, i.e. an increase in anodisation potential and fluoride salt above (NaF > 8.4g) resulted in no nanotube formation. This is due to the rapid dissolution of the formed oxide layer compared to the rate at which it is formed. In regime 3, it was observed that anodisation at an anodic potential of 30 V for 3hours did not yield nanotube formation. However, through varying electrolyte composition and anodisation duration, nanotubes were obtained when the condition mentioned above was used. Thus, the condition was kept as the optimum condition for this study.

4.3 Crystallinity

As mentioned in chapter one, it is well documented that the as-synthesised TiO_2 nanotubes are amorphous and require thermal treatment at elevated temperatures above 250°C to induce crystallinity. Figure 4.5 shows a TEM bright-field image of the as-synthesised single TiO_2 nanotube synthesised in regime 1 electrolyte together with the corresponding SAED pattern. Evident from the SAED pattern, no distinct diffraction spots or rings are observed, only diffused broad low contrast scattering bands, confirming that the as-synthesised nanotube

structures are amorphous. Similar results are observed for nanotube arrays synthesised in other electrolyte regimes.

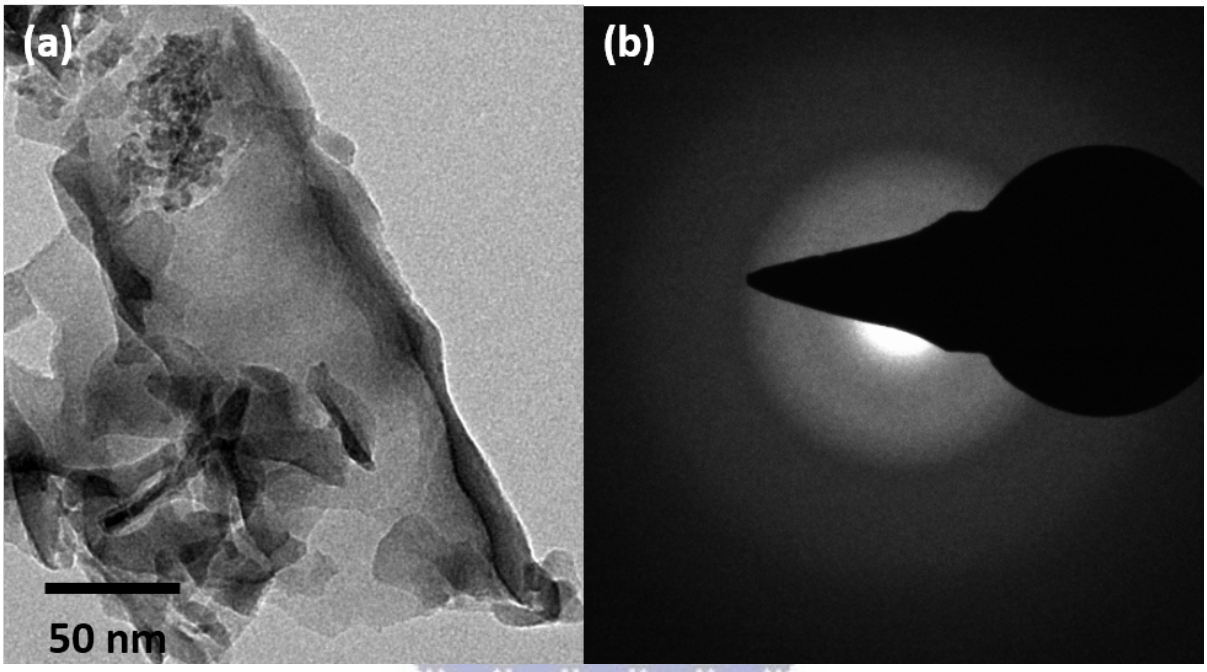

Figure 4.5: TEM bright-field image of (a) the as-synthesised single nanotube and the corresponding (b) selected-area electron diffraction pattern.

Upon annealing the TiO_2 nanotube samples at a temperature of 450°C in air for 3 hours, the samples show conversion of amorphous into predominantly anatase phase as depicted by the X-ray diffraction patterns in figure 4.6. The sample synthesised in the regime 2 electrolyte show no traces of rutile. However, the sample synthesised in regime 1 electrolyte have a low intensity peak (indicated by the arrow) at $\theta = 27.45°$ that corresponds to the (110) plane of rutile. The appearance of this low intensity rutile peak following annealing TiO_2 nanotubes at temperatures above 430°C has also been observed in publications by [4.9, 4.10] and it is indicative of crystallographic transformation of anatase crystallites into rutile. Moreover, it is evident from figure 4.6 that the major anatase orientation is the (101) plane with other planes such as (103), (200) and (105) present in minor amounts. The determined lattice parameters (a = b = 0.377 nm, c = 0.957 nm) of anatase phase following the indexing of the diffraction peaks are in agreement with those in the anatase JCPDS file (reference code: 00-001-0562). No

significant change in the average lattice constant obtained for the regimes presented in the figure.

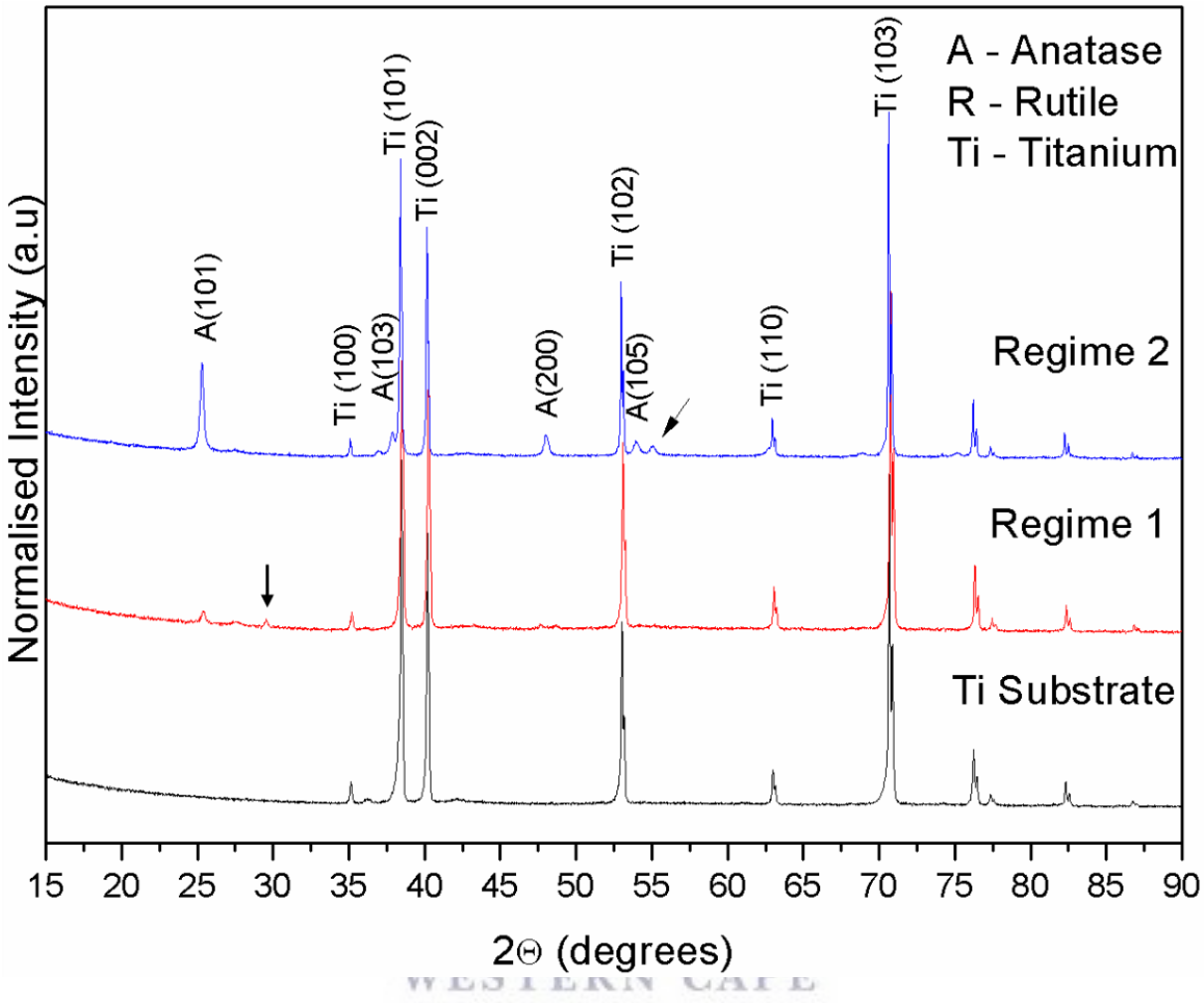

Figure 4.6: XRD patterns of TiO2 nanotubes that were annealed at a temperature of 450°C for 3 hours in air (atmospheric pressure). For comparison purpose, the XRD pattern of a commercially pure Titanium substrate was as also included

Shankar et al [4.11] observed a reduction of pore-diameter from 120 to 105 nm after annealing TiO_2 nanotubes at a temperature of 550°C in an oxygen environment. He ascribed the observed change to the occurrence of crystallisation. In this study, there are no discernable morphological changes in the TiO_2 nanotube architecture after thermal treatment. When the Scherrer formula (derived in chapter three, section 3.9.5) was employed to the XRD diffractograms of anatase phase, it was found that the TiO_2 nanotubes synthesised in regime 1 electrolyte has grain or crystal size of 32 nm with strain of ε_{str} = 0.000251, whereas those

synthesised in regime 2 showed a bigger crystal size of 45 nm with ε_{str} = 0.000176. Reports by [4.2, 4.13] suggest that the nanotube wall-thickness imposes geometrical constraint on the growth of bigger crystals at tube walls. Thus, the observed dominance of anatase phase in figure 4.6 with crystal size exceeding the dimensions of nanotube wall-thickness may be anatase crystals formed at the nanotube-Ti interface. In this region, there is a large available space for nucleation to occur. Hence, rutile crystals are formed as observed in figure 4.6. Furthermore, evident from table 4.1, the wall-thickness of nanotubes synthesised in regime 1 electrolyte have thinner walls than those synthesised in regime 2, thus, the obtained strain on the anatase crystal of regime 1 has slightly higher magnitude than that of regime 2 as a consequent result of the wall-thickness constraint.

Figure 4.7 shows TEM bright-field images of the annealed (at 450°C in air for 3 hours) single TiO_2 nanotubes synthesised in all three electrolyte regimes together with their corresponding SAED patterns. The occurrence of rings in the shown SAED patterns reveals the polycrystalline nature of TiO_2 nanotubes and indicate that the nanotubes crystallise predominantly in anatase with the most intense peak being that of (101) plane. The lattice parameters were found to be a = b = 0.379 nm, c = 0.942 nm, which are again in agreement with anatase JCPDS (reference code: 00-001-0562). No traces of rutile are observed in the SAED patterns of figure 4.7 as was the case in XRD pattern of regime 2 nanotubes. This difference is ascribed to the localised nature of the SAED pattern, compared to the bulk diffraction obtained during XRD. Macak et al [4.10] observed similar trends in glycerol based TiO_2 nanotubes that were annealed at 450°C. These results confirm that the nanotube wall thickness imposes a constraint on the growth of larger rutile crystals.

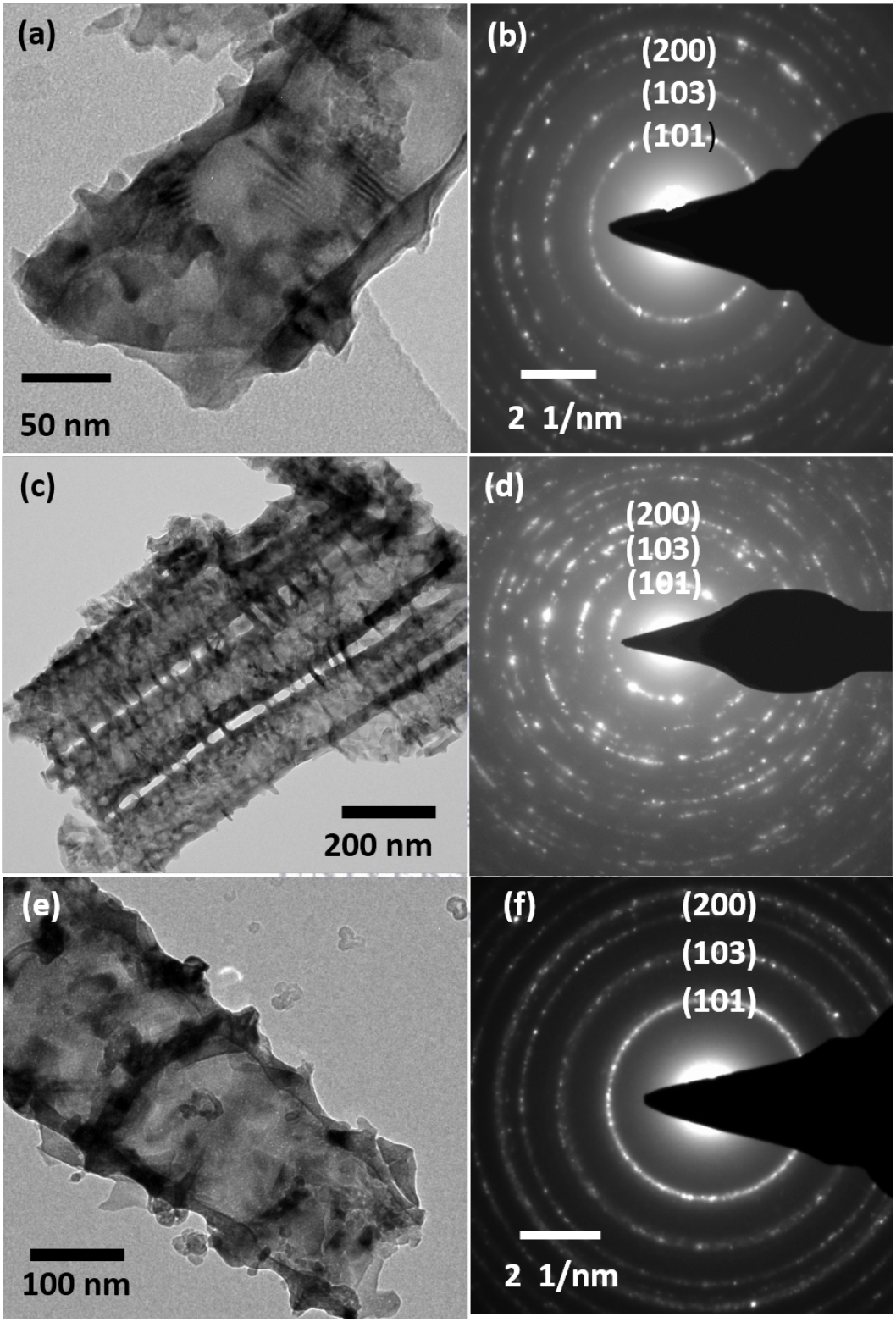

Figure 4.7: TEM bright-field images of the annealed (at 450°C in air for 3 hours) single TiO2 nanotubes synthesised in (a) regime 1, (c) regime 2, and (e) regime 3 electrolyte(s) with their corresponding SAED patterns (b), (d) and (f) respectively.

Figure 4.8 shows XRD patterns of TiO_2 nanotube after they were annealed at an elevated temperature of 600°C for 3 hours in air, at atmospheric pressure. Evident from the figure is the increase in the intensity of rutile peaks with the most intense peak arising from (110) plane of rutile that appears at angles ranging from θ = 27.47° to θ = 27.62°. This increase in intensity and the dominance of rutile peaks is indicative of the crystallographic transformation of anatase to rutile phase and the growth of rutile crystal.

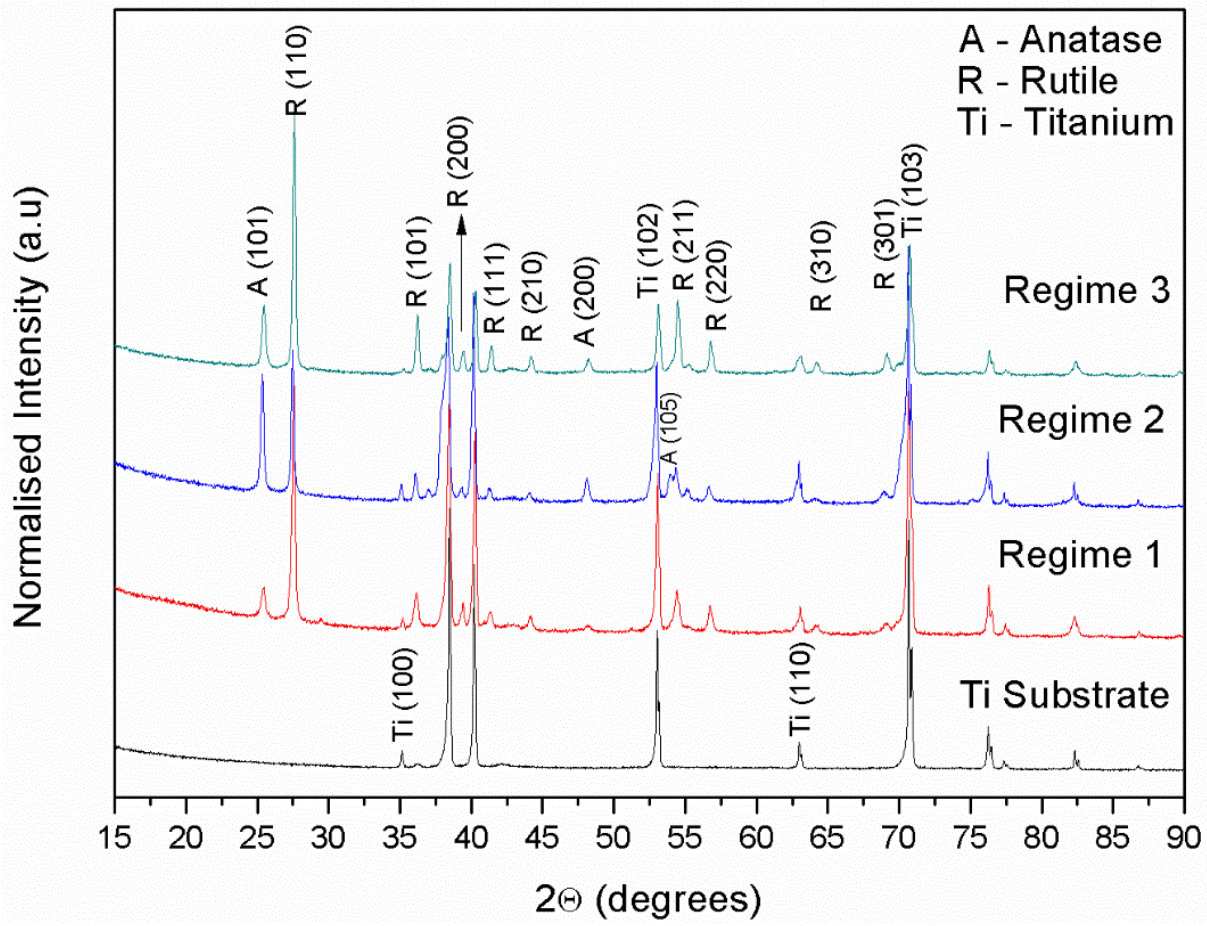

Figure 4.8: XRD patterns of TiO2 nanotube samples synthesised in all three electrolyte regimes and annealed at an elevated temperature of 600°C for 3 hours in air, at atmospheric pressure.

However, anatase peaks are still observed in the figure, suggesting a mixed phase TiO_2 nanotube structure. Similar results have been observed in literature [4.2-4.4, 4.8-4.14]. These mixed phase nanotubes are shown to have enhance photocatalytic properties when employed

in degradation of methylene-blue in aqueous solution under low power ultra-violet (UV)-light irradiation [4.15]. Moreover, Liao et. al. [4.16] also reported that the degradation of methyl-orange is enhanced when the mixed phase nanotubes are used.

Table 4.2 shows the anatase and rutile crystal sizes that were determined using Scherrer formula considering the full-width half maximum (FWHM) of the (101) and (110) planes of anatase and rutile respectively. The use of the Scherrer formula over the Williamson-Hall analysis is described by [4.20] who states that the use of Scherrer at crystal sizes below 100 nm is valid, especially when compared to the Williamson-Hall analysis that was employed. In this study the results obtained using Williamson-Hall analysis were inconsistent and didn't match the crystal sizes imaged during TEM, whereas those obtained from Scherrer were more consistent with TEM images. Furthermore, given that the sizes measured and calculated were well below 100 nm, the Scherrer formulation was preferred to report on the crystal sizes. The results show that when the annealing temperature is increased, both the anatase and rutile crystals obtained in for regime 1 nanotubes are increased. No comparison could be made for rutile crystal size of regime 2 nanotubes annealed at 450°C since its XRD patterns (figure 4.6) showed no traces of rutile phase. The observed results for regime 1 are in line with reports by [4.2] who reported that the anatase crystals initially increases with temperature, then start to decrease at annealing temperatures ranging from 480 to 580°, then again increases with temperature, whilst the rutile crystal continuously increases with temperature. However, a decrease in crystal size of rutile is observed for nanotubes synthesised in regime 2. The occurrence of this phenomena is unclear and forms part of future investigations.

Table 4.2: Comparison of anatase and rutile crystallite sizes of TiO_2 nanotubes annealed at 450°C and 600°C for 3 hours in air.

Electrolyte Regimes	Annealed at 450°C		Annealed at 600°C	
	Anatase Crystal Size (nm)	Rutile Crystal Size (nm)	Anatase Crystal Size (nm)	Rutile Crystal Size (nm)
1	32	17	34	54
2	45	-	39	45
3	-	-	31	35

Further investigations on the occurrence of rutile phase were performed by means of collecting high-resolution (HRTEM) images of nanotube walls together with the corresponding SAED pattern of a sample synthesised in regime 1(0.14 M (0.5 vol%) NaF + 0.5 M (2.5 vol%) H_3PO_4 + 97 vol% H_2O). The results of this investigation are shown in figure 4.9, and reveals that the nanotube walls are predominantly single crystalline, whereas the rest of the structure is poly-crystalline. From the SAED pattern, it was found that the first three rings that gave rise to the diffraction have interplanar d-spacing of (d_1 = 0.365 nm, d_2 = 0.236 nm, and d_3 = 0.183 nm). These d-spacing, corresponds to the d-spacings of (101), (103) and (200) planes of anatase phase when compared to those from the anatase JCPDS (reference code:00-001-0562). The diffuse in the SAED pattern may be ascribes to the amorphous region indicated by circle in the figure. When the interplanar spacing of lattice planes observed in figure 4.9 (a) were directly measured and it was found that they are spaced by d = 0.357 nm, which corresponds to the spacing of the (101) plane of anatase. In other words, the walls of the nanotubes grow along the [101] direction. It is well known in literature [4.6] that the nanotube walls crystallises only in the anatase phase due to the tube wall constraint. Thus, the results obtained suggest that the rutile phase that is observed in XRD patterns of figure 4.6 does not originate at the nanotubes surface, but from the seeded TiO_2 layer underneath the nanotube array.

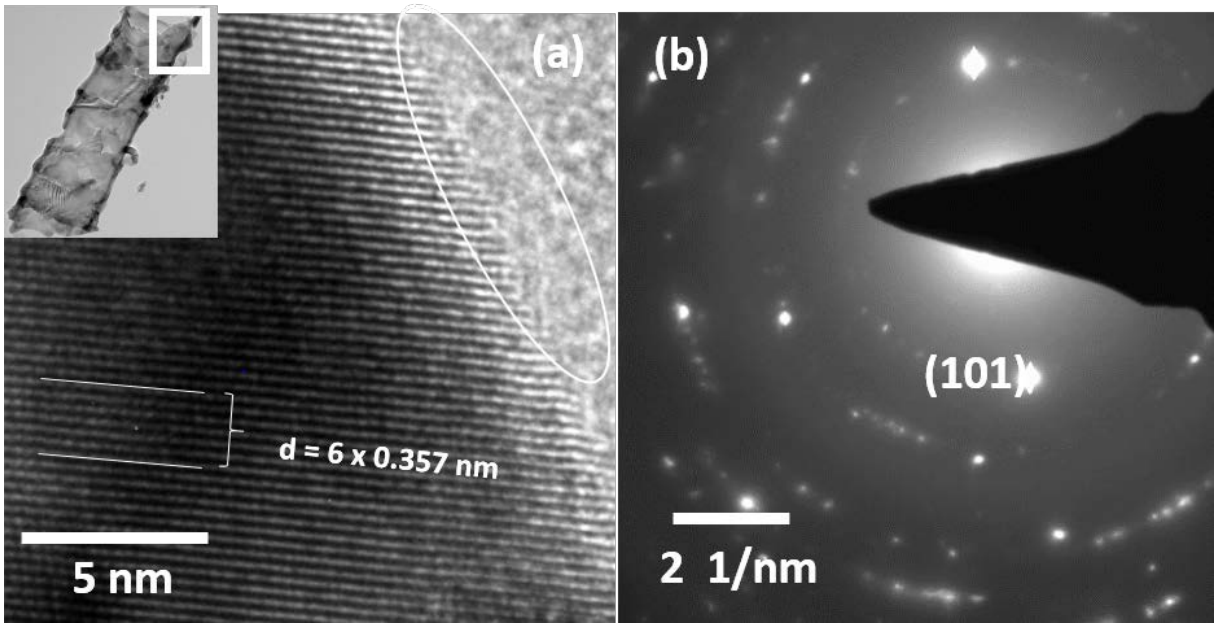

Figure 4.9: HRTEM image of (a) a single-crystalline bottom and wall of the nanotube, indicated by the inset and (b) the corresponding SAED pattern

4.4 Parallel Beam Electron Energy Loss Spectroscopy of TiO_2 Nanotubes

4.4.1 Energy Loss-Near Edge Fine Structure of Ti $L_{3,2}$ and O-K Line-shapes

Figure 4.10 shows EELS spectra of the annealed (at 450°C for 3 hours in air) TiO_2 nanotubes synthesised in regime 1 and 3 electrolytes. The EELS spectra were collected in normal bright-field TEM mode using a parallel beam (i.e. convergence angle = 0) during illumination. Each spectrum was background subtracted using the decay power law (as discussed in chapter 3) to remove the effect of plural scattering and other instrumental artifacts. Evident from figure 4.10 (a), the Ti L-edge character prevails at an energy loss of about 456 eV and exhibit a splitting into two main peaks namely L_3 and L_2 that are centered at 460 eV and 465 eV respectively. The measured separation of 5 eV between these two peaks is comparable to that of 5.4 eV that was observed by [3.17] and its occurrence is ascribed to the spin-orbit coupling of 2p states of Ti. It is noticeable that the spectrum of regime 1(black line) is shifted by 2 eV (indicated by dashed lines in the figure) to the higher energy loss.

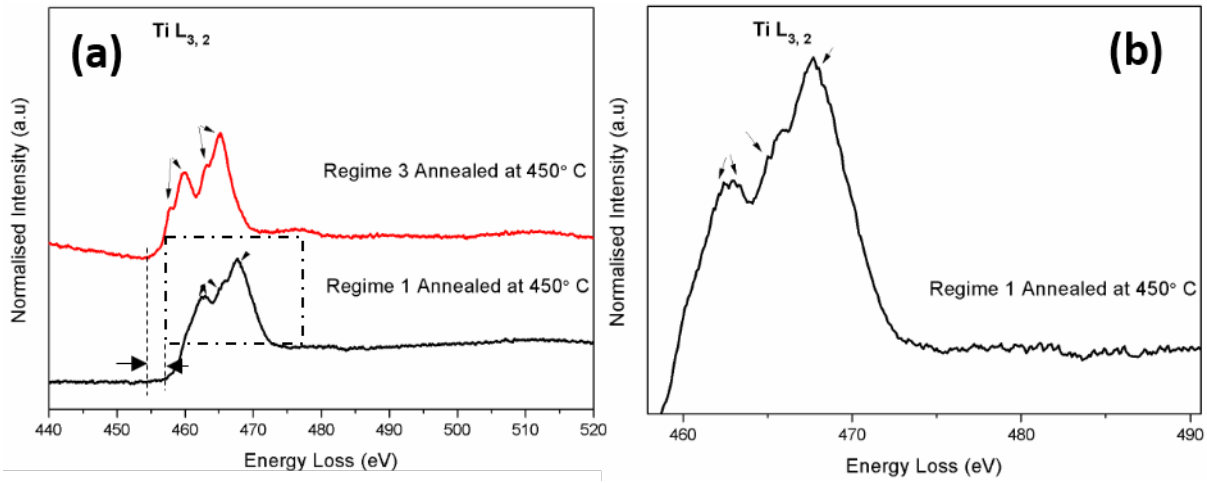

Figure 4.10: (a) Core-loss EELS spectra of the annealed TiO2 nanotube that were synthesised in regime 1 and 3 electrolyte bath, and the (b) zoomed area of interest that is indicated with the box with (a).

However, the observed shift is not structure related, but is suspected to be due to specimen drift, beam damage and/or long exposure times. At closer inspection of the figure, it is observed that the L_3 and L_2 edges exhibit a further splitting into two crystal-field peaks namely, three-fold t_{2g} and two-fold e_g bands (indicated by arrows). Considering the EELS spectrum of regime 3, the measured separation between the t_{2g} and e_g bands of the L_3-edge is 2.1 eV, whereas the measured separation for the L_2- edge is 2 eV.

Moreover, it is apparent from figure 4.10 (a) that the t_{2g} band of both the L_3 and L_2-edges occur as a shoulder at the lower energy loss of the e_g band, which is indicative of the point group symmetry of rutile [4.8, 4.17, 4.18]. This observation is supported by the measured separation of 2 eV between the t_{2g} and e_g bands of the L_3-edge, which Glote et al [4.19] reported as the recent theoretical crystal-field splitting for rutile. The two results mentioned above corroborate the results obtained from XRD studies which showed traces of crystallisation of TiO_2 nanotubes in rutile phase when annealed at 450°C. Zooming into the area indicated by the box (shown in figure 4.10 (b)), it is evident that the L_3-edge reveal a flat plateau which [4.18] reported to be indicative of the co-existence of both anatase and rutile crystals.

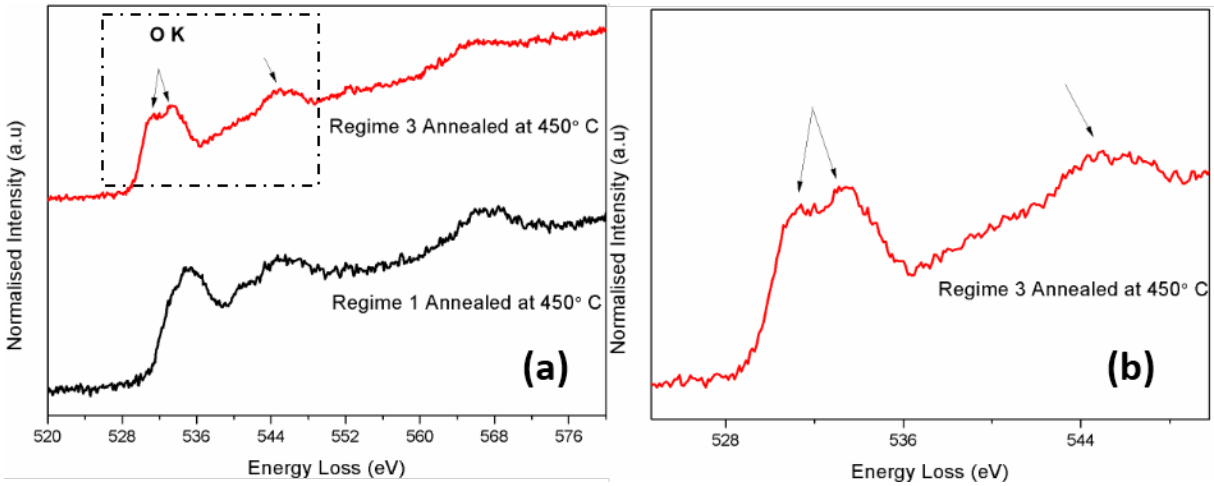

Figure 4.11: (a) Oxygen K-edge of the annealed TiO2 nanotubes that were synthesised in regime 1 and 3 electrolyte bath, (b) the selected area of interest (indicated by box) from (a).

The O K-edge EELS spectra of the annealed TiO_2 nanotubes depicted in figure 4.11 prevails at energy loss of 528 eV and exhibit two peaks (t_{2g} and e_g band) as a result of crystal-field splitting, with another ionisation edge (indicated by arrow in figure 4.11 (b)) occurring at higher energy loss. The two peaks (t_{2g} and e_g) of the O K-edge are centered at energy loss of 531.1 eV and 533.6 eV respectively, with energy separation of 2.5 eV. This separation corresponds to the 2.5 eV of anatase [4.19], thus the O K-edge also confirms the mixed phase structure of TiO_2 nanotubes.

4.4.2 Investigation of the Ti $L_{3,2}$ Energy Loss Near-Edge Fine Structure in Regime 1 Electrolytes

Figure 4.12 shows TEM micrographs of the anodised TiO_2 nanotubes (both top and side-views) synthesised at different fluoride concentrations in regime 1 electrolytes, at a fixed operating potential of 30V. Figure 4.12 (a) and (b) depict micrographs of the as-synthesised nanotubes, whereas the images shown in figures 4.12 (c) to (j) are that of the structures annealed at 450 °C at atmosphere for 3 hours. As can be observed in figures (h) to (j), no distinct nanotubes are formed at NaF concentrations exceeding 2.4g, whereas clearly defined nanotubular structures

with closed bottoms are observed in (a) to (h). This is again ascribed to the enhanced field-aided chemical dissolution (reaction 2.5) of the formed oxide layer as a result of the increase in fluorine species. Analyses of the corresponding SAED patterns shown in the insets in figure 4.12 show once more crystallisation in predominantly anatase.

Studies of ELNEFS features of the different structures shown above are depicted in figure 4.13 and show interesting Ti $L_{3,2}$ lineshapes. As observed, the as-synthesised 0.6 g and the annealed (at 450 °C in atmosphere for 3 hours) samples shows clear distinction of L_3 and L_2 edges, whereas the sample synthesised at NaF concentration above 1.2 g shows no discernible splitting of the L-edge. The latter makes sense since the corresponding TEM micrographs indicates no formation of nanotube structures, thus according to Stoyanov et al [4.21] its lineshape is characteristic of TiO oxides. It is worth knowing, as also mentioned in chapter 3, that the splitting of the L_3 and L_2 edges does not directly imply crystallisation in rutile or anatase phase, but it is indicative of unfilled 3d states in transitional metals/oxides. Hence, in figure 4.13 no information can be deduced from the crystallisation of the 0.9 g sample since there are no sub-band (shoulders) peaks observed. However, a more detailed analysis of the sample by means of STEM-EELS is presented in section 4.5 of this chapter. Regarding the 0.6 g sample, it has been confirmed from the corresponding SAED pattern that the as-synthesised nanotubes are amorphous.

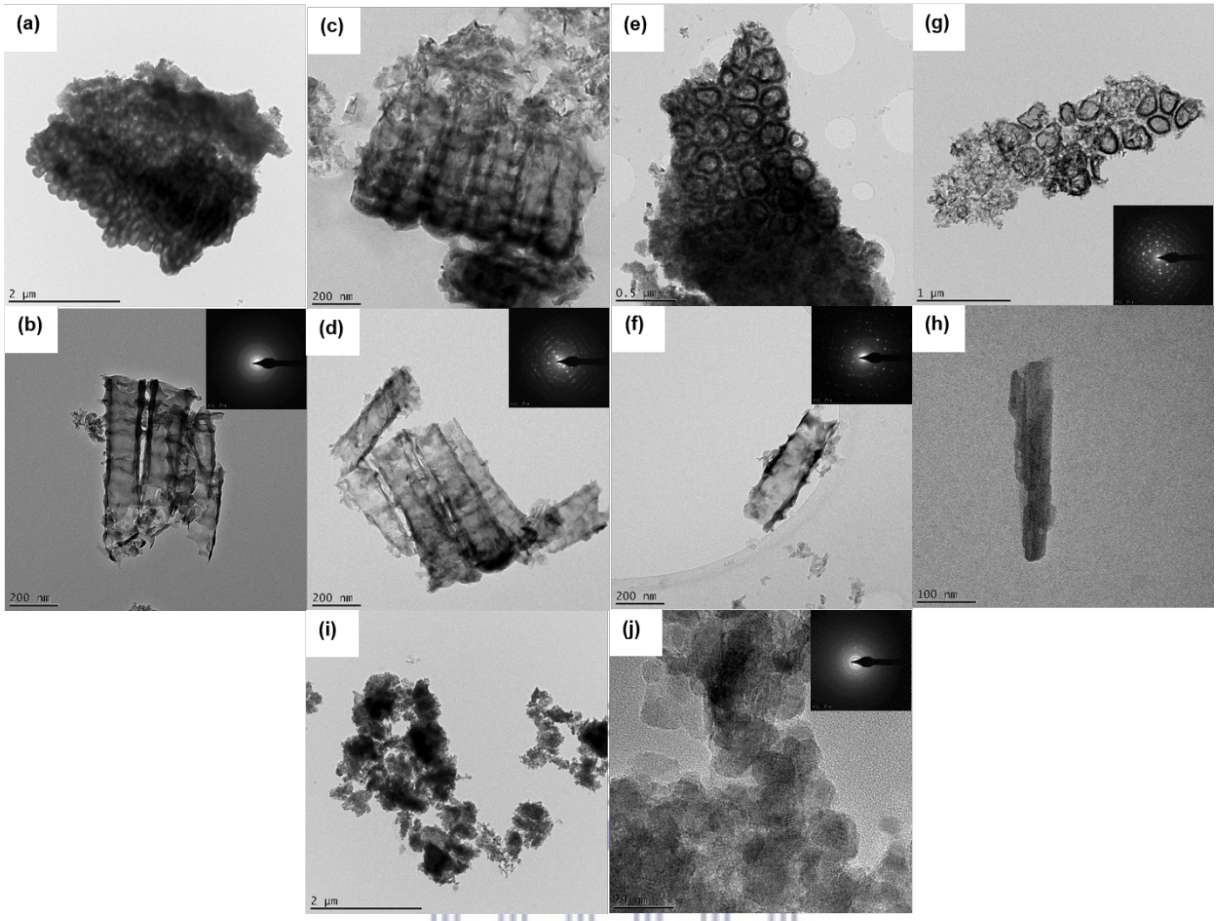

Figure 4.12: TEM micrographs of the as synthesised samples in regime 1 with (a)-(b) 0.6g NaF concentration, and the annealed samples with (c)-(d) and(e)-(g) 0.9g and 2.4g NaF concentration respectively. (i)-(j) are the samples synthesised at NaF concentrations exceeding 1.2g

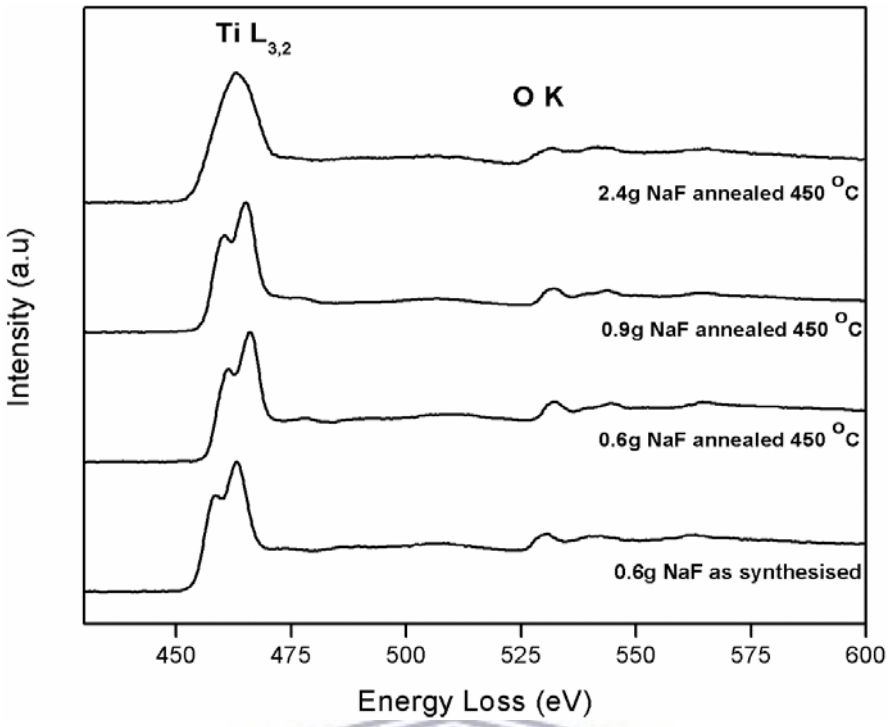

Figure 4.13: ELNEFS of the annealed (at 450°C for 3 hours in air) samples synthesised in regime 1 electrolyte at different NaF concentrations (as indicated) at fixed anodisation potential of 30 V

4.4.3 Investigation of the Ti $L_{3,2}$ Energy Loss Near-Edge Fine Structure in Regime 2 Electrolytes

Figure 4.14 shows TEM micrographs of samples synthesised in regime 2 electrolyte at different fluoride concentrations and fixed anodisation potential of 60 V. Evident from the figure, all three NaF concentrations used yielded successful synthesis of nanotubes with no distinct morphological changes observed. This is ascribed to the controlled diffusion coefficient of ionic species by the use highly viscous glycerol and reduction of water content. As mentioned in section 4.2.1, the anodisation duration of 4 hours used during the synthesis may have been another factor that resulted in achievement of similar structures. It is also observed (not shown but similar to figure 4.1 (c)) that nanotubes synthesised in this regime are bundled with their tube tops covered with debris. Report by [4.22] suggest that the bundling of nanotubes does not only destroy the tube tops but also affect performance of technological devices where they

are incorporated. For example, it lowers the efficiency of DSSCs due to the blocked/ destroyed tops which diminishes light permeation and block gas from interacting with nanotubes, thus badly affects the performance of sensors. Analyses of the SAED patterns (shown as insets) of figure 4.14 (a), (d) and (f) reveals crystallisation in predominantly anatase phase with rings that are suspected to be due to rutile crystals observed in the diffuse region of the SAED pattern.

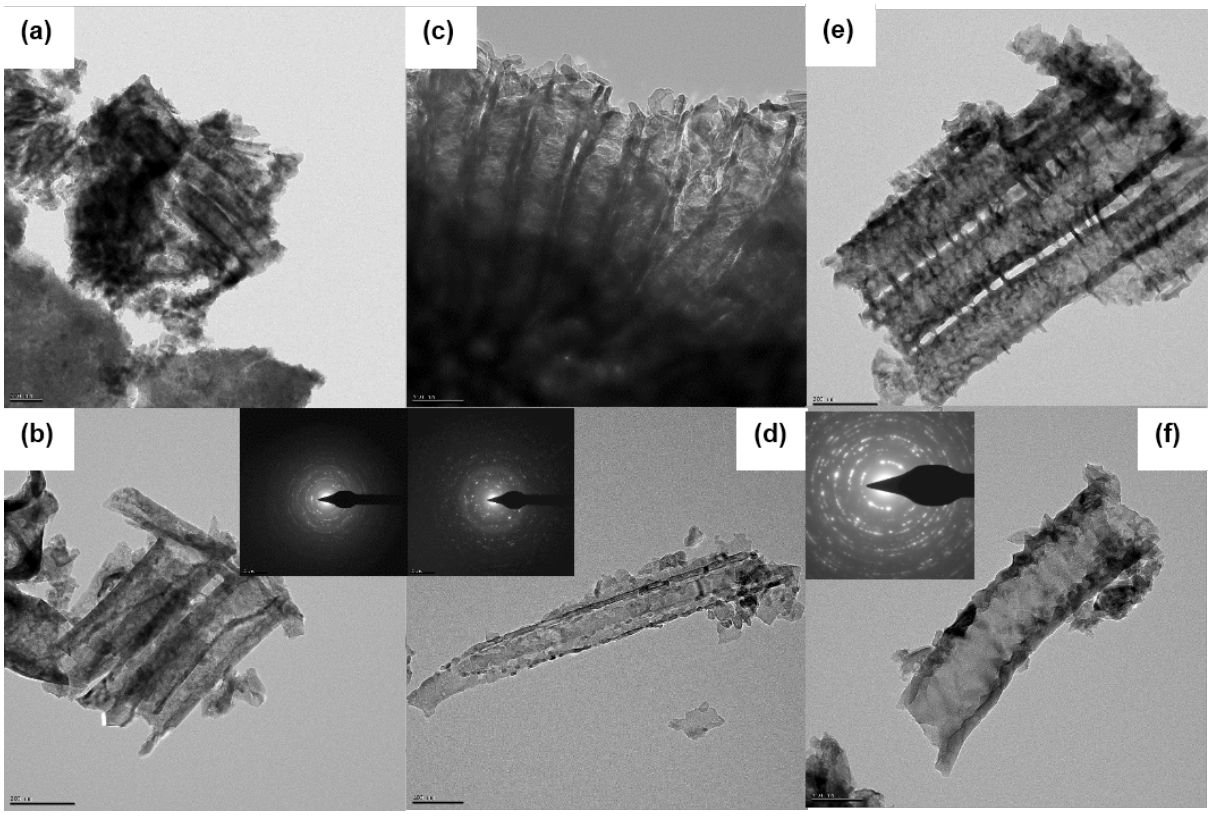

Figure 4.14: TEM micrographs and corresponding SAED patterns of the annealed samples synthesised in regime 2 electrolyte at different NaF concentrations.

The ELNEFS results of these samples are depicted in figure 4.15. It is observed from the figure that the Ti L-edge of samples synthesised with fluoride concentration of 4.2 g and 6.3 g exhibit a splitting into L_3 and L_2 edges, whereas no splitting is clearly observed for the sample synthesised in 8.4 g NaF concentration. However, it has been shown in figure 4.1 and 4.14 that TiO_2 nanotube structures are grown in this condition (8.4g NaF + 98 vol % Glycerol + 2 vol % H_20) and by means of SAED patterns, it has been deduced that the nanotubes crystallise in predominantly anatase phase. When considering the nature of the electron beam used (parallel illumination), the beam irradiates a large area on the specimen, thus, it is speculated that the

observed lineshape can be ascribed to a response from collective crystals in the specimen. It shall be observed in section 4.5 of this chapter that upon performing point by point analysis (STEM-EELS), the L-edge exhibit the characteristic splitting into L_3 and L_2 edges suggesting the presence of either or both anatase and/or rutile.

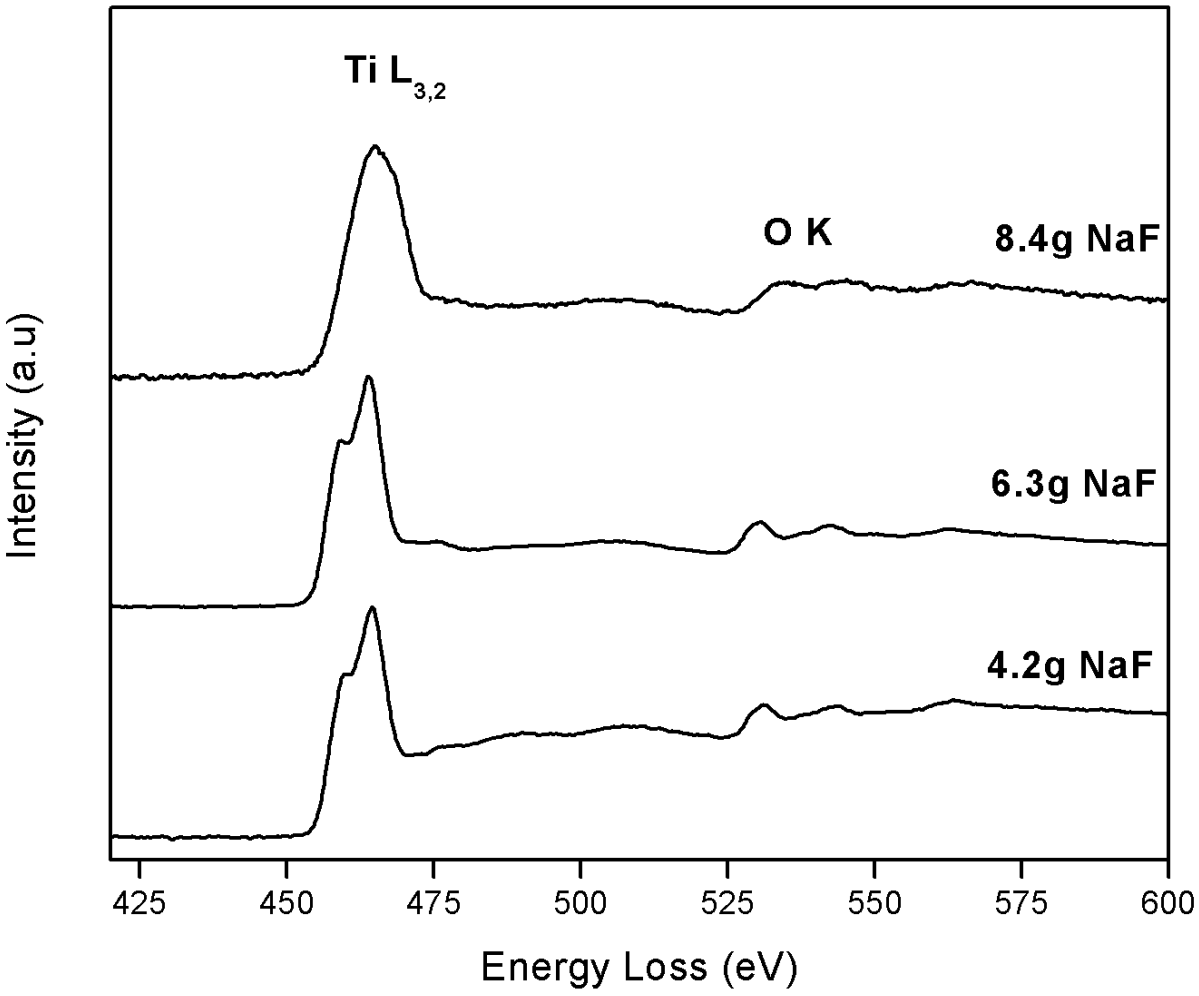

Figure 4.15: ELNEFS spectra of the annealed (at 450°C in atmosphere for 3 hours) samples synthesised in regime 2 electrolyte at different fluorine (as indicated) concentrations and fixed potential of 30 V

4.5 High Angular Annular Dark-Field STEM coupled with EELS

A more detailed investigation of the spatial distribution of the crystallographic (anatase and rutile) phases on the TiO_2 nanotube structure was performed by means of simultaneously collecting HAADF-STEM images together with the corresponding STEM-EELS spectra as shown in figures 4.16 to 4.19 below.

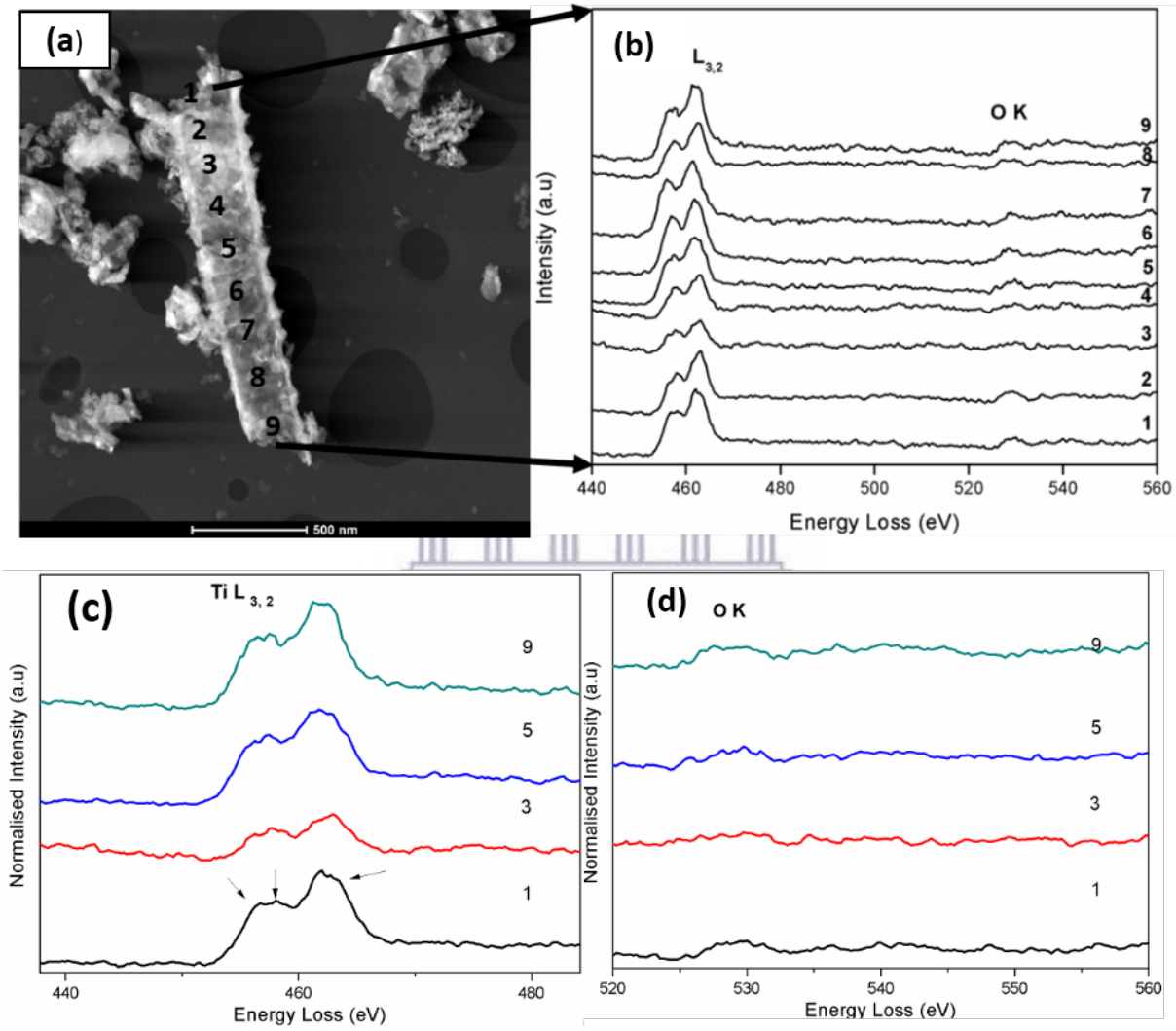

Figure 4.16: Shows a (a) HAADF-STEM micrograph of individual nanotube synthesised in (regime 1, 0.14 M (0.5 vol%) NaF + 0.5 M (2.5 vol%) H3PO4 + 97 vol% H2O) obtained with the line-scan along its length, (b) the corresponding STEM-EELS spectra at relative positions

Evident from figure 4.16 (b), the Ti $L_{3,2}$ line-shapes along the nanotube length (all positions) exhibit similar splitting as was observed in the case for parallel recording of EELS spectra with noticeable peak shift (with respect to position 1) of about 0.5 – 1 eV towards higher energy loss. Moreover, a very interesting feature observed in figure 4.16 (b), is the alteration in the occurrence of the t_{2g} and e_g bands for both the L_3 and L_2 edges as the beam-line scan approaches the bottom (position 9) of the tube. Figure 4.16 (c) shows magnified spectra of selected positions (1, 3, 5 and 9) from the tube top (1) to the tube bottom (9) illustrating the observed variations. At closer inspection of the line-shape originating from the nanotube top, it is evident that the t_{2g} band of the L_2-edge appears as the shoulder (indicated with arrow in EELS spectra of position 1) on the higher energy side of the e_g band with energy separation of 1.7 eV, which is indicative of anatase. However, the L_3-edge exhibit a dual shoulder effect (shown with arrows) which indicative of the coexistence of anatase/rutile phase. It is also discriminable from the EELS spectra of position 5, that t_{2g} of the L_2-edge appears as a shoulder on the low energy side of the e_g band which reveal the presence of rutile crystals, whereas the L_3 still possesses the dual shoulder effect. Towards the nanotube bottom (position 9), the dual shoulder effect is observed to have initiated also on the L_2 -edge resulting in a flat plateau shape, which is an indication of mixed-phase structure of TiO_2 nanotubes. It can be speculated that the occurrence of the t_{2g} band on the high energy side at the nanotube top (position 1) is indicative of the dominance of anatase phase, whereas towards the nanotube tube bottom it may be indicative of rutile dominance. No real information about the crystallographic structure could be obtained in the O K-edge shown in figure 4.16 (a), (d) due to poorly-resolves crystal-field splitting. However, it is observed that the O K-edge exhibit changes in line shapes towards the bottom of the nanotube, thus this could be indicative of variations in chemical bond lengths and distortion of the octahedra of the two crystal phases. Similar results for the annealed (at 450°C in atmosphere for 3 hours) TiO_2 nanotubes synthesised in regime 3 electrolyte were observed and are depicted in figure 4.17 below.

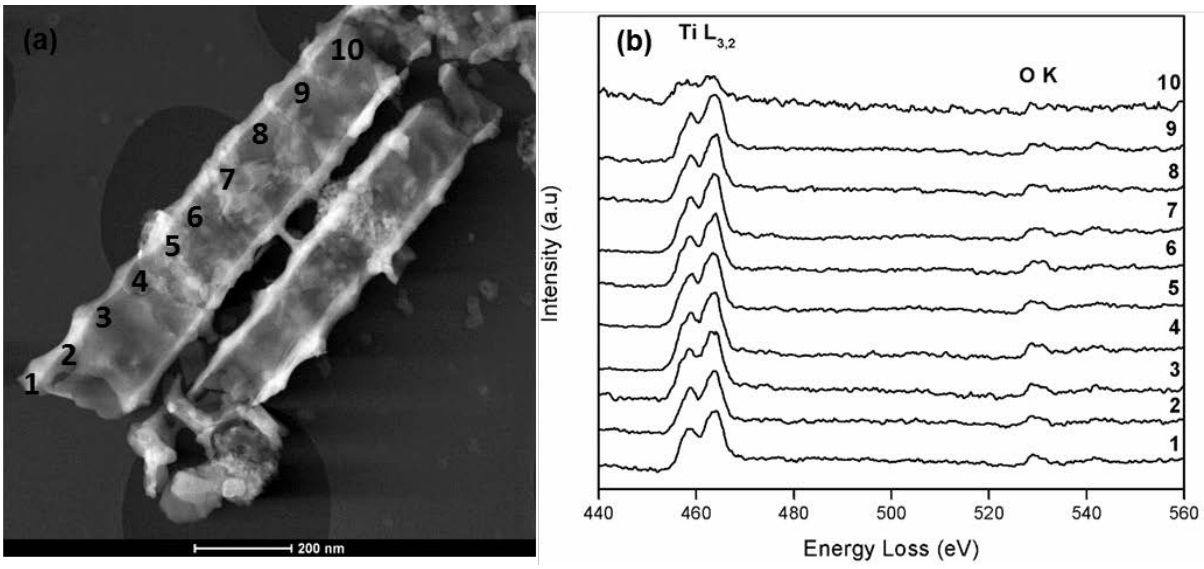

Figure 4.17: (a) HAADF-STEM micrograph of nanotubes synthesised in optimum condition of regime 3 and (b) the corresponding STEM-EELS

To elucidate the unclear crystallisation of the annealed TiO_2 nanotubes as per discussion in sections 4.4.2 and 4.4.3, figure 4.18 depicts the STEM-EELS spectra accompanied by the HAADF-STEM images of 0.6 g NaF sample synthesised in regime 1 and 8.4 g NaF sample synthesised in regime 2. A clear distinction of the L_3 and L_2 edge is observed for both samples synthesised in regimes 1 and 2 which is a feature that was not observed in figure 4.15. It is also observed that the L_3 edges for both samples appear to have broadened compared to those in figure 4.13 and it is indicative of a dual shoulder effect, whilst the L_2 edge (at position 3-bottom and 10-top) appears to have a low intensity shoulder on either low or high energy loss. The broadening of the L_3 edge (flat plateau) and the occurrence of a shoulder on the L_2 edge is indicative of the coexistence of both anatase and rutile phase with nanotube top (position 10, shown in inset of figure 4.18 (a)) revealing crystallisation in anatase phase, while the nanotube bottom is rutile rich. Similar features are observed for those samples shown in figures 4.13 and 4.15; not presented in figure 4.18 for conciseness.

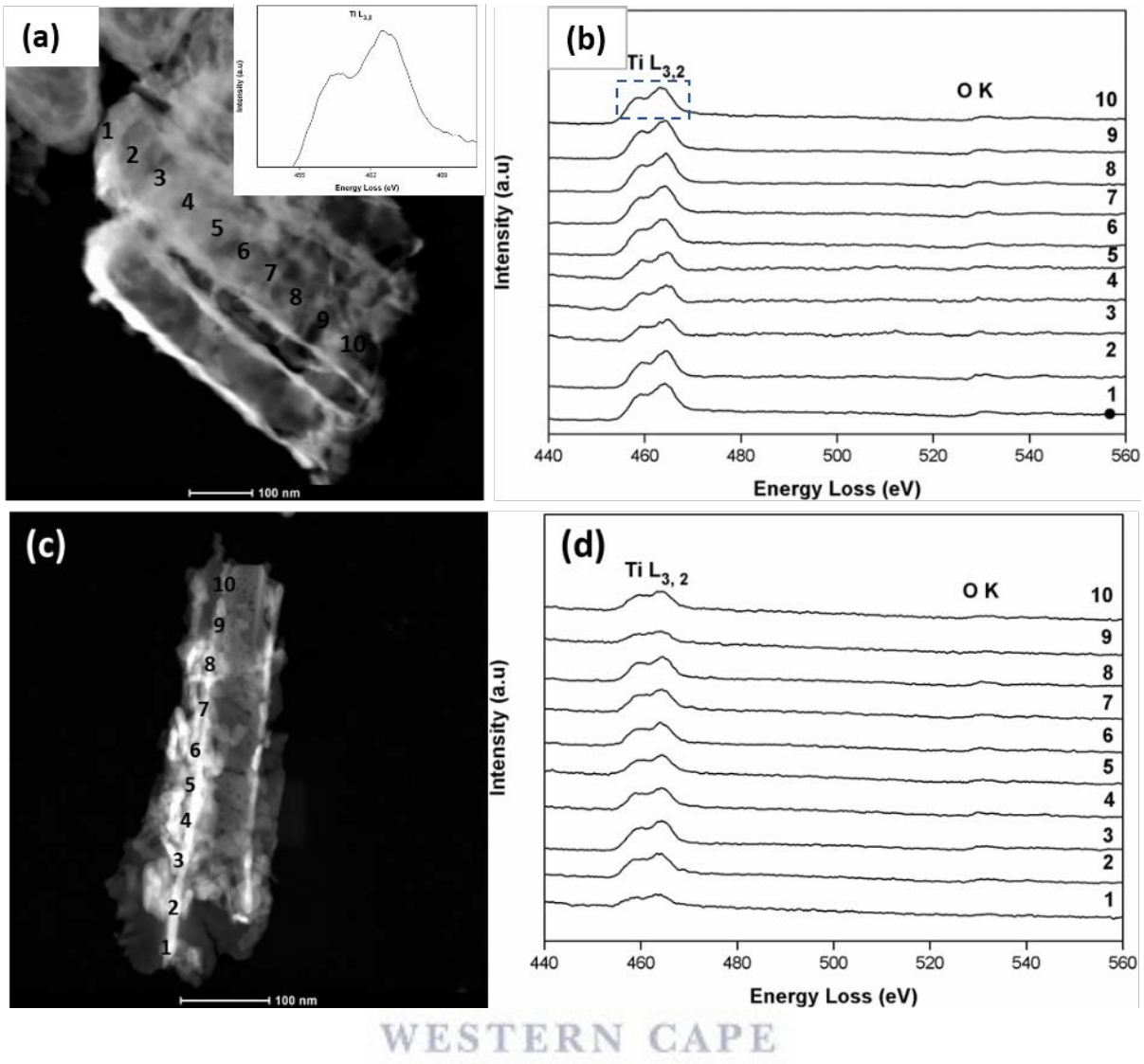

Figure 4.18: (a) and (c) HAADF-STEM micrograph of nanotubes synthesised regime 1 and 2, with their corresponding (b) and (d) STEM-EELS spectra

Figure 4.19 shows typical STEM-EELS spectra of a TiO_2 nanotube sample annealed at elevated temperature of 600°C for 3 hours in air. The spectra show no evidence of crystal-field splitting of the Ti $L_{3,2}$-edges, but only a broadening of the edges which may well be indicative of a flat plateau as consequence of the coexistence of both anatase and rutile phase. This to be true, since from the XRD results (shown in figure 4.8) it was observed that annealing the TiO_2 nanotube samples at elevated temperature of 600°C results in crystallisation of the samples in mixed-phase containing anatase and rutile crystals. The results depicted by figure 4.19 suggest a 50:50 presence of anatase and rutile crystals throughout the nanotube length.

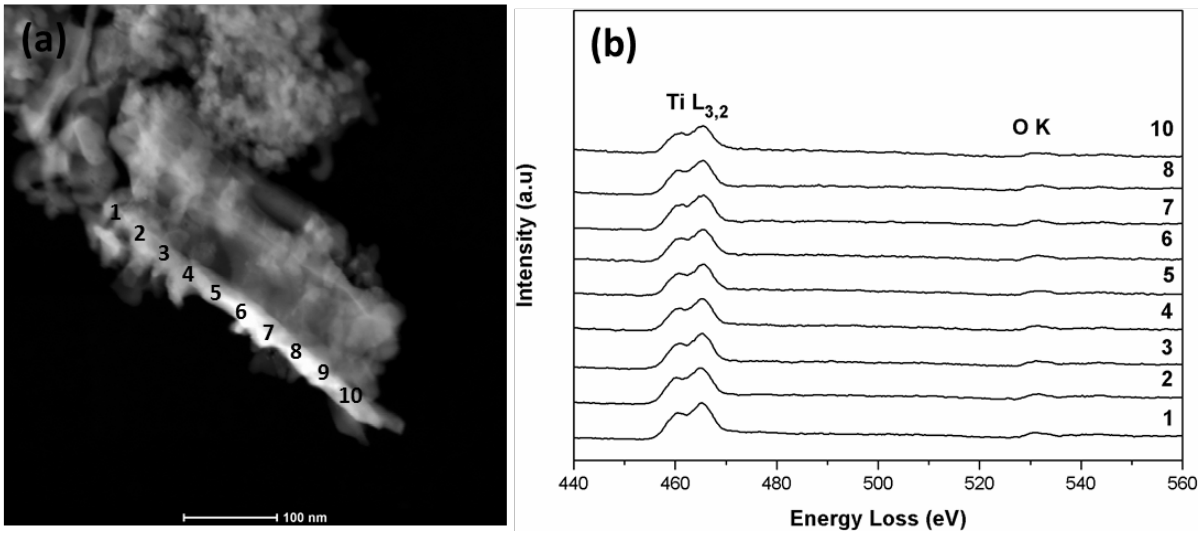

Figure 4.19: shows the (a) HAADF-STEM micrograph together with (b) STEM-EELS spectra scanned along the length of individual TiO2 nanotube sample annealed at elevated temperature of 600°C for 3hours in air.

4.6 Jump Ratio Imaging and Valence Electron Energy Loss Spectroscopy of Single Anodised TiO_2 Nanotube

Figure 4.20 shows a HAADF image of a single nanotube from the samples shown in figure 4.1 (e) and (f), i.e. in a regime 3 electrolyte at 60V for 77 hours and subsequently annealed at 450 °C in air for 3 hours. Also shown in figure 4.20 is the SAED patterns collected using a 200 nm selected area aperture from the circular areas indicated. An analyses of the SAED patterns once more show a rutile rich bottom, coupled by a mixed phase at the top regions of the structure, in accordance with the EELS results presented throughout sections 4.4 and 4.5 above. In this section, however, the study is aimed at coupling the diffraction data directly with imaging when taking a jump ratio (discussed in chapter 3), thereby providing a visual result.

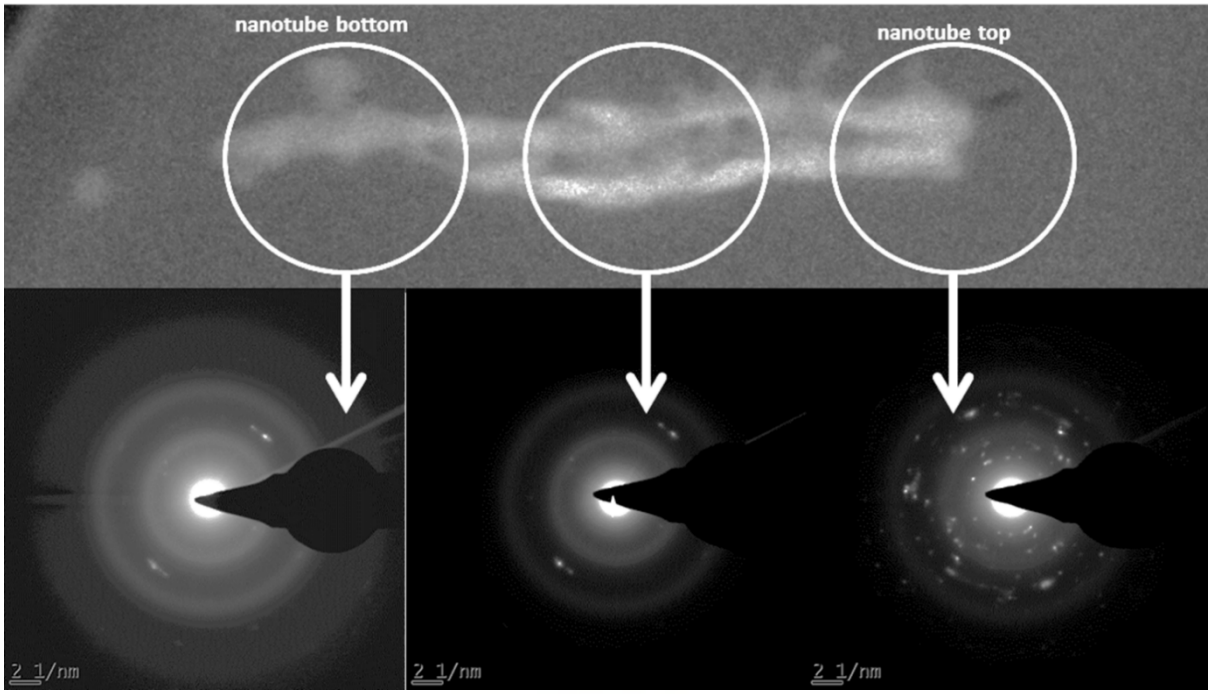

Figure 4.20: HAADF image coupled with SAED patterns of a single nanotube synthesised in regime 3 electrolyte. The SAED patterns were collected from the circular areas as indicated

The maps of the L_3 (labeled Ti pre-edge) and L_2 (Ti post-edge) bands of the Ti $L_{3,2}$ edge are shown in figure 4.21 below. The jump ratio maps were collected by centering a 2 eV energy slit at 460 (L_3) and 465 eV (L_2) and taking the ratio of firstly L_2/L_3 (shown as Ti L_2 jump ratio map) and then L_3/L_2 (Ti L_3 jump ratio map). The Ti L_3 jump ratio map shows the brighter contrast, with a jump ratio of 0.82 measured at the nanotube bottom. The theoretical value for L_3/L_2 for rutile is 0.91 but decreases due to instrumental effects, as well as the presence of different symmetries and Ti valence states [4.17]. In this case, based on the SAED results, this decrease in L_3/L_2 is attributed to the presence of anatase as well as rutile at the bottom and as such the Ti L_3 jump ratio map can be interpreted as a visual aid to demonstrate the rich rutile bottom of a single nanotube.

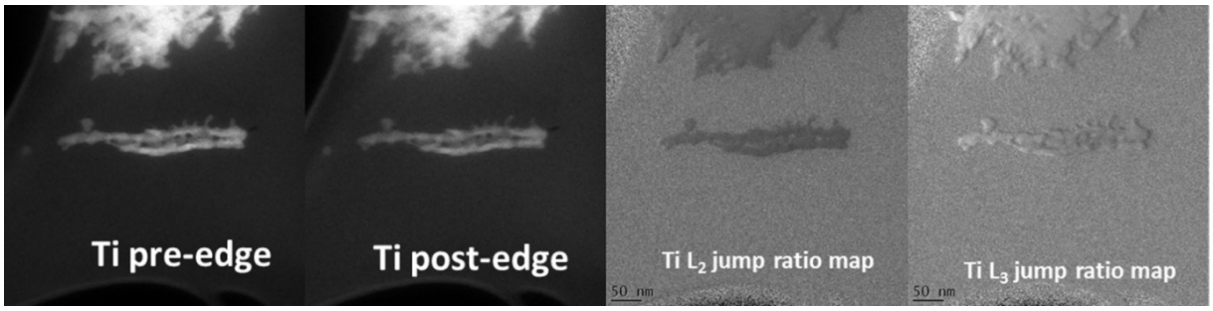

Figure 4.21: Energy filtered maps of the Ti pre- (L3) and post-edges (L2) collected with an energy slit of 2 eV, centered at 460 and 465 eV, respectively. The indicated Ti L2 and L3 jump ratio maps were collected by taking a ratio of the L3 and L2 filtered maps

Given this inhomogeneous crystalline nature of anodised TiO_2 nanotubes, it may be a worthwhile study to ascertain whether this influence the measured optical properties of the structure, in particular the bandgap. Using electron microscopy, this can be achieved by means of valence EELS, or so called VEELS. It must be noted, however, that the use of VEELS in elucidating the optical properties of nanostructures, in the absence of a monochromatic electron source, is very difficult due to the extended tail of the zero loss peak. Various methods, both mathematical and experimental, have been developed over the years to remove the tail of the ZLP from low loss EELS spectra, all with various success. In this study, the ZLP was removed by collecting a low loss EELS spectrum in vacuum (i.e. in the absence of a specimen) and then mathematically subtracting it from the eventual low loss spectrum, in accordance with Potapov et al [4.23]. Figure 4.22 shows the resultant VEELS data. As shown a single nanotube was imaged in STEM mode (figure 4.22 (a)), with a low loss EELS spectrum collected long the nanotube length at 8 strategic positions, depicted in figure 4.22 (b). The result of removing the ZLP and the determination of the bandgap is shown in figure 4.22 (c).

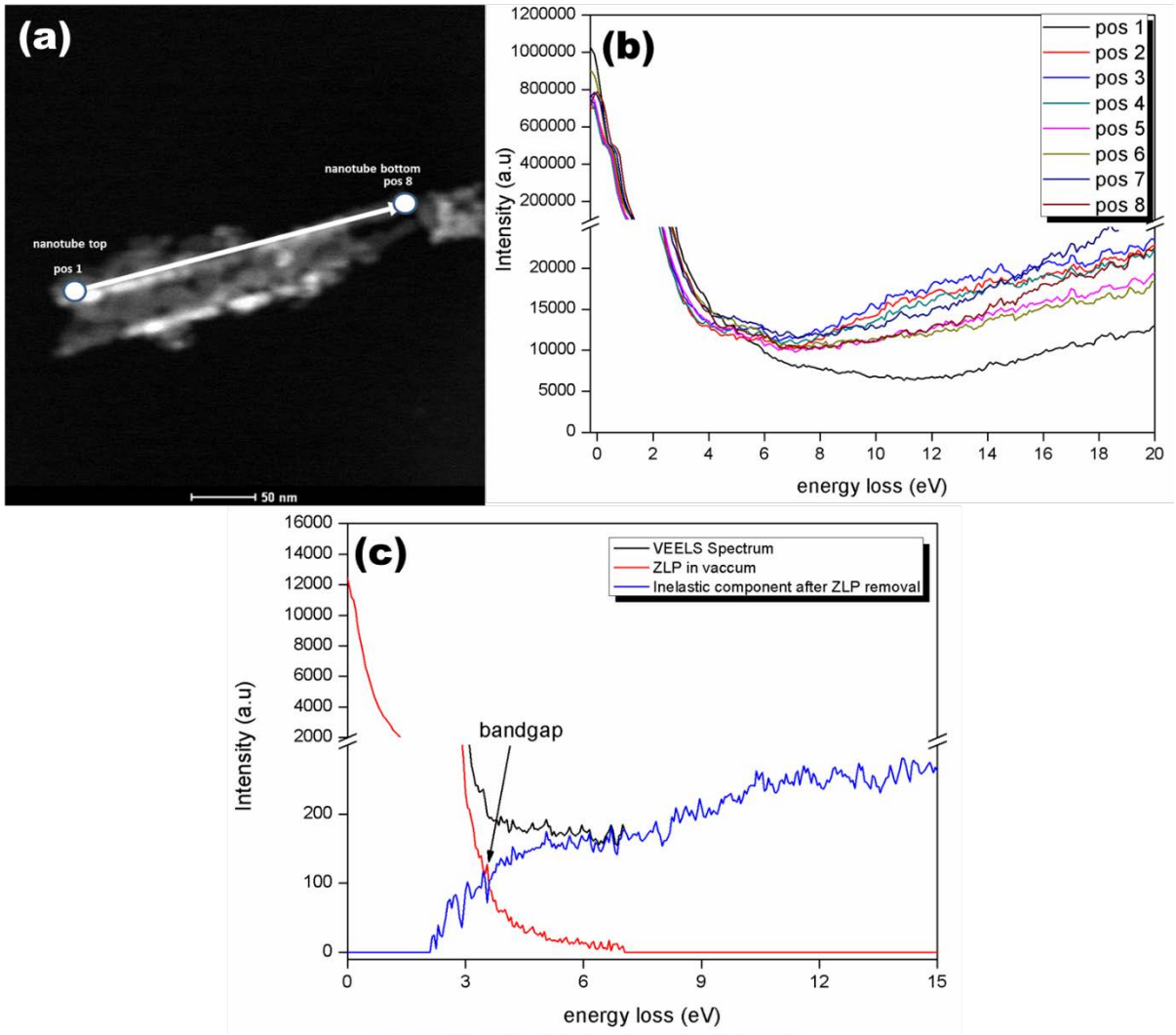

Figure 4.22: (a) HAADF micrograph of single nanotube with the positions at which low loss EELS spectra were collected indicated; (b) resultant low loss EELS spectra; (c) ZLP removal from low loss spectrum and determination of bandgap.

From figure 4.22, it is determined that the bandgap along the nanotube length is indeed not fixed, but varies with the distribution of the anatase and rutile crystals from bottom to top. From the spectra in figure 4.22 it is determined that the bandgap at the bottom of the nanotube averages around 3.12 eV, whereas at the top regions an average value of approximately 3.28 eV is determined. Anatase typically has an optical bandgap of 3.2 eV, whereas pure rutile has a gap of 3.0 eV [4.24] meaning the results from figure 4.22 correspond well with the STEM-EELS results reported in section 4.6 above.

4.7 Summary of Results

In this chapter, it has been deduced that the anodic synthesis of TiO_2 nanotubes in neutral, high-viscous electrolytes (regime 3) bath yields to nanotubes with high aspect ratio compared to the other two regime electrolytes. By means of SEM and TEM, it was observed that upon annealing the TiO_2 nanotubes at 450 °C for 3 hours in air, the morphology of the TiO_2 nanotubes was unchanged and crystallised in anatase, as shown by the SAED pattern of figure 4.7. However, the XRD results of figure 4.6 suggested that annealing the nanotube sample (regime 1) at 450 °C, induces some rutile crystallisation. The presence of rutile was believed not to be indicative of rutile crystallisation on the surface of the TiO_2 nanotubes, but rather from the seed layer underneath the nanotube [4.2, 4.13]. This conclusion was based on the geometrical constraint imposed by the nanotube walls. The microstructural investigations of individual TiO_2 nanotubes annealed at 450 °C and 600 °C reveal that the rutile crystals prevail half-way between the nanotube length and bottom for samples annealed at 450 °C, whereas for the 600 °C samples, the rutile crystals are evenly distributed throughout the nanotube length. These results may well be true when taking into consideration the reduction of the pore-diameter upon annealing the nanotubes at elevated temperatures, which consequently resulted in increased wall-thickness as was observed by [4.11]. Thus, from the microstructural investigations, it can be proposed that: the rutile crystals found in the nanotube side-walls may be small sized rutile crystallites, whereas larger size rutile crystals are found at nanotube bottom.

Further investigations by means of Jump-Ratio imaging and the corresponding SAED patterns reveal that upon annealing TiO_2 nanotubes at a temperature of 450 °C in air, the nanotube bottom crystallises in predominantly rutile, whilst the nanotube top consist of mixed phases (anatase and rutile). This conclusion is based on the experimentally observed deviation of the L_3/L_2 (L_3 jump ratio) from the theoretical value of 0.91 for pure rutile. Thus, this deviation can be directly related to the presence of anatase phase which, once again, confirms the coexistence of anatase and rutile in the TiO_2 nanotube structure. Furthermore, when the VEELS was used to probe for energy band-gap of the nanotubes following a tedious background subtraction to enable extraction of sensible information, it was found that the band-gap varies along the tube length with nanotube bottom having band-gap of 3.12 eV and of 3.28 eV at nanotube top. The obtained energy band-gap are neither of anatase (3.2 eV) or rutile (3.0 eV), but may well be true for a mixed phase of TiO_2 nanotubes structure as deduced in section 4.5 and 4.6.

References

[4.1] D. Gong, C. A. Grimes, O. K. Varghese, W. Hu, R. S. Singh, Z. Chen and E. C. Dickey, J Mater Res. 16 (2001) 3331

[4.2] Q. Cai, M. Paoulose, O.K. Varghese, C.A. Grimes, J Mater Res. 20 (2005) 230

[4.3] F. R. Cummings, 2012, "TiO_2 Nanotubes Based Dye-Sensitised Solar Cells", Unpublished PhD Thesis, University of the Western Cape, South Africa

[4.4] J.M Macak., 2008, "Growth of Anodic Self-Organized Titanium dioxide nanotube layers", Unpublished PhD Thesis, University of Erlangen, Germany

[4.5] V. C. Anitha, A. N Banerjee, S. W Joo and B. K Min, Material Science and Engineering B. 195 (2015) 1

[4.6] J.M. Macak, H. Tsuchiya, A. Ghicov, K. Yasuda, R. Hahn, S. Bauer and P. Schmuki, Curr. Opinion Solid State Mater. Science 11 (2007) 3

[4.7] S. Berger, S. P. Albu, F. Schmidt-Stein, H. Hildebrand, P. Schmuki, J.S. Hammond, D. F Paul and S. Reichlmaier, Surf. Sci. 605 (2011) L57

[4.8] F. R. Cummings, T. F. G. Muller, G. F. Malgas and C. J. Arendse, Journal of Physics and Chemistry of Solids 85 (2015) 278

[4.9] O. K. Varghese, D. Gong, M. Paulose, O. KG and C. A. Grimes, J Mater. Res. 18 (2003) 156

[4.10] J. M. Macak, H. Hildebrand, U. M. Jahn and P. Schmuki, Journal of Electrochemistry 01 (2008) 005

[4.11] K. Shankar, G. K. Mor, H. E. Prakasam, S. Yoriya, M. Paulose, O. K. Varghese and C. A. Grimes, Nanotechnology 18 (2007) 11

[4.12] O. K. Varghese, M. Paulose, K. Shankar and C. A. Grimes, J. Nanosci. Nanotechnol. 15 (2005) 109

[4.13] M. Paulose, G. K. Mor, O. K. Varghese, K. Shankar and C. A. Grimes, J. Nanosci. Nanotechnol. 178 (2006) 1158

[4.14] C. A. Grimes and G. K. Mor, (2009)," TiO_2 Nanotube Arrays- Synthesis, Properties and Applications", Springer Science + Business Media. New York

[4.15] M. Boehme and W. Ensinger, Nano-Mico Letters 3 (2011) 236

[4.16] Y. Liao and W. Que, J. Alloy. Compd. 1 (2010) 243

[4.17] R. Brydson. J. Phys.Condens. Matter 1 (1989) 797

[4.18] A. Tarasov, Z. Y. Hu, M. Maledina, G. Trusov, E. Goodilin, G. Van Tendeloo and Y. Drobovolsky, J. Phys. Chem. 121 (2017) 4443

[4.19] C. Gloter, C. P. Ewels, D. Arcon, P. Umek and C. Colliex, Physical Review B 80 (2009) 035413

[4.20] A. Weibel, R. Bouchet, F. Boulc and P. Knauth, Chem. Matter. 17 (2005) 2378

[4.21] E. Stoyanov, F. Langenhorst and G. Steinle-Neumann, American Mineralogist 92 (2007) 577

[4.22] D. Yu, Y. Song, X. Zhu, C. Yang, B. Yang and H. Xiao, J. Matlet. 109 (2003) 211

[4.23] P. L. Potapov, H. -J. Engelmann, E. Zschech and M. Stoger-Pollach, Micron 40 (2009) 262

[4.24] T. Luttrell, S. Halpegamage, J. Tao, A. Kramer, E. Sutter and M. Batzill, Scientific Reports 4 (2014) 4043

CHAPTER FIVE

Summary and Future Work

5.1. Summary

This study focused on investigating the effect of electrolyte regime on the resulting morphology of TiO_2 nanotubes, synthesised by potentiostatic anodisation. During the anodisation period, the growth of TiO_2 nanotubes is governed by three simultaneously occurring process; namely (i) field-aided oxidation of Ti at metal (Ti)-oxide interface forming Ti^{4+} ions which, through the presence of electric field, migrate outward the oxide and, (ii) react with the inward transported O^{2-} species to form/thicken a compact oxide layer, that is continuously(iii) etched due to the presence of the inward transported F^- ions species. The growth of TiO_2 nanotubes is largely influence by the environment through which the synthesis is performed and duration, thus the study investigated the resulting morphology by means of SEM and TEM following synthesis in three different electrolyte regimes. It is widely reported that upon annealing TiO_2 nanotubes at elevated temperatures, the crystallinity is induced in either rutile or anatase (and/or sometime as hybrid structure). However, very little is known about the crystal distribution along the nanotubes length. Hence, the emphasis of the study was on developing understanding about the crystallographic phase transformation of along the TiO_2 nanotube length after post-treatment at elevated temperatures. The investigations were conducted by means of XRD, TEM-SAED, HRTEM and HAADF imaging coupled with STEM-EELS which all probe various features of the resulting TiO_2 nanotube structure. The results outcomes of the study were reported and discussed in the previous chapter, thus in this chapter will conclude based on the discussed results.

TiO_2 nanotubes were successfully synthesised in all three electrolyte regimes with aqueous acidic regime 1 (0.14 M (0.5 vol%) NaF + 0.5 M (2.5 vol%) H_3PO_4 + 97 vol% H_2O) yielding to rippled side-walled nanotubes with average pore-diameter of 150 nm, length and wall-thickness of 26 μm and 23 nm respectively. Organic neutral Regime 2 (1 M (3 vol% NaF + 2 vol% H_2O + 95 vol% glycerol) and 3 (0.14 M (1 vol%) NH_4F + 97 vol% PEG + 2 vol% H_2O) yielded to generally smooth side walls with regime 3 having high aspect ratio (pore-diameter

of 200 nm, length of 39 μm and wall-thickness of 29 nm) due to the well-controlled diffusion rate of ionic species by using highly viscous PEG-400. Regime 2 electrolyte yielded to nanotubes with average pore-diameter of 58 nm, wall-thickness and length of 1.9 μm. Compared to the other two electrolyte regimes, regime 2 electrolyte had the least aspect ratio due to the reduced anodisation duration and low-diffusion rate of ionic species. Moreover, SEM micrographs of nanotubes synthesised in this electrolyte regime revealed that the nanotubes are bunched, branched and with almost the entire nanotube tops covered with debris. It is proposed that the resulting morphology of regime 2 is due to the use of high fluorine concentration which result in high areal density of nanotubes. Because of the high areal density, the bunching of nanotubes occurred and because of the continuous etching of the oxide layer, the available space for continuous oxide formation became limited and since saturation was not yet attained, alternative pathways of etching were found, subsequently leading to the branched nanotube structures.

The as-synthesised nanotubes were shown, by means of SAED patterns, to be amorphous and upon annealing at a temperature of 450°C and 600°C in air the crystallinity was induced. XRD studied revealed that nanotubes synthesised in regime 2 were crystallised in anatase phase with no trace of rutile, whilst regime 1 electrolyte contained a low intensity peak (110) of rutile. When Scherrer formula was used to determine the crystallite size, it was found that the anatase crystals in regime 1 were 32 nm big with those in regime 2 having a crystallite size of 45 nm. Results obtained in XRD patterns revealed that when the annealing temperature is increased to 600°C, a mixed phase TiO_2 nanotube structure is attained for all three electrolyte regimes. However, at 450°C and 600°C the SAED patterns revealed presence of anatase crystals with no traces of rutile crystals even though they were observed in XRD patterns. As such, the STEM-EELS technique was used to probe the crystallographic transformation along nanotube length.

Parallel EELS results revealed the presence of rutile crystals at the seeded area underneath the nanotubes, which is a feature that was not observed in the SAED patterns of the nanotubes synthesised in all three-electrolyte regime. Further investigations of the TiO_2 nanotube microstructure by means of STEM-EELS and Jump-ratio, revealed that the rutile and anatase crystals are randomly distributed along the nanotube length with anatase crystals dominant from nanotube top to mid-way, whilst the rutile phase dominate half-way to the bottom of the

nanotubes. Valence EELS results show that the mixed phase structure of TiO_2 nanotubes have inconsistent band-gap along the nanotube with nanotube bottom having energy band-gap of 3.12 eV, while the top have band-gap of 3.28 eV. It is observed that the band-gap at nanotube top is closer to the band-gap of anatase (3.2 eV), whereas that of nanotubes bottom is close to that of rutile (3.0 eV). It is proposed that the obtained band-gap results are due to the dominance of these crystallite phases at certain positions along the nanotube length. Thus, it can be concluded that upon annealing nanotubes at 450°C the nanotube bottom and top crystallises in predominantly rutile and anatase phase respectively, whereas along the nanotube length, there exist a mixture of the two crystallite phases.

5.2. Future Work

This study, for the first time, probed the evolution of the crystallinity using predominantly advanced TEM techniques, as discussed. As part of the future work, our group aims to investigate whether we can apply the knowledge generated in this study to advanced SEM characterisation techniques, one of which being electron backscatter diffraction (EBSD) and transmission Kikuchi diffraction (TKD).

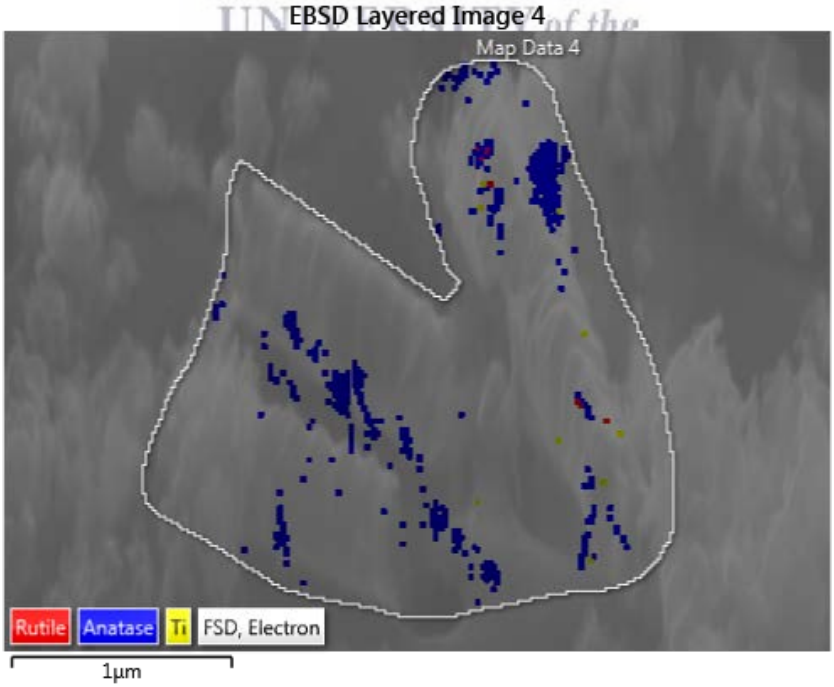

Figure S1: Example of a TKD map showing regions containing anatase, rutile and Ti phases

Figure S1 shows an example of the first results obtained by TKD where three anodised TiO_2 nanotubes are imaged and indexed. Although the indexing of the TKD patterns are low, it can be seen that traces of both anatase and a very small volume of rutile can be indexed along the nanotube length. These preliminary studies are well supportive of the major findings of this thesis, and once more proves that the work presented in this study is accurate and meaningful to the research community. As such, a draft manuscript, for publication in an international, peer-reviewed journal is currently in progress and will be submitted for review as soon as the TKD studies are complete.